

Unravelling the  
snowmelt–albedo feedback in  
Antarctica

**Stan Jakobs**

Author: Stan Jakobs  
Cover design: Melissa van Beekveld  
DOI: 10.33540/481  
ISBN: 9789464191332  
Printing: Gildeprint, Enschede

Institute for Marine and Atmospheric research Utrecht (IMAU)  
Department of Physics  
Faculty of Science  
Utrecht University

# **Unravelling the snowmelt–albedo feedback in Antarctica**

Het ontrafelen van de smelt–albedo terugkoppeling in Antarctica  
(met een samenvatting in het Nederlands)

't Ontrafele van de smeltj–albedo truukkoppeling in Antarctica  
(mèt 'n samevatting in 't Limburgs)

PROEFSCHRIFT

ter verkrijging van de graad van doctor aan de Universiteit Utrecht  
op gezag van de rector magnificus, prof. dr. H.R.B.M. Kummeling,  
ingevolge het besluit van het college voor promoties  
in het openbaar te verdedigen op

maandag 8 maart 2021 des middags te 12.45 uur

door

**Constantijn Lambertus Jakobs**

geboren op 7 september 1991  
te Heythuysen

**Promotor:**

Prof. dr. M.R. van den Broeke

**Copromotor:**

Dr. C.H. Tijm-Reijmer

Dit proefschrift werd mede mogelijk gemaakt met financiële steun van de Nederlandse Organisatie voor Wetenschappelijk Onderzoek (NWO).

# Contents

<b>Summary</b> .....	<b>ix</b>
<b>Samenvatting in het Nederlands</b> .....	<b>xii</b>
<b>Samevatting in 't Limburgs</b> .....	<b>xvi</b>
<b>1 Introduction</b> .....	<b>1</b>
<b>1.1 Sea level rise</b> .....	<b>1</b>
<b>1.2 Surface Mass Balance</b> .....	<b>2</b>
<b>1.3 The Antarctic ice sheet</b> .....	<b>5</b>
1.3.1 Geographical description .....	5
1.3.2 Climatology .....	7
1.3.3 Ice shelves .....	10
<b>1.4 Surface melt</b> .....	<b>11</b>
1.4.1 Snowmelt–albedo feedback .....	13
<b>1.5 Thesis outline</b> .....	<b>15</b>

---

<b>2</b>	<b>Methods</b> .....	<b>19</b>
<b>2.1</b>	<b>Surface Energy Balance</b>	<b>19</b>
<b>2.2</b>	<b>Modelling the SEB</b>	<b>22</b>
2.2.1	Radiation fluxes .....	22
2.2.2	Turbulent fluxes .....	24
2.2.3	Ground-heat flux .....	26
2.2.4	Albedo parameterisation .....	28
<b>2.3</b>	<b>Automatic weather stations</b>	<b>30</b>
2.3.1	Neumayer Station and the Baseline Surface Radiation Network . . .	33
<b>2.4</b>	<b>Regional climate models</b>	<b>35</b>
2.4.1	RACMO2 .....	36
<b>3</b>	<b>SMAF at Neumayer</b> .....	<b>39</b>
<b>3.1</b>	<b>Introduction</b>	<b>39</b>
<b>3.2</b>	<b>Methods</b>	<b>42</b>
3.2.1	Surface energy balance model .....	42
3.2.2	Albedo parameterisation .....	44
3.2.3	Observational data .....	47
<b>3.3</b>	<b>Results: surface energy balance and melt</b>	<b>49</b>
3.3.1	SEB model performance and uncertainties .....	49
3.3.2	Surface energy balance .....	52
3.3.3	Melt season .....	54

---

<b>3.4</b>	<b>Results: the snowmelt-albedo feedback</b>	<b>56</b>
3.4.1	Optimising the albedo parameterisation . . . . .	58
3.4.2	Magnitude of the snowmelt-albedo feedback . . . . .	61
<b>3.5</b>	<b>Conclusions</b>	<b>63</b>
<b>4</b>	<b>Evaluation of RACMO2 . . . . .</b>	<b>65</b>
<b>4.1</b>	<b>Introduction</b>	<b>65</b>
<b>4.2</b>	<b>Methods</b>	<b>69</b>
4.2.1	Automatic weather stations . . . . .	69
4.2.2	Surface Energy Balance model . . . . .	73
<b>4.3</b>	<b>Results</b>	<b>74</b>
4.3.1	Annual means and seasonal cycles . . . . .	74
4.3.2	Two case studies: meteorological drivers of surface melt . . . . .	79
<b>4.4</b>	<b>Evaluation of other surface melt products</b>	<b>82</b>
4.4.1	Temperature–index models . . . . .	82
4.4.2	RACMO2 . . . . .	83
4.4.3	QuikSCAT . . . . .	87
<b>4.5</b>	<b>Summary and conclusions</b>	<b>88</b>

---

<b>5</b>	<b>SMAF in Antarctica</b> .....	<b>91</b>
<b>5.1</b>	<b>Introduction</b>	<b>91</b>
<b>5.2</b>	<b>Methods</b>	<b>93</b>
5.2.1	Model descriptions .....	93
5.2.2	Quantifying SMAF .....	96
<b>5.3</b>	<b>Results</b>	<b>97</b>
5.3.1	Spatial distribution of SMAF .....	97
5.3.2	Temporal variability of SMAF .....	98
<b>5.4</b>	<b>Discussion</b>	<b>101</b>
5.4.1	Climatic drivers of SMAF .....	101
5.4.2	SMAF and its connection to the SEB .....	103
5.4.3	Outlook: Greenland and the future .....	111
<b>5.5</b>	<b>Conclusions</b>	<b>113</b>
<b>6</b>	<b>Conclusions and outlook</b> .....	<b>115</b>
<b>6.1</b>	<b>Conclusions</b>	<b>115</b>
<b>6.2</b>	<b>Outlook</b>	<b>119</b>
6.2.1	Antarctica's future climate and Greenland .....	119
6.2.2	RACMO2 improvements .....	120
6.2.3	Towards a non-hydrostatic climate model on an adaptive grid ...	121
	<b>Bibliography</b> .....	<b>123</b>
	<b>Publication list</b> .....	<b>141</b>
	<b>Acknowledgements</b> .....	<b>142</b>
	<b>Resume</b> .....	<b>146</b>

## Summary

Along three-quarters of its edge, the Antarctic ice sheet is fringed by ice shelves. These floating extensions of the ice sheet measure 100–2000 metres in thickness. Ice shelves act to buttress the flow of the grounded ice sheet, slowing down the rate at which it is flowing into the ocean. In the recent past, ice shelves have been subject to significant change. In 1995 and 2002, two ice shelves in the Antarctic Peninsula completely disintegrated, permanently redefining Antarctica's coastline. As ice shelves float on the ocean, their disappearance does not directly contribute to sea-level rise. However, when ice shelves disappear, so does their buttressing effect on the grounded ice sheet. This causes the ice sheet to flow into the ocean at a faster rate, which raises global mean sea level. Therefore, the mass loss of the grounded Antarctic ice sheet, and therewith its contribution to global mean sea level rise, strongly depends on the conditions of its surrounding ice shelves.

An ice shelf is susceptible to a process called 'hydrofracturing'. This occurs when snow melts at the ice-shelf surface, forming melt ponds. The meltwater can fill pre-existing crevasses, and because of the water pressure the crevasses can become deeper. Eventually, the crevasse can reach the bottom of the ice shelf. If snowmelt is widespread on the ice-shelf surface, meltwater can fill crevasses over the entire ice shelf, potentially destabilising the ice shelf, causing it to disintegrate.

Climate scientists want to understand how the climate has evolved over the past decades, and how it will evolve in the future. There are several ways to study the climate. With weather stations, we can measure the meteorological conditions near the surface. However, Antarctica has an extremely harsh climate, and as a result, such observations are scarce. Although some weather stations have been operational for a relatively long period of time (decades), most stations provide data for just a couple of years. In any case, weather stations only provide information for single locations scattered across the ice sheet, usually in more accessible locations.

To fill in these gaps, we use either satellites or climate models. Satellites often observe the full ice sheet, but have a limited operation time

span (typically 5–10 years) and do not measure all quantities of interest, for example melt rates. Climate models do not suffer from these limitations. They come in different degrees of complexity: some models only take the atmosphere into account, some also model changes in ocean circulation or explicitly calculate changes of an ice sheet. Unfortunately, the increased degree of complexity comes at a price: increased computational costs. Therefore, when using climate models, we have to consider which processes should be modelled explicitly, and which processes can be estimated using a simpler parameterisation.

Whether snowmelt occurs is determined by the surface energy balance: the sum of all energy fluxes towards and away from the surface. An important energy source is the absorption of solar radiation. The amount of sunlight that is absorbed by the surface is determined by its reflectivity: the surface albedo. Antarctic snow is pristine white and reflects typically 85 % of the incoming sunlight (i.e. it has an albedo of 0.85). However, when snow melts, it becomes darker, reflecting perhaps 70 %, and thus absorbs two times more solar radiation. If the surface absorbs more energy, more snow can melt, darkening the surface even further. This process is known as the snowmelt–albedo feedback.

Although this is a known process, until recently we did not know how much it affects the amount of snowmelt that occurs in Antarctica. In this thesis, we explicitly model this process and quantify how strongly it influences snowmelt events on the vast Antarctic ice sheet. In Chapter 3, this is first done for a single location, using meteorological observations from a German research station situated on an ice shelf in coastal Dronning Maud Land, East Antarctica. We find that the average annual snowmelt amount is approximately 2.5 times higher than in a simulation in which we do not consider the snowmelt–albedo feedback. Data from several automatic weather stations are used in Chapter 4 to evaluate RACMO2, a regional atmospheric climate model developed in collaboration with the Royal Netherlands Meteorological Institute (KNMI), which is used to study the polar climate. We find that RACMO2 provides reasonable estimates of snowmelt rates: although on average it slightly underestimates snowmelt, the spatial and temporal variability agree well with weather stations and satellite measurements.

Finally, in Chapter 5, we use RACMO2 to study the snowmelt–albedo feedback over the entire Antarctic ice sheet. We identify meteorological conditions that favour this feedback: since fresh snowfall makes the surface bright again, the snowmelt–albedo feedback is more active in seasons with a long dry spell. We furthermore show that the feedback is less active in both the coldest and the warmest parts of the Antarctic ice sheet. This is because in the coldest part, almost no snowmelt occurs in the first place and as a result, the snowmelt–albedo feedback is not activated. On the other hand, in the warmer regions, snowmelt is no longer solely driven by the absorption of sunlight, but also by warm air that heats the surface directly. This process is not dependent on the surface albedo and therefore the snowmelt–albedo feedback is weaker.

These results show that it is worth the extra computational costs to explicitly calculate the surface albedo and snowmelt. A simpler, more straightforward snowmelt parameterisation can yield similar Antarctica-wide totals, but lacks the spatial and temporal variability that is related to the snowmelt–albedo feedback. In a warming climate, more parts of the Antarctic ice sheet will be susceptible to this feedback, including its largest ice shelves. Using an explicit albedo model is crucial if we want to predict when the circumstances on these ice shelves become favourable for surface melt leading to hydrofracturing, and more importantly, when we have reached the moment in time that we can no longer prevent this from happening.

## Samenvatting in het Nederlands

Kun jij je nog herinneren waar je was op 12 juli 2017? Op die dag werd ijsberg A-68 geboren: een grote ijsberg die afbrak van de Antarctische ijskap. Of wat dacht je van 9 februari 2020? Die dag werd een nieuw temperatuurrecord gevestigd op Antarctica: bijna  $+21^{\circ}\text{C}$ . Deze gebeurtenissen zijn momenteel heel zeldzaam en daarom noemenswaardig, maar het klimaat is sterk aan het veranderen. De atmosfeer warmt op, de oceanen warmen op en de mondiale zeespiegel stijgt. Als deze veranderingen doorzetten zullen zulke gebeurtenissen vaker voorkomen en op meer plekken. In het ergste geval zullen we er niet eens meer naar omkijken als een deel van de ijskap afbreekt.

De Antarctische ijskap wordt voor driekwart omringd door ijsplaten. Dit zijn drijvende uitlopers van de ijskap van 100–2000 meter dik. Ijsplaten geven steun aan de grondgebonden ijskap: dat deel van de ijskap dat op het land ligt. Door de aanwezigheid van ijsplaten stroomt het grondgebonden ijs minder snel de oceaan in. Ijsplaten hebben recent significante veranderingen ondergaan. In 1995 en in 2002 zijn twee ijsplaten in het Antarctisch Schiereiland volledig opgebroken. Dit heeft de kustlijn van Antarctica permanent veranderd. Omdat ijsplaten op het oceaanooppervlak drijven, dragen ze niet direct bij aan mondiale zeespiegelstijging wanneer ze verdwijnen. Ze hebben daarentegen wel een indirect effect op de mondiale zeespiegel: wanneer een ijsplaat verdwijnt, verdwijnt ook het afremmende effect op de grondgebonden ijskap. Het massaverlies van de Antarctische ijskap is daarom sterk afhankelijk van de toestand van de omringende ijsplaten.

Ijskappen kunnen opbreken als gevolg van ‘hydrofractie’. Wanneer aan het oppervlak sneeuw smelt, kan dit smeltwatermeren vormen. Dit smeltwater kan zich verzamelen in aanwezige gletsjerspleten, die daardoor kunnen opvullen. Door de waterdruk van het smeltwatermeer kan de spleet verder uitdiepen en eventueel de ijsplaat verticaal doorklieven. Wanneer er veel smeltwater aanwezig is op het oppervlak van een ijsplaat en er veel gletsjerspleten zijn, kan de ijsplaat instabiel worden, waardoor deze volledig opbreekt.

Als klimaatwetenschappers willen we graag begrijpen hoe het klimaat in de afgelopen decennia is veranderd, maar ook hoe het zich in de toekomst zal ontwikkelen. Er zijn meerdere manieren om het klimaat te bestuderen. Weerstations stellen ons in staat om de meteorologische omstandigheden aan het oppervlak te meten. Aangezien Antarctica een zeer ruig klimaat kent, zijn weerstations op de ijskap schaars. Enkele stations hebben over een relatief lange periode metingen verricht, maar de meeste stations hebben data van slechts enkele jaren. Weerstations geven hoe dan ook slechts informatie over geïsoleerde plekken op de ijskap, meestal in de meest toegankelijke gebieden.

Deze gaten kunnen we opvullen door satellieten en klimaatmodellen te gebruiken. Satellieten leveren vaak informatie over de volledige ijskap, maar slechts voor een relatief korte periode (normaliter 5–10 jaar). Daarnaast meten ze niet alle relevante componenten, zoals smelthoeveelheden. Klimaatmodellen zijn daarentegen in staat alle gewenste componenten te berekenen, en voor elke gewenste periode. Ze komen dan ook in verschillende soorten en maten: sommige modelleren alleen de atmosfeer, andere nemen ook oceaanstromingen mee, of modelleren expliciet de veranderingen van een ijskap. Helaas is het niet gratis om een klimaatmodel complexer te maken: hoe complexer, des te meer rekenkracht ervoor benodigd is. Daarom is het noodzakelijk de gulden middenweg te vinden: welke processen moeten expliciet worden berekend, en voor welke processen volstaat een simpelere beschrijving?

Het smelten van sneeuw wordt fysisch bepaald door de oppervlakte-energiebalans: de som van alle energiestromen die naar het oppervlak toe of van het oppervlak af zijn gericht. Een belangrijke term is de absorptie van zonlicht. Hoeveel zonlicht wordt geabsorbeerd door het oppervlak is afhankelijk van de reflectiviteit: het albedo. Je hoeft echter niet in Antarctica te zijn om dit te ervaren: wanneer je over het strand loopt, heb je waarschijnlijk je schoenen uitgedaan en loop je blootsvoets door het zand. Maar wanneer je van het zand afstapt en de boulevard oversteekt over het zwarte asfalt, heb je er waarschijnlijk spijt van dat je niet even gauw je schoenen hebt aangedaan: het zwarte asfalt brandt en doet pijn aan je voetzolen.

Hetzelfde gebeurt op een besneeuwd oppervlak: Antarctische sneeuw is maagdelijk wit en reflecteert doorgaans 85 % van het inkomende zonlicht; met andere woorden, het heeft een albedo van 0.85. Smeltende sneeuw verlaagt het albedo: een smeltend oppervlak kan wel twee keer zo veel zonlicht absorberen. Wanneer het oppervlak meer energie absorbeert, is er ook meer energie beschikbaar om de sneeuw verder te doen smelten, waardoor het albedo nog verder verlaagd wordt. Dit heet de smelt–albedo terugkoppeling.

Dit is een bekend proces, maar tot voor kort wisten we niet hoeveel invloed het heeft op de smelthoeveelheden in Antarctica. In dit proefschrift hebben we dit proces expliciet gemodelleerd, en de invloed op smeltende sneeuw op de Antarctische ijskap gekwantificeerd. Dit hebben we eerst gedaan voor een enkele locatie (hoofdstuk 3) door gebruik te maken van meteorologische waarnemingen van een Duits onderzoeksstation gelegen op een ijsplaat in Koningin Maudland in Oost-Antarctica. Met deze data ontdekken we dat de gemiddelde jaarlijkse smelthoeveelheid met een factor 2,5 toeneemt wanneer de smelt–albedo terugkoppeling wordt meegenomen in de berekeningen. In hoofdstuk 4 gebruiken we waarnemingen van verschillende automatische weerstations om RACMO2 te evalueren: een regionaal atmosferisch klimaatmodel dat samen met het Koninklijk Nederlands Meteorologisch Instituut is ontwikkeld om het klimaat van poolgebieden te bestuderen. Hier ontdekken we dat RACMO2 goed in staat is om de waargenomen smelthoeveelheden te reproduceren. Ook al onderschat gemiddeld genomen het model de smelthoeveelheden enigszins, variaties in tijd en ruimte komen goed overeen met de weerstation-data en satellietmetingen.

Uiteindelijk gebruiken we RACMO2 in hoofdstuk 5 om de smelt–albedo terugkoppeling over de gehele Antarctische ijskap te bestuderen. Dit stelt ons in staat om de meteorologische omstandigheden te identificeren die deze terugkoppeling faciliteren. Aangezien verse sneeuw het oppervlak wit maakt, is de terugkoppeling actiever in seizoenen die een lange droge periode kennen. We zien ook dat zij minder actief is in zowel de koudste als de warmste delen van de ijskap. Dit is omdat er nauwelijks smelt optreedt in de koudste delen van de ijskap, waardoor de terugkoppeling überhaupt niet geactiveerd wordt. In de warmste delen daarentegen speelt de

absorptie van zonlicht een kleinere rol voor het smelten van sneeuw. Het oppervlak wordt hier niet alleen opgewarmd door de zon maar ook door warme lucht die eroverheen stroomt. Aangezien dit proces het albedo niet beïnvloedt, is de terugkoppeling hier ook minder sterk.

De resultaten van dit proefschrift laten zien dat het de extra rekenkracht waard is om het albedo van het oppervlak en sneeuwsmeelt expliciet te modelleren. Een meer rechttoe rechtaan model zou in principe vergelijkbare waardes kunnen opleveren voor de totale hoeveelheid sneeuwsmeelt op de Antarctische ijskap. Dit model zou echter tekortschieten in het in kaart brengen van de variabiliteit in ruimte en tijd als gevolg van de smelt–albedo terugkoppeling. In een opwarmend klimaat zoals we dat nu zien, zal een groter deel van de Antarctische ijskap gevoelig worden voor de smelt–albedo terugkoppeling, inclusief de grootste Ross en Filchner-Ronne ijsplaten. Een expliciet albedomodel is dan ook onmisbaar wanneer we de omstandigheden op de ijsplaten willen voorspellen die gunstig zijn voor sneeuwsmeelt en het daaraan gerelateerde opbreken van ijsplaten. Maar nog belangrijker: het stelt ons in staat om te voorspellen onder welke omstandigheden we niet meer in staat zijn om de afbrekende ijsplaten en de daarmee samenhangende zeespiegelstijging te voorkomen.

## Samevatting in 't Limburgs

Kins doe dich nog herinnere woeë se woors op 12 juli 2017? Op dae daag waas iesberg A-68 gebaore: 'ne groeëte iesberg dae aafbrook van de Antarktische ieskap. Of waat dachs se van 9 februari 2020? Toen waerdje 'n nuuj temperatuurrecord gevestigdj op Antarctica: bienao +21°C. Dees gebäörtenise zeen momenteel hieël zeldzaam en daoróm neumenswaerdig, mer 't klimaat is sterk aan 't verangere. De atmosfeer wermtj op, de oceane werme op en de mondiale zieëspiegel stijgtj. As dees verangeringe doorzette, zulle zó'n gebäörtenise vaker väörkómme en op mieër plekke. In 't ergste geval zulle wae d'r neet ins mieër nao ómkieke as 'n deil van de ieskap aafbrèktj.

De Antarktische ieskap is väör driekwart ómringdj door iesplate. Dit zeen drievevondje oetloupers van de ieskap van 100–2000 maeter diek. Iesplate gaeve steun aan de gróndjgebónje ieskap: det deil van de ieskap det op 't landj ligktj. Door de aanwezigheid van iesplate struimtj 't gróndjgebónje ies minder snel de oceaan in. Iesplate höbbe recent significante verangeringe óngergaon. In 1995 en in 2002 zeen twieë iesplate in 't Antarktisch Schiereilandj gans opgebraoke. Dit haet de kustlien van Antarctica permanent verangerdj. Ómdet iesplate op 't oceaanoppervlak drieve, drage ze neet drek bie aan de mondiale zieëspiegelstijging as ze verdwiene. Ze höbbe waal 'n indirek effect op de mondiale zieëspiegelstijging: as 'n iesplaat verdwientj, verdwientj ouch 't aafremmendje effect op de gróndjgebónje ieskap. 't Massaverlees van de Antarktische ieskap is daoróm sterk afhankelik van de toestándj van de ómringendje iesplate.

Ieskappe kinne opbraeke as gevólg van 'hydrofractie'. As aan 't oppervlak snieë smèltj, kin dit smèltjwatermere vorme. Dit smèltjwater kin zich verzamele in aanwezige gletsjersplete, die daodoor kinne opvölle. Door de waterdrök van 't smèltjwatermeer kin de spleet wieër oetdepe en eventueel de iesplaat verticaal doorklieve. Wannieër d'r väöl smèltjwater aanwezig is op 't oppervlak van 'n iesplaat en d'r väöl gletsjersplete zeen, kin de iesplaat instabiël waere, woeëdoor deze gans opbrèktj.

As klimaatweitensjappers wille wae gaer begriepere wie 't klimaat in de aafgeloupe decennia is verangerdj, mer ouch wie 't zich in de toekomst zal

ontwikkele. D'r zeen mieërdere manere óm 't klimaat te bestudere. Waerstations stèlle ós in staot óm de meteorologische ómstenj aan 't oppervlak te maete. Aangezeen Antarctica 'n hieël ruig klimaat kentj, zeen waerstations op de ieskap sjaars. 'n Paar stations höbbe äöver 'n relatief lange periode maetinge verrichtj, mer de meiste stations höbbe data van mer inkele jaore. Waerstations gaeve wie den ouch slechts informatie äöver geïsoleerdje plekke op de ieskap, meestal in de meist toegankelike gebiede.

Dees gate kinne wae opvölle door satelliete en klimaatmodelle te gebroeke. Satelliete levere dök informatie äöver de ganse ieskap, mer slechts vöör 'n relatief korte periode (normaal gespraoke 5–10 jaor). Verder maete ze neet alle relevante componente, wie smèltjhoeveelhede. Klimaatmodelle zeen echter in staot alle gewinsdje componente te beraekene, en vöör edere gewinsdje periode. Ze kómme den ouch in versjillendje saorte en maote: sómmige modellere allein de atmosfeer, angere neme ouch oceaanstroominge mèt, of modellere expliciet de verangeringe van 'ne ieskap. Helaas is 't neet gratis óm 'n klimaatmodel complexer te make: wie complexer, wie mieër raekenkracht daovöör benuedigd is. Daoróm is 't noeëdzakelik de gulde middewaeg te vinje: welke processe mótte expliciet waere beraekendj, en vöör welke processe volsteit 'n simpelere besjrijving?

't Smèltje van snieë waertj fysisch bepaoldj door de oppervlakte-energiebalans: de som van alle energiestruime die nao 't oppervlak toe of van 't oppervlak aaf zeen gerichtj. 'n Belangrieke term is de absorptie van zonleecht. Wievööl zonleecht waerdj geabsorbeerdj door 't oppervlak is aafhankelik van de reflectiviteit: 't albedo. Mer doe hoofs neet in Antarctica te zeen óm dit te ervare: wannieër se äöver 't strandj löps, höbs se wersjienlik dien sjoon oetgedaon en löps se op bloeëte veut door 't zandj. Mer zoeë gauw as se van 't zandj aafstaps en de boulevard äöverstèks äöver 't zwarte asfalt, höbs se d'r wersjienlik spiet van des se neet effe gauw dien sjoon höbs aangedaon: 't zwarte asfalt brantj en duit pien aan dien zaole.

't Zelfde geböörtj op 'n besnieëdj oppervlak: Antarctische snieë is maagdelik wit en reflecteertj doorgaons 85 % van 't inkomendje zonleecht; mèt anger wäörd, 't haet 'n albedo van 0.85. Smèltendje snieë verlieëgtj 't albedo: 'n smèltendj oppervlak kin waal twieë kieër zoeë vööl zonleecht

absorbere. Wannieër 't oppervlak mieër energie absorbeertj, is d'r ouch mieër energie besjikbaar óm dae snieë verder te doon smèltje, woeëdoor 't albedo nog wieër verlieëgdj waertj. Dit hètj de smèltj–albedo truukkoppeling.

Dit is 'n bekindj proces, mer toet vöör kort wiste wae neet wievööl invloed 't haet op de smèltjhoeveelhede in Antarctica. In dit proofschrift höbbe wae dit proces expliciet gemodelleerdj, en de invloed op smèltendje snieë op de Antarctische ieskap gekwantificeerdj. Dit höbbe wae ieërst gedaon vöör 'n inkele locatie (hoofdstuk 3) door gebroek te make van meteorologische waarneming van 'n Duits óngerzeuksstation op 'n iesplaat in Koningin Maudlandj in Oeëst-Antarctica. Mèt dees data óntdèktje wae det de gemiddeldje jaorlikse smèltjhoeveelheid mèt 'n factor 2,5 toeneemtj wannieër de smèltj–albedo truukkoppeling waertj mètgenome in de be-raekening. In hoofdstuk 4 gebroeke wae waarneming van versjillende automatische waerstations óm RACMO2 te evaluere: 'n regionaal atmosferisch klimaatmodel det same mèt 't Käöninklik Nederlands Meteorologisch Instituut is óntwikkeldj óm 't klimaat van poolgebiede te bestudere. Hie óntdèkke wae det RACMO2 good in staot is óm de waorgenaome smèltjhoeveelhede te reproducere. Ouch al óngersjatj gemiddeldj genaome 't model de smèltjhoeveelhede 'n bietje, variaties in de tied en ruumdje kome good äöverein mèt de weerstationdata en satellietmaetinge.

Oeteindelik gebroeke wae RACMO2 in hoofdstuk 5 óm de smèltj-albedo truukkoppeling äöver de ganse Antarctische ieskap te bestudere. Dit stèltj ós in staot óm de meteorologische ómstentj te identificere die deze truukkoppeling faciliteere. Aangezeen verse snieë 't oppervlak wit meuktj, is de truukkoppeling actiever in seizoene die 'n lange druuege periode kinne. Wae zeen ouch det 't minder actief is in zoeëwaal de kaodste as de wermste deile van de ieskap. Dit is ómdet d'r nauweliks smèltj optreutj in de kaojste deile van de ieskap, woeëdoor de truukkoppeling überhaupt neet geactiveerdj waertj. Aan de angere kantj speeltj in de wermste deile de absorptie van zonleecht 'n kleinere rol vöör 't smèltje van snieë. 't Oppervlak waertj hie neet allein opgewermdj door de zon mer ouch door de werme lócht die d'r äöverhaer struimtj. Aangezeen dit proces 't albedo neet beïnvlootj, is de truukkoppeling hie ouch minder sterk.

De resultate van dit proofschrift laote zeen det 't de extra kóste waerd is óm 't albedo van 't oppervlak en snieësmèltj expliciet te modellere. Mèt 'n mieër rechtoe rechaan model zoj men in principe vergeliëkbare waerdes kinne verkiege vöör de totale hoeveelheid snieësmèltj op de Antarctische ieskap. Dit model zoj den waal tekortsjete in 't in kaart bringe van de variabiliteit in ruumdje en tied as gevolg van de smèltj–albedo truukkoppeling. In 'n opwermendj klimaat wie wae det noe zeen, zal 'n groeëter deil van de Antarctische ieskap geveulig waere vöör de smèltj–albedo truukkoppeling, inclusief de groeëtste Ross en Filchner-Ronne iesplate. 'n Expliciet albedomodel is den ouch ónmisbaar wannieër wae de ómstenj op de iesplate wille vöörspelle die gunstig zeen vöör snieësmèltj en 't dao aan gerelateerdje opbraeke van iesplate. Mer nog belangrieker: 't stèltj ós in staot óm te vöörspelle ónger welke ómstenj wae neet mieër in staot zeen óm de aafbraekendje iesplate en de daomèt samehangendje zieëspegelstijging te vöörkómme.



# 1. Introduction

## 1.1 Sea level rise

Since the industrial revolution, global mean sea level has been gradually rising. This is a looming threat for millions of people across the world, living in island states such as the Maldives or the Marshall Islands, in deltas such as in India or Bangladesh, in countries with heavily built-up coastal areas such as the United States, and in countries situated partly below sea level, such as the Netherlands. The current (2006–2015 average) estimated rate of sea level rise is  $3.00 \pm 0.38 \text{ mm yr}^{-1}$  (Oppenheimer et al., 2019) and it is accelerating: the Intergovernmental Panel on Climate Change expects the global mean sea level in 2100 to be 0.29–1.1 m higher than it is today (Oppenheimer et al., 2019). This large bandwidth is only partly a result of model uncertainties and incomplete measurements. The biggest uncertainty is related to the followed warming scenario: whether humanity is capable of recognising the urgency of climate change, and will adopt and implement effective climate mitigation policies.

Contemporary global mean sea level rise is mainly driven by the warming and expanding seawater, responsible for almost half of the observed signal (Cazenave and Meyssignac, 2018). The rest is primarily caused by the melting of the Earth's glaciers, ice caps and ice sheets. Together with permafrost and sea ice, this is collectively known as the cryosphere. The individual contributions of the ice sheets to contemporary sea level rise are presented in Fig. 1.1. Table 1.1 shows the volumes of the ice sheets and glaciers, as well as their current and potential contributions to global mean sea level rise. Ice masses contribute to sea level rise primarily in two ways. Increased surface melting of snow and ice results in increased melt-water runoff into the ocean; most mountain glaciers contribute to sea level

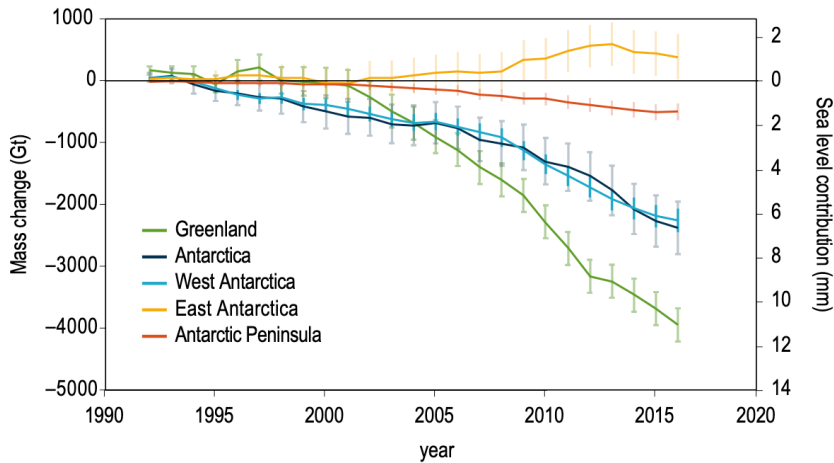


**Figure 1.1** Recent mass loss and contributions to global mean sea level rise of the Greenland and Antarctic ice sheets (Meredith et al., 2019).

rise this way, but also (parts of) ice caps that are not terminating in the ocean. The other way is through basal melt from floating glaciers, iceberg calving and subsequent melting of icebergs. This occurs at the terminus of marine-terminating glaciers and ice sheets.

## 1.2 Surface Mass Balance

In order to determine the state of a glacier or ice cap/sheet, we introduce the Mass Balance ( $MB [Gt yr^{-1}]$ ):

$$MB = SMB - D, \quad (1.1)$$

where  $SMB$  is the Surface Mass Balance and  $D$  represents the discharge of ice over the grounding line: the location where the grounded ice sheet starts to float. The  $SMB$  is the sum over the grounded part of all fluxes that add mass to and remove mass from the ice surface:

$$SMB = PR - RU - SU - ER, \quad (1.2)$$

**Table 1.1** Total ice volume, Potential Sea-Level Equivalent (SLE) and Sea Level Rise (SLR) for the Antarctic and Greenland ice sheets and the remaining glaciers and ice caps. Antarctic ice volume only includes the volume above flotation, the part that contributes to sea level rise. SLE: potential contribution to global mean sea level when melted completely. SLR: estimated contribution to 2006–2015 global mean sea level rise. Glaciers include the peripheral glaciers and ice caps of the Antarctic and Greenland ice sheets. Data from Morlighem et al. (2017); Farinotti et al. (2019); Meredith et al. (2019); Morlighem et al. (2020).

	Total ice volume (km <sup>3</sup> )	Potential SLE (m)	SLR (mm yr <sup>-1</sup> )
Antarctica	$22.8 \pm 0.4 \cdot 10^6$	$57.9 \pm 0.9$	$0.43 \pm 0.09$
Greenland	$2.74 \pm 0.02 \cdot 10^6$	$7.42 \pm 0.05$	$0.77 \pm 0.05$
Glaciers	$158 \pm 41 \cdot 10^3$	$0.32 \pm 0.08$	$0.61 \pm 0.08$

where PR is total precipitation (solid and liquid), RU is meltwater runoff, SU is sublimation and ER is erosion due to drifting snow. Runoff is surface meltwater that is not retained or refrozen in the subsurface snow layers and is transported away. Drifting snow erosion is caused by wind transporting more snow away from a certain location than it imports. Averaged over an entire ice sheet this is a small component, as there is only a net removal of snow occurring at the ice sheet edge. However, locally this can lead to significant erosion or deposition of snow (Lenaerts and Van den Broeke, 2012). Estimates of the various components of the SMB for the Antarctic ice sheet (AIS) and Greenland ice sheet (GrIS) are presented in Table 1.2.

The table shows that the AIS and GrIS are very different. Almost no runoff occurs on the AIS, although there is significant snowmelt occurring along the ice sheet margins. This means that almost all meltwater refreezes in the layer of compressed snow, called firn, which therefore acts as a buffer for meltwater runoff. As a result, sublimation is the most significant mass loss term. Sublimation removes only about 6 % of the total amount of precipitation, and therefore most snow remains at the surface, leading to a high positive average SMB. The GrIS, on the other hand, experiences more runoff, totalling about one-third of the annual precipitation. As the GrIS is situated in a warmer climate than the AIS, more surface melt occurs.

**Table 1.2** Annual average SMB and components (in  $\text{Gt yr}^{-1}$ ) for the Antarctic ice sheet (AIS, including ice shelves) and the Greenland ice sheet (GrIS). The average SMB values for the AIS cover 1979–2014 (Van Wessem et al., 2018), those for the GrIS cover 1972–2012 (Noël et al., 2018b, 2020b).

SMB component	AIS	GrIS
Precipitation	2773	712
Snowmelt	112	412
Runoff	4	245
Sublimation	169	33
Snowdrift erosion	7	0
Total SMB	2595	434

In summer, about 10 % of the surface of the GrIS consists of bare ice, the ablation zone, where the meltwater runs off without much delay. As a result, only 60 % of the annual average precipitation remains at the ice-sheet surface. Noël et al. (2019) show that the refreezing capacity of the interior GrIS is gradually decreasing, which causes runoff to become more widespread across the ice sheet.

Rignot et al. (2019) and Mouginot et al. (2019) present MB values for the Antarctic and Greenland ice sheets, respectively. Mouginot et al. (2019) report that in Greenland, the decadal MB has decreased from  $+47 \pm 21 \text{ Gt yr}^{-1}$  in 1972–1980 to  $-286 \pm 20 \text{ Gt yr}^{-1}$  in 2010–2018. Antarctica has seen a similar decrease in MB: Rignot et al. (2019) report a decadal MB of  $-40 \pm 9 \text{ Gt yr}^{-1}$  in 1979–1990, compared to  $-252 \pm 26 \text{ Gt yr}^{-1}$  in 2009–2017. Given the larger size of Antarctica compared to Greenland, these numbers indicate that the GrIS is experiencing faster and relatively more significant mass loss.

Although the AIS experiences almost no runoff, surface melt is an important process for the current state and the future of the ice sheet. This is because of the presence of ice shelves along a large part of the AIS: floating extensions of the grounded ice sheet that provide a buttressing effect to the AIS, slowing down its flow into the ocean. The next sections introduce Antarctica and the AIS, and discuss how surface melt affects ice-shelf stability.

## 1.3 The Antarctic ice sheet

### 1.3.1 Geographical description

The AIS has an eight-times larger volume and hence potential contribution to global mean sea level rise than the GrIS (Table 1.1). Still, its current contribution to global mean sea level rise (2006–2015) is only 45 % of that of Greenland (Meredith et al., 2019). The main reason for this is the much colder climate of Antarctica. Antarctica is located farther poleward than Greenland, including the geographical South Pole and with its most northerly point at almost  $63^{\circ}\text{S}$  (Fig. 1.2). It furthermore has a higher average surface elevation. Its climate is influenced by the Antarctic Circumpolar Current, the largest ocean current on Earth (Kennett, 1977). This current flows west to east in the Southern Ocean, fully encircling the Antarctic continent. Warm ocean waters or atmospheric currents cannot easily reach the continent and as a result, the continent can maintain its low

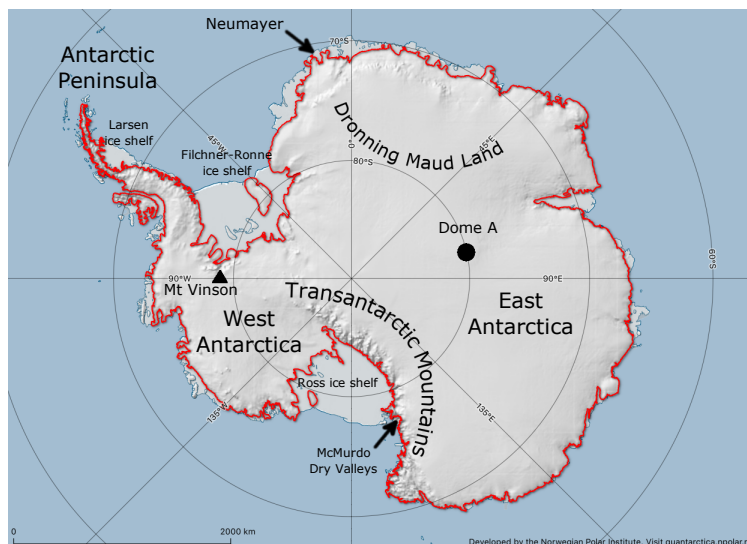


**Figure 1.2** Map of Antarctica, indicating some regions used throughout this thesis. The red line indicates the grounding line.

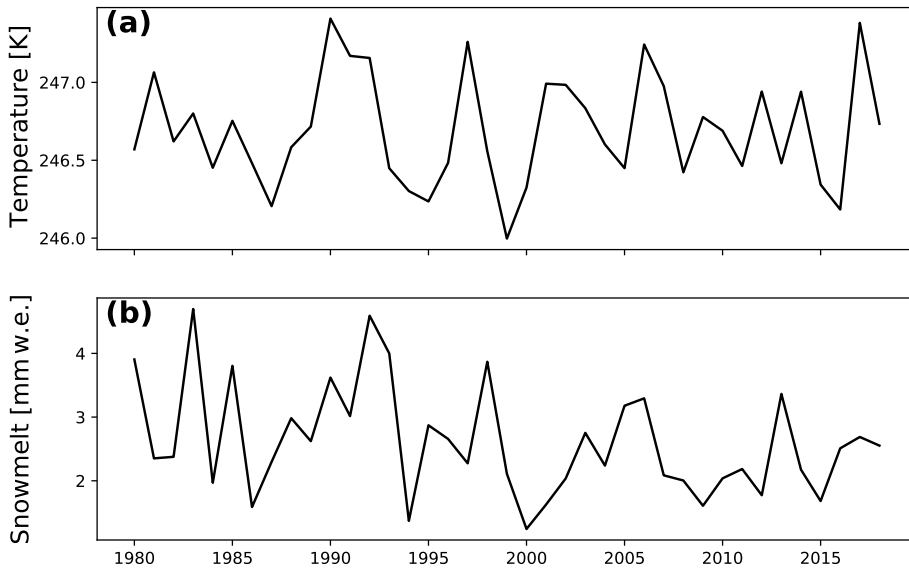


**Figure 1.3** Time series of annual average **(a)** temperature and **(b)** snowmelt as modelled by RACMO2 (Van Wessem et al., 2018), averaged over the entire AIS (including ice shelves).

temperatures (Martinson, 2012). The increase in average global temperature is therefore not yet reflected clearly in Antarctic near-surface air temperatures and surface melt rates (Fig. 1.3). A 3 K increase in average air temperature has been observed in the Antarctic Peninsula before 1990 (Meredith and King, 2005), but this trend has reversed since (Van Wessem et al., 2015; Turner et al., 2016). Combined with increased ocean temperatures, this forced the glaciers in the western AP to retreat (Cook et al., 2016). A similar decadal temperature variability has been observed at the South Pole (Nicolas and Bromwich, 2014), which recently warmed up again (Clem et al., 2020).

The Antarctic ice sheet (AIS) covers almost 14 million km<sup>2</sup>, or approximately 98 % of the Antarctic continent. Antarctica is usually divided into three regions: East Antarctica, West Antarctica and the Antarctic Peninsula (AP) (see Fig. 1.2). At its highest point, the ice sheet reaches an altitude of more than 4 km above sea level (Dome A), although the highest

point of Antarctica is Mount Vinson in West Antarctica (4892 m). The average ice sheet thickness is  $\sim 2$  km, with the thickest ice measuring almost 5 km (Fretwell et al., 2013). Along  $\sim 74\%$  of its coastline, the AIS is surrounded by floating ice shelves: extensions of the grounded ice sheet that are hundreds of metres thick. These are discussed in more detail in Sect. 1.3.3.

### 1.3.2 Climatology

The near-surface climate of Antarctica is characterised by low temperatures, low specific humidity and little absorbed solar radiation due to the Sun's low elevation above the horizon in combination with the ice sheet's highly reflective surface. A characteristic feature of ice masses is the occurrence of katabatic winds (Bromwich, 1989; King, 1998; Van den Broeke et al., 1999). Due to radiative cooling, the near-surface air cools and will flow to lower elevations. In West and East Antarctica, this results in a flow from the high ice-sheet interior towards the coast.

To illustrate some characteristics of the Antarctic climate, Fig. 1.4 shows the average 2 m air temperature (**a**), 500 hPa geopotential (**b**), annual precipitation (**c**) and snowmelt (**d**) as modelled by the regional climate model RACMO2 (Van Wessem et al., 2018). The coldest part of Antarctica is the East-Antarctic plateau, where the average annual temperature is as low as  $-50^\circ\text{C}$ . The AP is the warmest part, where the average annual temperature reaches  $-5^\circ\text{C}$ . The western AP is substantially warmer than the eastern part, a result of the dominant atmospheric flow patterns and local topography: up to 2000 m high, a steep mountain range divides the AP in an eastern and western part. Furthermore, changes in ocean currents have increased the heat transport towards West Antarctica and the western AP (Martinson et al., 2008). As a result, the western AP and coastal West Antarctica have experienced a strong warming signal, causing retreating glaciers and ice shelves (Bromwich et al., 2012; Turner et al., 2013). Figure 1.4b shows the average 500 hPa geopotential height, which illustrates that the large-scale flow around Antarctica is largely zonal and westerly. This leads to warm conditions in the western AP, where this flow meets

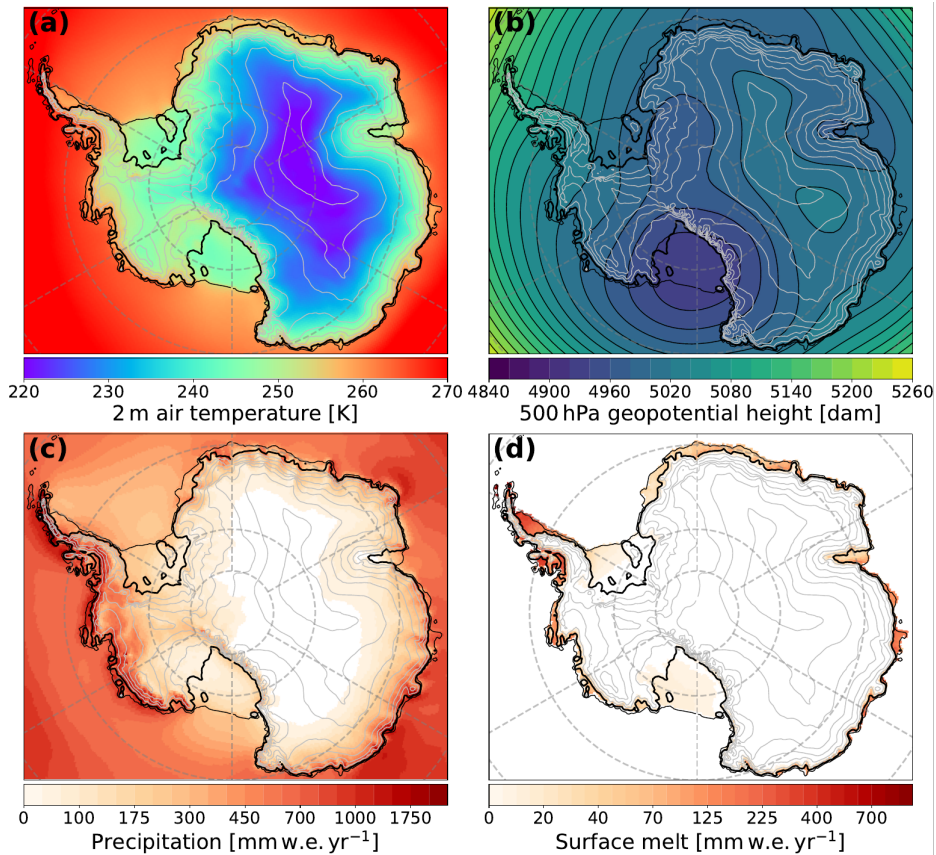


**Figure 1.4** Period-average (1979–2018) **(a)** temperature, **(b)** 500 hPa geopotential height, **(c)** precipitation and **(d)** snowmelt as modelled by RACMO2 (Van Wessem et al., 2018).

the AP mountain range; the eastern AP is colder because of predominantly southerly near-surface barrier winds (Turner et al., 2002).

As a result of this westerly flow in combination with the continent’s high elevation, most depressions do not reach far inland. Therefore, precipitation rates are very low in the ice-sheet interior (Fig. 1.4c), which is classified as a polar desert: some areas receive less than 50 mm w.e. of precipita-

**Table 1.3** Mass balance in  $\text{Gt yr}^{-1}$  ( $\text{Gt} = \text{gigaton}$ ) for the East Antarctic ice sheet (EAIS), West Antarctic ice sheet (WAIS), Antarctic Peninsula (AP) and the entire grounded Antarctic ice sheet (AIS) (Shepherd et al., 2018).

Area	1992–2017	2012–2017
EAIS	$5 \pm 46$	$-28 \pm 30$
WAIS	$-94 \pm 27$	$-159 \pm 26$
AP	$-20 \pm 15$	$-33 \pm 16$
AIS	$-109 \pm 56$	$-219 \pm 43$

tion per year<sup>1</sup> (displayed in white in Fig. 1.4c). The McMurdo Dry Valleys, located in the Transantarctic Mountains, constitute the largest ice-free region of Antarctica (Fountain et al., 2010). This is a result of the low precipitation amounts in combination with strong sublimation by Föhn: a warm, dry wind that transports mild, dry air into the valleys (Speirs et al., 2010). Most precipitation falls in the AP, where average annual amounts on the west side can exceed  $2000 \text{ mm w.e. yr}^{-1}$ .

Figure 1.4d shows the average snowmelt in Antarctica. Almost no snowmelt occurs on most of the grounded AIS ( $<5 \text{ mm w.e. yr}^{-1}$  displayed in white in Fig. 1.4d). Only in a small band around the ice sheet are conditions favourable for snowmelt to occur, mostly constrained to the low-lying ice shelves. Relatively high snowmelt rates are observed in the AP, locally exceeding  $750 \text{ mm w.e. yr}^{-1}$ . However, because of the below-freezing temperatures in combination with high precipitation rates, nearly all melt-water refreezes in the sub-surface snow layers (Van Wessem et al., 2018).

The three Antarctic regions (Fig. 1.2) each have different MB signatures (Table 1.3). Although there is no trend observed in air temperature and surface-melt rates (Fig. 1.3), there is a recent significant acceleration in mass loss from all regions. This mass loss is mainly driven by increased ice discharge through thinning and disappearance of ice shelves (see next section), caused partly by the warming ocean. So far, the East Antarctic

<sup>1</sup>Millimeter water equivalent, allowing a direct comparison of water, snow and ice amounts.

ice sheet is the least affected by global warming and shows only a moderate decrease in MB. However, increased ice flow and mass loss have been observed at Totten Glacier (Li et al., 2016), the largest outlet glacier of East Antarctica, with a total volume representing a global mean sea level change of 3.9 m.

### 1.3.3 Ice shelves

The largest difference between the Greenland and Antarctic ice sheets is the presence of ice shelves around ~74 % of the AIS (Bindshadler et al., 2011) (Fig. 1.5). These extensions of the grounded ice sheet float on the ocean surface and buttress the grounded ice sheet, slowing its flow rate into the ocean. Their thickness typically ranges from more than 1 km near the grounding line to about two hundred metres at the calving front (Griggs and Bamber, 2011). As ice shelves are floating, they do not directly

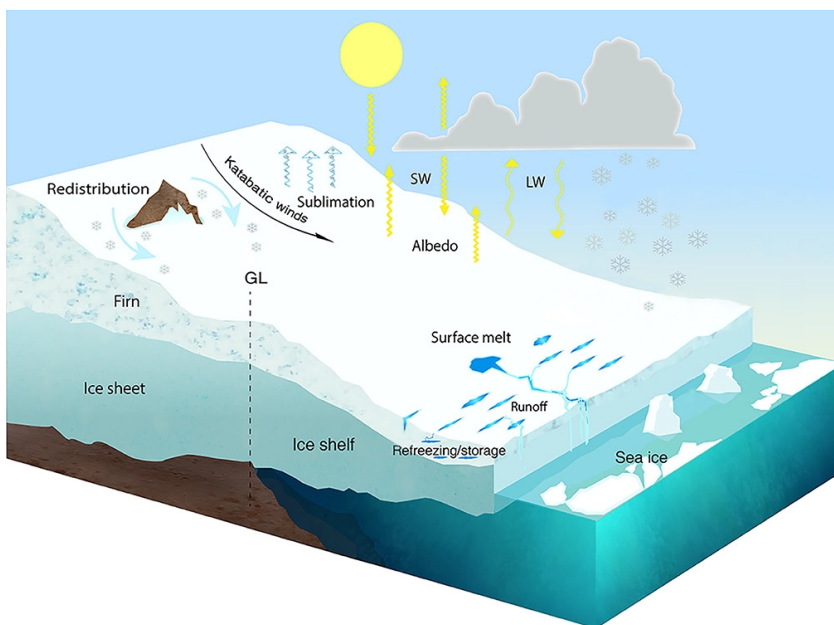


**Figure 1.5** Schematic of an ice shelf and relevant processes, based on Lenaerts et al. (2019).

contribute to sea level rise when they thin or disintegrate. However, these processes trigger a seaward acceleration of the ice flow of the grounded ice sheet (Scambos et al., 2004). This leads to an increased flux of ice entering the ocean, raising global mean sea level. Rott et al. (2011) show that years after ice-shelf disintegration, the tributary glaciers still exhibit an increased ice flow velocity.

Ice-shelf thinning can lead to a retreat of the grounding line, which can in turn trigger a process known as Marine Ice Sheet Instability (MISI). This instability arises because the flux of ice at the grounding line is proportional to the local ice thickness (Weertman, 1974; Schoof, 2007). Consider a grounding line that is located on a bedrock that slopes downwards away from the ice shelf calving front, a so-called ‘retrograde’ bed. If the grounding line were to retreat, the ice thickness increases and consequently so does the ice flux. This locally thins the ice sheet, leading to a further retreat of the grounding line. This retreat stops when the bedrock no longer slopes downwards. Large parts of the West Antarctic ice sheet are considered to be susceptible to MISI (Joughin et al., 2014; Rignot et al., 2014; Favier et al., 2014). Morlighem et al. (2020) show that a significant part of the East Antarctic ice sheet also rests on a retrograde bed, and is therefore susceptible to MISI.

A second mechanism that affects ice-sheet stability has been proposed, the Marine Ice Cliff Instability (MICI) (Bassis and Walker, 2012). This mechanism relies on the hypothesis that an ice-shelf cliff height has a theoretical upper limit. This is a result of the force balance at the ice-shelf terminus, where the pressure exerted by the ice is balanced by the water pressure. As an ice shelf is thicker towards the grounding line, the cliff height increases when an ice shelf retreats. If the ice cliff becomes too high ( $\sim 90$  m), the force balance is no longer met and the cliff will collapse. The effect of MICI on sea-level projections remains a matter of ongoing debate (DeConto and Pollard, 2016; Edwards et al., 2019).

## 1.4 Surface melt

In the previous section, we discussed processes that destabilise the grounded ice sheet when ice shelves retreat, thin or disintegrate. But what causes

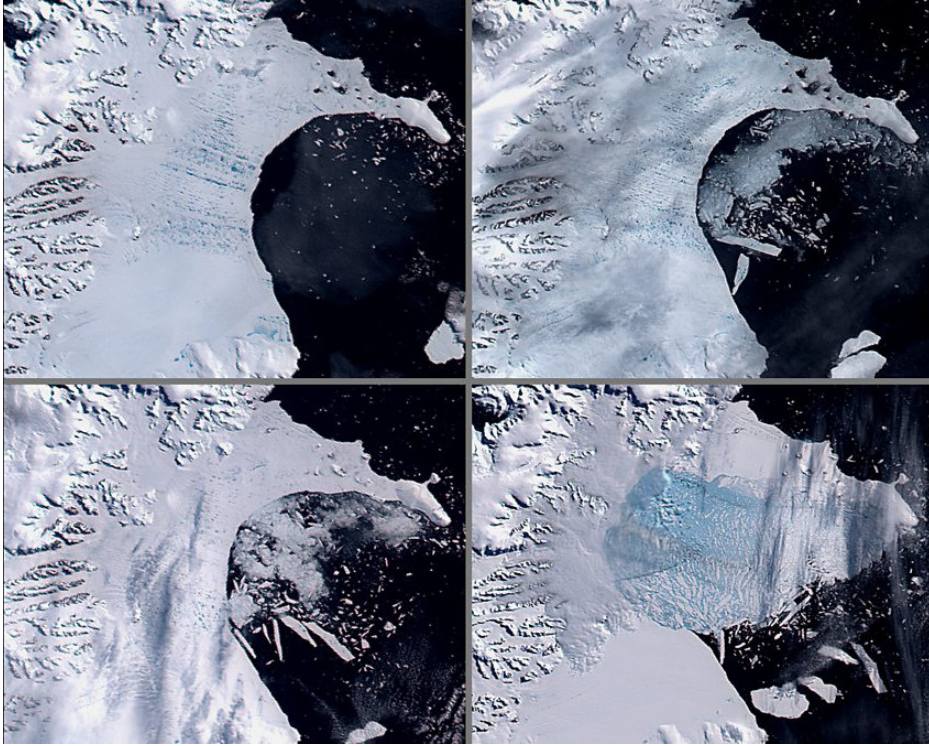


**Figure 1.6** Satellite images of Larsen B disintegrating in 2002 ©NASA. The image top-left was taken on 31 January 2002, bottom-right on 5 March 2002.

ice shelves to suddenly disappear in the first place? This is where surface melt comes into play. Surface melt is widespread on Antarctic ice shelves and was observed as early as 1947 (Kingslake et al., 2017). The accumulation of meltwater in surface ponds can lead to deepening of existing crevasses, due to increased water pressure in the crevasse tip. After sufficient deepening, a crevasse reaches the bottom of the ice shelf or connects to a basal crevasse, a process known as hydrofracturing. This means that there is a close relationship between surface melt and ice-shelf stability.

Based on temperature maps, Cook and Vaughan (2010) suggest the annual  $-9^{\circ}\text{C}$  isotherm as a temperature limit beyond which an ice shelf is no

longer stable. At higher temperatures, the presence of extensive meltwater ponds can trigger hydrofracturing, leading to significant destabilisation and eventual break-up of an entire ice shelf (Scambos et al., 2004; Van den Broeke, 2005). However, on sloping, saturated ice shelves meltwater streams can transport meltwater directly to the ocean (Bell et al., 2017). This potentially slows the destabilisation of the ice shelf, as the meltwater no longer forms melt ponds at the surface.

Morris and Vaughan (2013) and Cook and Vaughan (2010) show that in the northern AP, the  $-9^{\circ}\text{C}$  isotherm crosses between the Larsen B and C ice shelves. Indeed in the recent past, several ice shelves in the AP have disintegrated: Larsen A in January 1995 and Larsen B in February–March 2002 (Fig. 1.6). Vaughan (2008) and Banwell et al. (2013) propose that hydrofracturing was the main cause of these events, in combination with ocean swell (Massom et al., 2018). The lack of sea ice at the ice-shelf calving front increases the flexing effect of ocean swells on the ice shelf, eventually causing it to break because of too high bending stresses.

From an SMB perspective, the AIS is currently of limited importance to global sea level rise: even though surface melt occurs, only a small fraction of meltwater finds its way to the ocean. However, the ice-atmosphere interaction described above affects the ice sheet stability. Therefore, we need to better understand the Antarctic surface melt climate and the relevant processes, if we want to comprehend the current state of the AIS and make predictions about its future.

### 1.4.1 Snowmelt–albedo feedback

The absorption of solar radiation is the most important energy source for surface melt in Antarctica (Jakobs et al., 2020, see also Chapter 4). The amount of absorbed solar radiation depends on the reflectivity of the surface: the surface albedo. The albedo is defined as the ratio of reflected solar radiation to incoming solar radiation, hence a high albedo corresponds to high reflectivity, and low albedo corresponds to high absorption.

The albedo of a snow/ice surface depends on several variables, such as the Sun's elevation above the horizon, cloud cover, the concentration of black

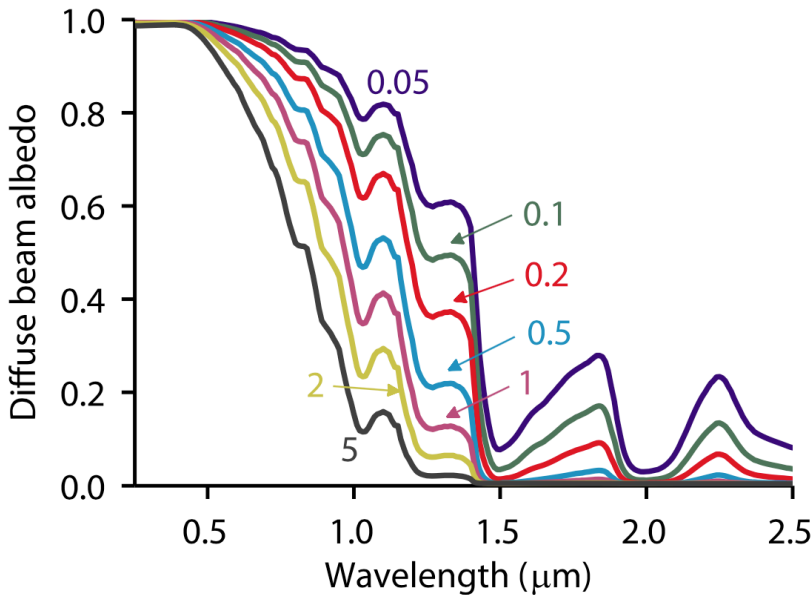


**Figure 1.7** Dependence of spectral surface albedo on incident light wavelength and snow grain size (Gardner and Sharp, 2010). The numbers indicate the grain size in mm.

carbon and the grain size of the snow or ice (Gardner and Sharp, 2010). Snow grains grow through metamorphism or melt, resulting in longer travel paths of photons in the snowpack, which increases the chances of a photon being absorbed. In other words: the surface has a lower albedo (Fig. 1.7).

There are several ways in which surface melt and surface albedo affect each other. For example, when sea ice melts, the ocean itself becomes exposed. As the albedo of water ( $\sim 0.07$ ) is much lower than that of sea ice (0.6–0.8), the ocean can take up more heat (Perovich and Polashen-ski, 2012). Other examples are retreating glaciers revealing the bare rock underneath, or the removal of seasonal snow on tundra. Rock and tundra also have a lower albedo than ice, so these also represent positive feed-backs (Grenfell and Perovich, 2004).

There is another positive feedback, which we call the snowmelt–albedo feedback (SMAF)<sup>2</sup>. After snowmelt, when the temperature of the subsurface snow layers is low enough, the meltwater can refreeze. This occurs when enough pore space is available to accommodate the meltwater. As the meltwater refreezes onto existing snow grains, the snow grains grow, and as a result the albedo decreases (Flanner and Zender, 2006). As the snowpack now absorbs more solar radiation, more energy is available for surface melt. The increased meltwater production in turn leads to an increase of meltwater refreezing in the subsurface snow layers, which further lowers the albedo. This constitutes a positive feedback, in which surface melt leads to more surface melt by a darkening of the surface.

In most studies, albedo feedbacks are quantified as a decrease in average albedo as a result of a 1-K temperature increase (Perovich et al., 2002; Hall, 2004; Flanner et al., 2007; Qu and Hall, 2007). This is practical in the case of disappearing sea ice or glaciers, which act on relatively long time scales in which the system reaches a new steady state. SMAF acts on much smaller scales, both temporal and spatial: snowmelt directly affects the local surface albedo. Until recently, it was unknown how much SMAF affects surface melt rates in Antarctica, and which processes are determining its magnitude.

## 1.5 Thesis outline

This thesis aims to quantify SMAF in Antarctica: by how much is surface melt enhanced by the snowmelt–albedo feedback? We determine this in two ways. First, we use meteorological observations to quantify the effect of SMAF on local surface melt rates, using a surface energy balance model. Next, the spatial variability and large-scale drivers of SMAF in Antarctica are studied with a regional atmospheric climate model.

In the next chapter on Methods (Chapter 2), we first introduce the surface energy balance (SEB), which is the theoretical framework of this thesis (Sect. 2.1). What determines whether or not surface melt occurs, and how

---

<sup>2</sup>SMAF is not yet a commonly accepted acronym, but it is coined in this thesis.

to identify the separate energy contributions? We discuss the different energy sources and sinks, and how they are defined. In Sect. 2.2 we discuss the SEB model, which we use to calculate the SEB components and surface melt rates from observations. The section introduces the equations and approximations that we make, and we identify which observations we require in order to run this model. We furthermore introduce the albedo parameterisation that lies at the basis of the SMAF studies in this thesis. Section 2.3 covers the observations: we describe the automatic weather stations of IMAU, as well as a staffed weather station at Neumayer, which is part of a global network of radiation observations. We discuss the sensors and practical difficulties that must be overcome when performing these observations in the harsh Antarctic climate. Finally, in Sect. 2.4 we discuss regional climate models: the tool we use to calculate continent-wide and long-term estimates of SEB and SMB components. We specifically discuss RACMO2, the climate model used in this thesis.

In Chapter 3 we use observations from a single location to quantify SMAF locally. For this we use Neumayer Station, a staffed research station on Ekström ice shelf in East Antarctica (Fig. 1.2) with a high-quality meteorological observatory. The observations also include high-precision radiation measurements, which serve as the input for the SEB model to calculate surface melt rates (Sect. 3.3). We find that the average surface melt rate at Neumayer is  $50 \text{ mm w.e. yr}^{-1}$ , which is small compared to the average precipitation rate of  $400 \text{ mm w.e. yr}^{-1}$ . As a result, all meltwater refreezes in the cold firn, causing Neumayer Station to have a positive SMB; this is the case for almost the entire AIS. We then turn to the SEB model with the grain-size-dependent albedo parameterisation (Sect. 3.4). SMAF was quantified by comparing a simulation in which the full parameterisation is used, to a simulation in which the contribution of refrozen snow to surface albedo is disabled; we define SMAF as the ratio of the surface melt rates in these simulations. We find that, on average, SMAF enhances surface melt rate at Neumayer by a factor of 2.6. This Chapter is published as Jakobs et al. (2019).

Before we can quantify SMAF on a continental scale, we first need to establish that the regional climate model of choice is able to accurately model surface melt rates in Antarctica. This is the subject of Chapter 4. We first

use observations from nine weather stations across Antarctica to calculate surface melt rates (Sect. 4.3.1), using the same SEB model as in Chapter 3. We find that there are roughly two types of melt events: radiation-driven and turbulence-driven. For most of the AIS, melt events are driven by solar radiation, and melt only occurs when the solar radiation is sufficient to warm the surface to the melting point. In the AP, melt events can also be turbulence-driven: on Larsen C ice shelf, located in the eastern AP, the combination of persistent large-scale westerlies and the mountains can cause Föhn winds, causing melt at the foot of the mountain range (Marshall et al., 2006; Van Lipzig et al., 2008; Cape et al., 2015). These Föhn events can cause significant melt well outside the summer season (King et al., 2015; Kuipers Munneke et al., 2018; Kirchgaessner et al., 2019).

In Sect. 4.4 we use the results to evaluate several melt products: a simple temperature–index model, which linearly relates surface melt to average temperature, the regional climate model RACMO2, and results from the QuikSCAT satellite. We find that temperature–index models are not able to adequately reproduce the different melt signals in the various regions. On the other hand, RACMO2 is able to accurately model surface melt rates ( $R^2 = 0.83$ ), although in some locations melt rates are underestimated. The comparison with the QuikSCAT satellite melt product also shows a good correlation ( $R^2 = 0.92$ ), although part of the data used in this evaluation has been used previously to calibrate the satellite’s melt product (Trusel et al., 2013). The satellite data furthermore show a temporal variability of surface melt that is similar to that modelled by RACMO2. This Chapter is published as Jakobs et al. (2020).

The final step is to use RACMO2 and quantify SMAF on a continental scale. This is covered in Chapter 5. To do this, we performed two dedicated runs with RACMO2: one in which the full albedo parameterisation (Sect. 2.2.4) is used, and one in which the effect of refrozen snow on surface albedo is disabled. The results show that SMAF is largest on East Antarctic ice shelves, and smaller on ice shelves in the AP (Sect. 5.3). We find a relationship between SMAF and average summer air temperature: SMAF seems to be most active in regions with an average summer air temperature of  $265 \pm 2$  K. Investigating individual melt seasons more closely, we identify several climatic drivers for SMAF: the occurrence of prolonged

dry periods, the prevailing air temperatures, and the time between significant snowfall events and the onset of surface melt (Sect. 5.4).

On a final note, we contemplate on the importance of SMAF in a warming climate, and how important it could potentially be in Greenland (Sect. 5.4.3). When temperatures increase, the two largest Antarctic ice shelves, the Filchner-Ronne and Ross ice shelves, can reach the temperature at which SMAF is most active. This could potentially expose these ice shelves to an exponential increase of surface melt. We also predict that SMAF is currently large in a large part of south Greenland, as well as in a narrow band around the ice sheet. This Chapter is published as Jakobs et al. (2021).

## 2. Methods

This chapter introduces the different methods used throughout this thesis. We first introduce the Surface Energy Balance (SEB), which is the theoretical framework that allows us to calculate surface melt rates (Sect. 2.1). After introducing the different SEB components, we discuss the model that we use to perform these simulations (Sect. 2.2). This includes the different parameterisations and approximations that we need in order to be able to calculate the SEB with the available observations. We furthermore introduce the albedo parameterisation which we use to quantify the snowmelt–albedo feedback.

Section 2.3 covers the Automatic Weather Stations (AWS), which provide the data we use as input for the SEB model. The section provides a historical context of in-situ observations in Antarctica by IMAU, the different types of weather stations and the variables they measure. Furthermore, it discusses the challenges of maintaining a weather station in a harsh environment as encountered in Antarctica. Finally, in Sect. 2.4 we introduce RACMO2: the regional climate model that is used to model the climate, SEB and Surface Mass Balance of Antarctica. We describe the history of RACMO2 model development and present the specific choices made for the simulations used in this thesis.

### 2.1 Surface Energy Balance

The Surface Energy Balance (SEB) equation for an infinitesimally thin surface layer of ice or snow is given by:

$$\begin{aligned} SW \downarrow + SW \uparrow + LW \downarrow + LW \uparrow + Q_S + Q_L + Q_G + Q_R &= M \\ SW_{\text{net}} + LW_{\text{net}} + Q_S + Q_L + Q_G &= M, \end{aligned} \quad (2.1)$$

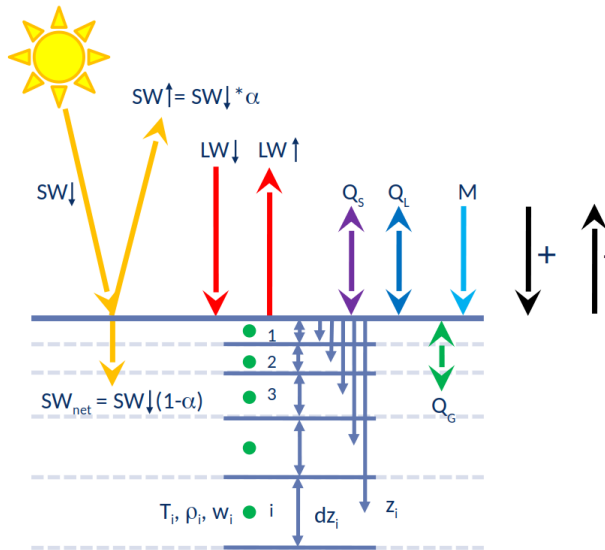


**Figure 2.1** Schematic overview of the SEB.

in which by convention, positive fluxes are directed towards the surface (Fig. 2.1).  $SW_{\text{net}}$  and  $LW_{\text{net}}$  are the net short-wave (solar) and long-wave (terrestrial) radiation fluxes. Both of these are composed of two components:  $SW_{\text{net}} = SW\downarrow + SW\uparrow$ , with  $SW\downarrow$  the incoming solar radiation and  $SW\uparrow$  the reflected solar radiation. The albedo  $\alpha$  is the shortwave reflection coefficient of the surface (for  $SW\downarrow > 0$ ):  $\alpha = -\frac{SW\uparrow}{SW\downarrow}$ . Similarly,  $LW_{\text{net}} = LW\downarrow + LW\uparrow$ , where  $LW\downarrow$  is the long-wave radiation emitted by the atmosphere and  $LW\uparrow$  is the long-wave radiation emitted by the surface.

$Q_S$  and  $Q_L$  are the turbulent fluxes of sensible and latent heat. These energy fluxes represent the vertical turbulent transport of heat and moisture towards or away from the surface. The sensible heat flux is the result of warm (cold) air exchanging heat with the surface, providing (extracting) energy to (from) the surface. This flux depends among others on the temperature gradient between the air and the surface. The latent heat flux for freezing conditions is associated with sublimation or deposition, which depends on the gradient of specific humidity. As the surface is fully saturated, sublimation occurs most of the time, extracting energy from the

surface. In humid circumstances, deposition of ice onto the surface can occur.

$Q_S$  and  $Q_L$  are given by

$$Q_S = -\rho c_p (\overline{w'\theta'})_s \quad (2.2)$$

$$Q_L = -\rho L (\overline{w'q'})_s \quad (2.3)$$

respectively. An overbar ( $\overline{\quad}$ ) indicates a time average, the subscript 's' denotes surface values, and a prime (') indicates the turbulent fluctuations, i.e. the deviations from the time average which equal zero on average.  $\rho$  is the density of air,  $c_p$  is the specific heat capacity of air at constant pressure,  $L$  is the latent heat of vaporisation or sublimation, dependent on the surface temperature  $T_s$ ,  $w$  is the vertical wind velocity,  $\theta$  is the potential temperature and  $q$  is the specific humidity. Potential temperature is defined as  $\theta = T \left(\frac{p_R}{p}\right)^{-\frac{R_d}{c_p}}$ , where  $T$  is air temperature,  $p$  is pressure,  $p_R = 1000$  hPa is a reference pressure and  $R_d \approx 287$  J kg<sup>-1</sup> K<sup>-1</sup> is the gas constant of dry air.

$Q_G$  is the subsurface conductive heat flux, the result of heat conduction in the snow/ice layers. To calculate  $Q_G$ , we solve the heat-diffusion equation:

$$\rho c_p \frac{\partial T}{\partial t} = \frac{\partial}{\partial z} \left( k_{\text{eff}} \frac{\partial T}{\partial z} + \text{SW}_{\text{pen}} \right) + q_{\text{ref}}, \quad (2.4)$$

where  $q_{\text{ref}}$  is the heat generated by refreezing,  $\text{SW}_{\text{pen}}$  is the amount of short-wave radiation that penetrates the surface, and  $k_{\text{eff}}$  is the effective conductivity of the snowpack. A subsurface temperature profile is calculated by solving Eq. (2.4), and the ground-heat flux is then given by

$$Q_G = k_{\text{eff}} \frac{\partial T}{\partial z} \Big|_{z=0}. \quad (2.5)$$

In summer and during daytime, the surface is typically warmer than the subsurface, causing a negative  $Q_G$ ; in winter and during the night, the surface is typically colder than the subsurface, leading to a positive  $Q_G$ .

$Q_R$  is the energy provided to the surface by liquid precipitation. As the air temperature in Antarctica is almost always below 0°C, there is very little

liquid precipitation and therefore, this term is neglected. Finally,  $M$  is the amount of energy available for surface melt, constrained by

$$M = \begin{cases} 0 & \text{if } T_s < 273.15 \text{ K} \\ > 0 & \text{if } T_s = 273.15 \text{ K}, \end{cases} \quad (2.6)$$

with  $T_s$  the surface temperature. As the surface is a snow or ice surface,  $T_s$  cannot exceed 273.15 K, the melting point of ice.

## 2.2 Modelling the SEB

Only the radiation terms  $SW_{\text{net}}$  and  $LW_{\text{net}}$  of Eq. (2.1) can be measured directly. Therefore, the first step is to express the other terms as a function of surface temperature  $T_s$ . After rewriting, an iterative procedure is used to find the value of  $T_s$  for which the SEB equation (Eq. 2.1) is closed within an accuracy of 0.01 K. If this value were to exceed 273.15 K,  $T_s$  is set to this value and excess energy is available for surface melt ( $M$ ).

### 2.2.1 Radiation fluxes

Although it is possible to use measured  $LW\uparrow$ , it is preferable to use this observation to evaluate the SEB model. Therefore, we assume the surface to radiate as a black body and use the Stefan-Boltzmann relation to calculate  $LW\uparrow$  as:

$$LW\uparrow = -\epsilon\sigma T_s^4, \quad (2.7)$$

where  $\sigma = 5.67 \cdot 10^{-8} \text{ W m}^{-2} \text{ K}^{-4}$  is the Stefan-Boltzmann constant and  $\epsilon$  is the long-wave emissivity of the surface. Comparing modelled to measured  $LW\uparrow$  provides a direct way to evaluate the performance of the model when  $T_s < 0^\circ\text{C}$  (Van den Broeke et al., 2005a). As the long-wave radiation sensor is elevated above the surface, the measured  $LW\uparrow$  is not exclusively emitted by the surface but also partly by the air between the surface and the sensor. Equation (2.7) nonetheless provides a sufficiently accurate way to calculate  $T_s$  from measured  $LW\uparrow$  (see e.g. Fig. 3.4). We set  $\epsilon = 1$  in this thesis, which is a reasonable approximation: observations of

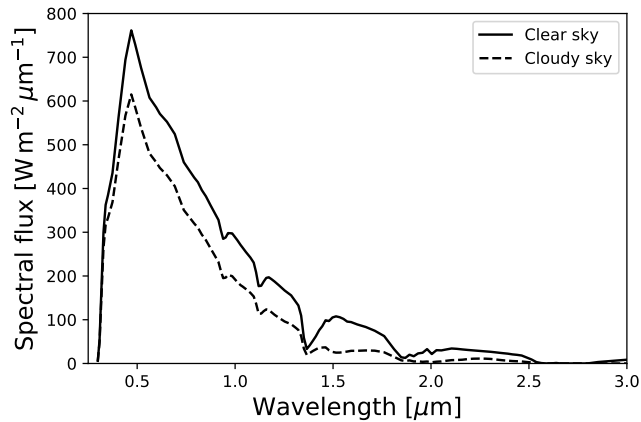


**Figure 2.2** Solar spectrum at the surface of the Antarctic Plateau for clear-sky and cloudy circumstances (Brandt and Warren, 1993).

snow/ice surface emissivity yield values between 0.95–1 (Wiscombe and Warren, 1980; Hori et al., 2006; Keck et al., 2017).

Similarly, it is possible to directly use measured net short-wave radiation. However, short-wave radiation sensors are susceptible to rime formation and tilting of the observation mast (Van den Broeke et al., 2004c). This mainly affects the upward-facing sensor. To minimise this effect, we use an adapted value of  $SW\downarrow$ . For each timestep, we first calculate a 24-hour running mean albedo. We then use this value to recalculate  $SW\downarrow$  from measured  $SW\uparrow$ .

Optionally, the model also simulates the penetration of short-wave radiation into the surface. This is modelled following Brandt and Warren (1993), in which the flux of radiation at depth  $z + \Delta z$  is related to the flux at depth  $z$  as:

$$F\downarrow(z + \Delta z) = F\downarrow(z) \exp(k_\lambda \Delta z), \quad (2.8)$$

where  $k_\lambda$  is the wavelength-dependent extinction coefficient. The model makes use of 118 spectral bands. For each band, the amount of short-wave radiation is determined from observed  $SW\downarrow$  and the solar spectrum (Fig. 2.2). The associated extinction coefficients are calculated from a look-up table, compiled using Mie scattering theory (Warren, 1984), depending on layer density  $\rho$  and effective snow grain size  $r_e$ .

## 2.2.2 Turbulent fluxes

Eddy covariances can be measured directly by sonic anemometers and Lyman- $\alpha$  sensors, but these are costly and difficult to operate for longer periods in harsh conditions as encountered on the Antarctic ice sheet, mainly because of their high energy consumption (Bintanja, 2000; Van As et al., 2005). To circumvent this, we determine the turbulent fluxes by using the *bulk method* (Denby and Greuell, 2000), which is based on Monin-Obukhov similarity theory (Monin and Obukhov, 1954). This method hypothesises that turbulent fluxes can be expressed in terms of *turbulent scales* of velocity ( $u_*$ ), potential temperature ( $\theta_*$ ) and humidity ( $q_*$ ):

$$Q_S = -\rho c_p u_* \theta_* \quad (2.9)$$

$$Q_L = -\rho L u_* q_* \quad (2.10)$$

The turbulent scales are related to the gradients of horizontal wind speed  $u$ ,  $\theta$  and  $q$  according to the *flux-profile relations* (Denby and Greuell, 2000):

$$\frac{\kappa z}{u_*} \frac{\partial u}{\partial z} = \phi_m(\zeta) \quad (2.11)$$

$$\frac{\kappa z}{\theta_*} \frac{\partial \theta}{\partial z} = \phi_h(\zeta) \quad (2.12)$$

$$\frac{\kappa z}{q_*} \frac{\partial q}{\partial z} = \phi_q(\zeta), \quad (2.13)$$

where  $z$  is the measurement height above the surface,  $\kappa$  is the Von Kármán constant ( $\kappa = 0.4$ ) and  $\zeta = \frac{z}{L_{MO}}$  is a dimensionless height based on the Monin-Obukhov length:

$$L_{mo} = \frac{u_*^2}{\frac{\kappa g}{T} \left( \theta_* + T \frac{1-\epsilon}{\epsilon} q_* \right)}, \quad (2.14)$$

where  $T$  is air temperature,  $g$  is the acceleration of gravity and here  $\epsilon$  is the ratio of the gas constant of dry air over the gas constant of moisture ( $\epsilon \approx 0.622$ ). The functions  $\phi_m$ ,  $\phi_h$  and  $\phi_q$  are stability functions for momentum, heat and moisture, respectively. Integration of Eqs. (2.11)–(2.13) between

two measurement levels  $z_1$  and  $z_2$  yields:

$$\frac{\kappa(u(z_2) - u(z_1))}{u_*} = \ln \frac{z_2}{z_1} - \psi_m(\zeta_2) + \psi_m(\zeta_1) \quad (2.15)$$

$$\frac{\kappa(\theta(z_2) - \theta(z_1))}{\theta_*} = \ln \frac{z_2}{z_1} - \psi_h(\zeta_2) + \psi_h(\zeta_1) \quad (2.16)$$

$$\frac{\kappa(q(z_2) - q(z_1))}{q_*} = \ln \frac{z_2}{z_1} - \psi_q(\zeta_2) + \psi_q(\zeta_1), \quad (2.17)$$

where  $\psi \equiv \int_0^\zeta (1 - \phi(\zeta')) d \ln(\zeta')$ . The turbulent fluxes obtained with this method compare well to direct observations of the eddy fluxes (Van den Broeke et al., 2005b; Van Tiggelen et al., 2020).

For unstable conditions ( $\zeta < 0$ ), the vertically integrated stability functions of Dyer (1974) are used:

$$\psi_m = 2 \ln \left( \frac{1+x}{2} \right) + \ln \left( \frac{1+x^2}{2} \right) - 2 \arctan x + \frac{\pi}{2} \quad (2.18)$$

$$\psi_h = \psi_q = 2 \ln \left( \frac{1+x^2}{2} \right), \quad (2.19)$$

with  $x = (1 - 16\zeta)^{1/4}$ . For stable conditions ( $\zeta > 0$ ), the vertically integrated stability functions of Holtslag and De Bruin (1988) are used:

$$\psi_m = - \left[ (0.7\zeta) + 0.75 \left( \zeta - \frac{5}{0.35} \right) \exp(-0.35\zeta) + 0.75 \frac{5}{0.35} \right] \quad (2.20)$$

and  $\psi_h = \psi_q = \psi_m$ .

We take the surface as the lowest of the two measurement levels in Eqs. (2.15)–(2.17). The lower level is equal to the *roughness lengths*  $z_{0,i}$ : the heights at which the wind ( $z_{0,m}$ ), humidity ( $z_{0,q}$ ) and temperature ( $z_{0,h}$ ) are assumed to obtain their respective surface values. This gives the following boundary conditions:  $u(z_{0,m}) = 0$ ,  $\theta(z_{0,h}) = T_s + \frac{g z_{0,h}}{c_p}$  and  $q(z_{0,q}, T) = q_{\text{sat}}(T_s)$ .

The roughness length for momentum  $z_{0,m}$  can be calculated from wind speed measurements at two heights using Eq. (2.15), but it can also be

**Table 2.1** Coefficients for Eq. (2.21), taken from Andreas (1987).

	$Re_* \leq 0.135$	$0.135 < Re_* < 2.5$	$2.5 \leq Re_* \leq 1000$
Heat			
$b_{0,h}$	1.25	0.149	0.317
$b_{1,h}$	–	-0.55	-0.565
$b_{2,h}$	–	–	-0.183
Moisture			
$b_{0,q}$	1.61	0.351	0.396
$b_{1,q}$	–	-0.628	-0.512
$b_{2,q}$	–	–	-0.18

used as a free tuning parameter in the SEB model. In this thesis, we prescribe  $z_{0,m}$  and use it to derive the other roughness lengths following the expressions by Andreas (1987):

$$\ln \left( \frac{z_{0,i}}{z_{0,m}} \right) = b_{0,i} + b_{1,i} \ln Re_* + b_{2,i} (\ln Re_*)^2, \quad (2.21)$$

where  $z_{0,i}$  is either  $z_{0,h}$  or  $z_{0,q}$ , the coefficients  $b_{j,i}$  are presented in Table 2.1 and  $Re_* = \frac{u_* z_{0,m}}{\nu}$  is the roughness Reynolds number, in which  $\nu$  is the kinematic viscosity of air.

This approach enables us to calculate the turbulent fluxes from the single-level AWS observations of temperature, wind speed and humidity.

### 2.2.3 Ground-heat flux

To determine the ground-heat flux, we first have to calculate the subsurface temperature profile from Eq. (2.4). To achieve this, a multilayer snow model is coupled to the SEB model, which consists of snow and ice layers, each with thickness  $dz$ , temperature  $T$ , density  $\rho$ , grain size  $r_e$  and liquid water content  $f_{liq}$  (see Fig. 2.1). The model incorporates densification of snow and firn, percolation and refreezing of meltwater, and penetration of short-wave radiation. The model is initialised with 70 layers, with layer thickness ranging from 1 cm at the top to 2 m at the bottom, in this case at

25 m below the surface. The bottom layer is kept at a constant prescribed temperature.

Snow densification is parameterised according to a semi-empirically derived equation following Arthern et al. (2010), which is in turn based on Herron and Langway (1980):

$$\frac{\partial \rho}{\partial t} = Cbg(\rho_i - \rho)e^{\left(\frac{-E_c}{RT_s} + \frac{E_g}{RT_s}\right)}, \quad (2.22)$$

with  $b$  the average annual accumulation,  $g$  the acceleration of gravity,  $\rho_i = 917 \text{ kg m}^{-3}$  the density of ice,  $E_c = 60 \text{ kJ mol}^{-1}$  and  $E_g = 42.4 \text{ kJ mol}^{-1}$  are constant activation energies,  $R = 8.314 \text{ J mol}^{-1} \text{ K}^{-1}$  is the ideal gas constant,  $T_s$  is the surface temperature,  $\overline{T_s}$  is the annual average surface temperature, and

$$C = \begin{cases} 0.07 & \text{for } \rho \leq 550 \text{ kg m}^{-3} \\ 0.03 & \text{for } \rho > 550 \text{ kg m}^{-3}. \end{cases} \quad (2.23)$$

When rain or meltwater enters the snowpack, it can either refreeze or percolate downwards. Refreezing is only possible when the layer temperature is below the melting point of ice, and when sufficient pore space is available, i.e. when the layer density has not yet reached  $\rho_i$ . If no refreezing can occur, the meltwater will remain in the layer if the layer has not yet reached its maximum capillary water retention. This *irreducible water content* is calculated as (Coléou and Lesaffre, 1998; Schneider and Jansson, 2004):

$$\theta_{mi} = 0.0143e^{3.3022n} \quad (2.24)$$

$$n = \frac{\rho_i - \rho}{\rho_i},$$

where  $n$  is the porosity, i.e. the available pore space in the firn. If there is more water available in the layer than what can be stored, the surplus of water percolates downwards to the next layer, where the procedure is repeated. This is called the tipping-bucket method (see e.g. Ligtenberg et al., 2011). If water cannot refreeze anywhere, for example because the

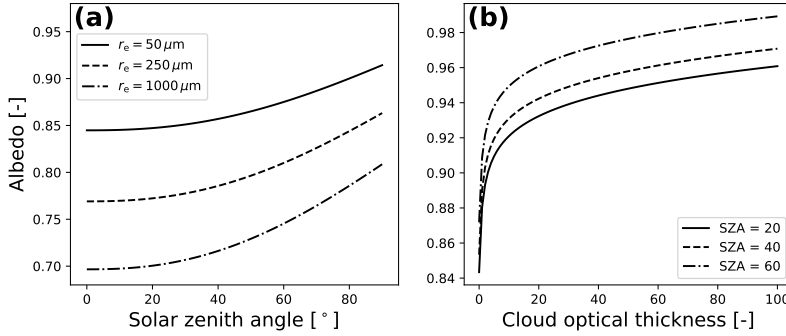


**Figure 2.3** Dependence of surface albedo of pure, dry snow on different grain sizes, solar zenith angle **(a)** and cloud optical thickness **(b)**, according to Eqs. (2.26)–(2.29).

entire column is at the melting point, the residual meltwater runs off. In reality, this meltwater can form melt ponds or meltwater streams on the ice surface, transporting mass away from the glacier or ice sheet. In the model, however, runoff is assumed to take place immediately, and the mass is removed instantaneously from the snowpack.

## 2.2.4 Albedo parameterisation

In order to explicitly quantify the snowmelt–albedo feedback, we use the albedo parameterisation by Kuipers Munneke et al. (2011b), which is based on Gardner and Sharp (2010). In this parameterisation, the surface albedo  $\alpha$  depends on snow grain size  $r_e$ , the solar zenith angle  $\theta$ , cloud optical thickness  $\tau$  and impurity concentration in the snow  $c$ :

$$\alpha = \alpha_S + d\alpha_u + d\alpha_\tau + d\alpha_c, \quad (2.25)$$

where  $\alpha_S$  is the base albedo calculated from  $r_e$ , and  $d\alpha_u$ ,  $d\alpha_\tau$  and  $d\alpha_c$  are the modifications due to the solar zenith angle  $\theta$  ( $u = \cos \theta$ ), cloud optical thickness and the snow impurities, respectively. The terms in Eq. (2.25)

are calculated as

$$\alpha_S = 1.48 - 1.27048r_e^{0.07} \quad (2.26)$$

$$d\alpha_u = 0.53\alpha_S(1 - \alpha_c)(1 - 0.64x - (1 - x)u)^{1.2} \quad (2.27)$$

$$d\alpha_c = \max\left(0.04 - \alpha_S, \frac{-c^{0.55}}{0.16 + 0.1085r_e^{-0.5} + 4.232c^{0.6}r_e^{0.25}}\right) \quad (2.28)$$

$$d\alpha_\tau = \frac{0.1\tau\alpha_c^{1.3}}{(1 + 1.5\tau)^{\alpha_S}}, \quad (2.29)$$

where  $x = \min(\sqrt{\tau/3u}, 1)$  and  $\alpha_c = \alpha_S + d\alpha_c$ . Figure 2.3 shows the dependence of surface albedo on  $r_e$ ,  $\tau$  and  $u$ . In Antarctica, it is customary to set  $c = 0$  as the snow impurity concentration is very low (Warren and Clarke, 1990; Grenfell et al., 1994; Bisiaux et al., 2012).

The snow grain size is given by

$$r_e(t) = [r_e(t-1) + dr_{e,dry} + dr_{e,wet}]f_o + r_{e,0}f_n + r_{e,r}f_r, \quad (2.30)$$

where  $dr_{e,dry}$  and  $dr_{e,wet}$  describe the grain metamorphisms for dry and wet snow,  $r_{e,0}$  and  $r_{e,r}$  are the grain sizes of new and refrozen snow, and  $f_o$ ,  $f_n$  and  $f_r$  are the fractions of old, new and refrozen snow respectively. Wet snow metamorphism is parameterised according to Brun et al. (1989):

$$\frac{dr_{e,wet}}{dt} = \frac{Cf_{liq}^3}{4\pi r_e^2}, \quad (2.31)$$

where  $C = 4.22 \cdot 10^{-13} \text{ m}^3 \text{ s}^{-1}$  and  $f_{liq}$  is the liquid water content. Dry snow metamorphism is given by (Kuipers Munneke et al., 2011b):

$$\frac{dr_{e,dry}}{dt} = \left(\frac{dr_{e,dry}}{dt}\right)_0 \left(\frac{\eta}{(r_e - r_{e,0}) + \eta}\right)^{1/\kappa}, \quad (2.32)$$

where  $\left(\frac{dr_{e,dry}}{dt}\right)_0$ ,  $\eta$  and  $\kappa$  are obtained from a look-up table (Flanner and Zender, 2006).

In Chapter 3 we use the method of Kuipers Munneke et al. (2011b), which takes multiple layers into account. In this method, the contribution of  $n$  snow layers is considered by calculating specific albedos  $\alpha_i$  for all snow layers separately, and combining these to a total albedo  $\alpha$  as:

$$\alpha = \alpha_1 + \sum_{i=2}^n (\alpha_i - \alpha_{i-1}) \exp\left(-\sum_{j=1}^{i-1} \Delta z_j / z_*\right). \quad (2.33)$$

This method assumes the contribution of layer  $i$  decays exponentially with depth (Oerlemans and Knap, 1998).  $z_*$  is a depth scale that determines the influence of lower layers on the total albedo. Following Kuipers Munneke et al. (2011b), we take  $z_* = 1$  cm and we take the upper 10 cm of snow into account.

In Chapter 5 we use the regional climate model RACMO2, which uses the implementation of Gardner and Sharp (2010). Although this method does not consider a multilayer snow albedo, there is a modification to  $d\alpha_c$  (Eq. 2.28) to account for two layers:

$$d\alpha'_c = (\alpha_c^{\text{btm}} - \alpha_s^{\text{top}}) + A (\alpha_c^{\text{top}} - \alpha_c^{\text{btm}}), \quad (2.34)$$

where  $\alpha^{\text{top}}$  and  $\alpha^{\text{btm}}$  denote the albedos of the first and second layer, respectively, and  $A = \min\left[1, 2.1z^{1.35(1-\alpha_s^{\text{top}})-0.1c-0.13}\right]$ , in which  $z$  is the top layer thickness. However, for a layer thickness  $z < \frac{1}{2.1}$  m, this factor is always equal to 1, i.e.  $d\alpha'_c = d\alpha_c$  and so the second layer is not taken into account.

## 2.3 Automatic weather stations

In order to use the SEB model described above, we need observations of several near-surface variables. In 2019, 57 automatic weather stations were operational on the Antarctic ice sheet (Fig. 2.5), but only a very limited number of them measure all the required quantities. Most of the Antarctic weather stations do not measure the full radiation balance, i.e. incoming and outgoing short-wave and long-wave radiation fluxes.

The Institute for Marine and Atmospheric Research Utrecht (IMAU) has operated a total of 35 Automatic Weather Stations (AWS) in several glaciated regions: Greenland, Svalbard, Iceland, Norway, the Alps and Antarctica. Not all of these stations were operational simultaneously. The first station was deployed in 1994 on the Morteratsch glacier in Switzerland (Fig. 2.4a) and this station is still operational. In the same season, the first station was deployed in Greenland, while the first station in Antarctica started operations one year later. As of 2020, 12 AWS are still operational, most of which are located in Greenland. The station on the Morteratsch glacier now covers the longest time series of all IMAU-AWS (Reijmer, 2020, personal communication).

The first IMAU-AWS type (T1) measured temperature, wind speed, short-wave radiation and instrument height (sensor information is provided in Table 4.1). However, in order to fully model the SEB, it is also necessary to measure relative humidity and long-wave radiation. Therefore, a new type was introduced (T2) which included humidity and long-wave radiation sensors (Van den Broeke et al., 2004c). A final upgrade to type T3 consisted of adding solar cells as an energy source, in addition to the lithium batteries that are also used in the T1 and T2 stations.

In the cold, harsh climate of Antarctica, several difficulties arise for carrying out such automatic meteorological observations. To save energy, IMAU has chosen not to artificially ventilate the instruments. This mostly affects the air temperature and humidity measurements, as these sensors are susceptible to heating by solar radiation. Active ventilation maintains a constant airflow around the sensor, which limits this effect. Van den Broeke et al. (2005a) show that this can lead to errors in the temperature measurements of up to 10 K for the T1 stations. T2 and T3 stations use improved shielding, and therefore typically have errors  $<1$  K. At very low temperatures ( $<-20^{\circ}\text{C}$ ), the maximum relative humidity that can be measured by the humidity sensor decreases strongly; we use the method of Anderson (1994) to correct this. The low temperatures in Antarctica can furthermore cause rime formation on the sensors (Fig. 2.4b), which can affect the sonic height ranger and radiation sensors (Van den Broeke et al., 2004c). Furthermore, the wind speed and wind direction sensors can freeze up in riming conditions.



**Figure 2.4** Left image: AWS on the Morteratsch glacier, Switzerland, June 2016, photo by Stan Jakobs. Right image: rime formation on AWS 9, Antarctic ice sheet, photo by Wim Boot (IMAU).

In the ablation zone, the sinking surface does not allow for fixing the AWS to the ice surface. Therefore, the AWS consists of a central mast with one or more crossbars, to which the instruments are attached. From the central mast, four legs spread outwards; on an ice surface, these legs melt into the ice surface, locking them in place. During the melt season in an ablation zone, the AWS moves down as the ice surface melts, remaining largely in the same place and upright. The AWS can become tilted when the surface melts inhomogeneously, which mainly affects reflected short-wave radiation measurements (Wang et al., 2016). As described in Sect. 2.3, this problem is mitigated by recalculating  $SW_{\downarrow}$  from measured  $SW_{\uparrow}$ , using the 24-hour running mean albedo (Van den Broeke et al., 2004c).

Measurements are taken every 5 (T1) or 6 min (T2/T3), which are averaged over two-hourly (T1 and early T2), one-hourly (T2) or half-hourly (T3) intervals. These averages are stored locally and also transmitted over the Argos satellite system; the live data of the operational AWS can be found on the IMAU website<sup>1</sup>. Approximately once every year an AWS is visited, dug out if necessary, sensors swapped and the memory card replaced.

In-situ measurements are the first and foremost method to obtain information about local weather phenomena. Although the AWSs have a rela-

---

<sup>1</sup>For example, data from Antarctic weather stations on <https://www.projects.science.uu.nl/iceclimate/aws/antarctica.php>.





**Figure 2.6** Neumayer Station on the Ekström ice shelf. Photo by Felix Riess, licensed under CC BY-SA 3.0 de.

up of the wind speed sensor can temporarily cause unreliable or missing data. Furthermore, because of the rare visits, it is not always clear there is something wrong with the AWS. These issues can be mitigated by using weather stations that transmit the data or are visited regularly, which can therefore provide higher quality datasets.

Neumayer Station is a year-round staffed scientific base on the Ekström ice shelf in Dronning Maud Land, East Antarctica (Fig. 2.6). A meteorological observatory is located close to the base and is visited daily, resulting in high-quality meteorological and radiation measurements. These data are used in Chapter 3 in a case-study to determine the surface energy balance and snowmelt–albedo feedback at one location in Antarctica.

The weather station at Neumayer is part of the Baseline Surface Radiation Network (BSRN), a global network of artificially ventilated, high-quality radiation observations, coordinated by the Alfred Wegener Institute (AWI) in Bremerhaven, Germany. Its goal is to provide a uniform and consistent dataset of Earth surface radiation measurements, with high

precision ( $<5 \text{ W m}^{-2}$ ). The BSRN network currently consists of 64 stations, covering  $80^\circ\text{N}$  to  $90^\circ\text{S}$ . Neumayer Station provides the longest available time series of the BSRN in Antarctica.

## 2.4 Regional climate models

A disadvantage of weather stations is the fact that the data they provide are limited in time and space: only in a handful of locations, stations have been erected and data are available, but always for just a limited period of time (see Fig. 2.5). In order to understand and study the climate of the entire Antarctic ice sheet for longer time periods, we can use climate models for a physics-based interpolation of AWS data in time and space.

Climate models are operated either on a regional or on a global scale, and can incorporate different components of the climate system. An atmospheric model only considers the atmosphere, and uses prescribed boundary conditions for e.g. sea-surface temperatures. In a coupled atmosphere-ocean model, a separate model simulates ocean processes, and feedbacks between the atmosphere and ocean are explicitly taken into account. Even more complex models consider feedbacks between all climate components, in so-called Earth system models.

A global model has the advantage that it does not need lateral boundary conditions: the modelled components are allowed to evolve freely. However, because of this large horizontal scale, global models are usually run at relatively coarse resolutions, and many processes are parameterised rather than solved explicitly.

On the other hand, a regional climate model covers only a part of the globe, which allows it to be run at higher resolution. As a result, it can use fewer parameterisations or more sophisticated parameterisations. The drawback is that it requires lateral and often also upper/lower boundary conditions, which constrain the interior solutions. These boundary conditions are usually taken from global models.

### 2.4.1 RACMO2

Throughout this thesis, we use the regional climate model RACMO2 to simulate the climate of Antarctica and surface processes on the Antarctic ice sheet. RACMO2 has been developed by the Royal Netherlands Meteorological Institute (KNMI) (Lenderink et al., 2003). This section provides an overview of the development of RACMO2 over the past several years, with emphasis on the polar version used throughout this thesis.

RACMO2 combines the dynamical part of a numerical weather prediction model, HIRLAM (Undén et al., 2002), with the physics parameterisations of a global model, IFS (ECMWF, 2009). The dynamical part solves the conservation equations of momentum, heat and moisture in the atmosphere on the prescribed model grid. RACMO2 is a hydrostatic model, which means that vertical accelerations are neglected. This is a reasonable assumption when using a relatively coarse model grid ( $>5$  km), as the highest vertical accelerations are encountered in convective clouds, which are usually smaller than that. In the era of constantly increasing computational power and thus model resolution, at resolutions higher than 5 km this hydrostatic approximation is no longer valid and one has to resort to a computationally more expensive non-hydrostatic model (Van de Berg et al., 2020).

The physics part of the model simulates processes that act on scales smaller than the horizontal and vertical model resolutions. As these cannot be calculated explicitly, parameterisations are used for e.g. cloud formation, precipitation and boundary-layer turbulence. This part of RACMO2 has received regular updates over the years, following updates of the physics parameterisations of IFS. The upgrade from RACMO2.0 to RACMO2.1 mainly involved changes in the cloud schemes and near-surface wind and temperature calculations (Van Meijgaard et al., 2008); this version also included an update of the dynamical core. From RACMO2.1 to RACMO2.3, major modifications were implemented concerning deep convection and the improved representation of turbulent mixing in the boundary layer (Van Meijgaard et al., 2012). These consecutive updates have gradually improved the performance of RACMO2 in simulating the climate of the Antarctic and Greenland ice sheets (Van Wessem et al., 2014a; Noël et al., 2015, 2018b; Van Wessem et al., 2018).

Apart from these general modifications, which are also implemented in the model used by the KNMI, IMAU has developed a polar version of RACMO2. Reijmer et al. (2005) replaced the single-layer snow model with multiple snow layers coupled to the existing soil layers, and used a new parameterisation for the roughness length that was more suitable for use over glaciated areas. Furthermore, they improved the albedo parameterisation by including temperature dependency in the albedo calculation. Ettema et al. (2009) further improved the snow model by detaching it from the soil layers, and introducing ice layers with multiple snow and firn layers on top. This allowed for a more detailed treatment of subsurface snow processes such as densification and meltwater percolation. Kuipers Munneke et al. (2011b) introduced a new albedo parameterisation, in which the surface albedo is related to the snow grain size. The snow grain size is calculated as a function of water content, snowfall rate, snowmelt rate, and temperature and density profiles of the snowpack. A final addition to the polar version was made by Lenaerts et al. (2012), who included a drifting-snow scheme that calculates the amount of snow that is transported and sublimated by wind. This affects accumulation and ablation patterns across the ice sheet.

Smaller adjustments have since been made to RACMO2.3, leading to the polar-specific version RACMO2.3p2 (Noël et al., 2018b; Van Wessem et al., 2018). The main change concerned delaying the onset of precipitation, allowing moisture to be advected farther onto the ice sheet interior. This resolved a bias present in RACMO2.3p1 and earlier, in which too much precipitation was deposited on the ice sheet margins. Further model adjustments concerned recalibration of the drifting snow scheme and using the albedo scheme (Kuipers Munneke et al., 2011b) for superimposed ice instead of using the bare ice albedo. This model version is used throughout this thesis and is usually referred to as RACMO2.

The development of RACMO2 is still ongoing. Van Dalum et al. (2019) introduced a spectral albedo scheme, replacing the parameterisation by Kuipers Munneke et al. (2011b). Van Dalum et al. (2020) show that the updated albedo scheme yields a better representation of the Greenland ice sheet albedo. Furthermore, a new physics parameterisation upgrade is underway, incorporating the parameterisations from a more recent version of the IFS (Van Wessem, personal communication, 2020).

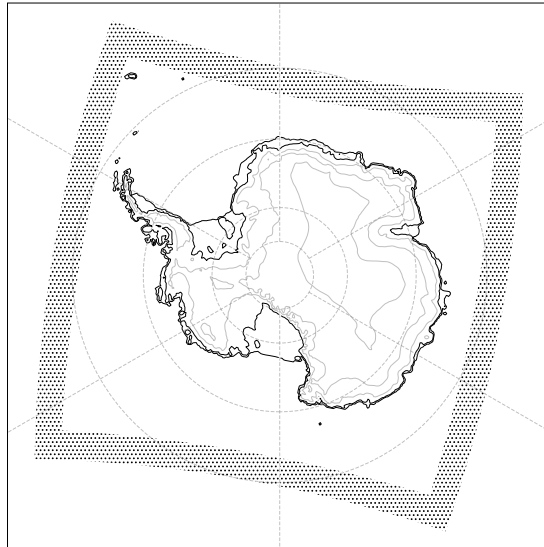


**Figure 2.7** Model domain of RACMO2 covering the AIS at 27 km resolution. The border indicates the relaxation zone, where boundary conditions are applied.

In this thesis, RACMO2 is run on the Antarctic domain shown in Fig. 2.7, at 27 km resolution grid and using 40 vertical atmospheric layers, for the time period 1979–2018. It is forced at its lateral boundaries by the ERA-interim reanalysis product of the ECMWF (Dee et al., 2011). This reanalysis is the result of assimilating all available observations to obtain the global state of the atmosphere, using a weather model to dynamically interpolate between the observations. Furthermore, RACMO2 uses upper-air relaxation (Van de Berg and Medley, 2016). As RACMO2 does not simulate ocean processes, sea surface temperature and sea ice cover are prescribed from the reanalysis product. A comprehensive evaluation of RACMO2 in Antarctica can be found in Van Wessem et al. (2018). Apart from Antarctica, RACMO2 is also used to simulate the climate of Greenland, the Canadian Arctic, Svalbard and the Patagonian ice fields (Lenaerts et al., 2014; Noël et al., 2018a,b, 2020a).

## 3. SMAF at Neumayer

We use 24 years (1992–2016) of high-quality meteorological observations at Neumayer Station, East Antarctica, to force a surface energy balance model. The modelled 24-year cumulative surface melt at Neumayer totals 1154 mm water equivalent (w.e.), with only a small uncertainty ( $\pm 3$  mm w.e.) from random measurement errors. Results are more sensitive to the chosen value for the surface momentum roughness length and new snow density, yielding a range of 900–1220 mm w.e. Melt at Neumayer occurs only in the months November to February, with a summer average of 50 mm w.e. and large interannual variability ( $\sigma=42$  mm w.e.). This is a small value compared to an annual average (1992–2016) accumulation of  $415\pm 86$  mm w.e. Absorbed shortwave radiation is the dominant driver of temporal melt variability at Neumayer. To assess the importance of the snowmelt–albedo feedback we include and calibrate an albedo parameterisation in the surface energy balance model. We show that, without the snowmelt–albedo feedback, surface melt at Neumayer would be approximately 3 times weaker, demonstrating how important it is to correctly represent this feedback in model simulations of surface melt in Antarctica.

### 3.1 Introduction

The Antarctic ice sheet (AIS) contains more than 25 million  $\text{km}^3$  of ice, sufficient to raise global mean sea level by almost 60 m if melted completely (Fretwell et al., 2013). Between 1992 and 2017, the AIS lost mass at an accelerated rate, contributing  $7.6 \pm 3.9$  mm to global sea level (Shepherd

---

This Chapter is published as “Quantifying the snowmelt–albedo feedback at Neumayer Station, East Antarctica”, *The Cryosphere*, **13**, 1473–1485, 2019, doi:10.5194/13-1473-2019.

et al., 2018). This mass loss is mainly observed in coastal West Antarctica and the Antarctic Peninsula (AP), and is caused by glaciers that accelerated after their buttressing ice shelves had thinned or disintegrated (Wouters et al., 2015; Turner et al., 2017).

The interaction between meltwater and firn, the intermediate product between snow and glacier ice, is hypothesised to play an important role in ice-shelf disintegration (Kuipers Munneke et al., 2014). If the firn layer contains enough air, as is the case for most of the AIS, meltwater can percolate downwards and refreeze (Ligtenberg et al., 2014). If the storage capacity of the firn layer is reduced, surface meltwater can flow laterally towards the ice-shelf edge (Bell et al., 2017), be stored englacially (Lenaerts et al., 2017) or form ponds on the ice-shelf surface (Kingslake et al., 2017). In all cases, meltwater can accumulate in crevasses, thereby increasing the hydrostatic pressure in the crevasse tip, causing it to penetrate farther down. When a crevasse reaches the bottom of the ice shelf or a basal crevasse, part of the ice shelf disintegrates, a process called hydrofracturing (Van der Veen, 2007).

Hydrofracturing has been identified as a potential precursor of rapid loss of Antarctic ice, accelerating sea level rise (DeConto and Pollard, 2016). In combination with enhanced ocean swell under low sea-ice conditions (Massom et al., 2018), hydrofracturing likely caused the disintegration of Larsen B ice shelf in the AP in 2002 (Rignot et al., 2004; Scambos et al., 2004). In July 2017, a large iceberg calved from Larsen C ice shelf, but it is unclear whether this signifies a further southward progression of ice-shelf destabilisation in the AP (Hogg and Gudmundsson, 2017).

Improving our predictive capabilities of future ice-shelf stability, AIS mass loss and associated sea level rise, thus requires a thorough understanding of the surface melt process on Antarctic ice shelves. In contrast to meltwater occurrence, which is readily observed from space (Picard et al., 2007; Tedesco, 2009; Luckman et al., 2014), observational estimates of surface melt *rates* on Antarctic ice shelves are rare; they have been obtained locally through explicit modelling of the surface energy balance (SEB) (Van den Broeke et al., 2010b; Kuipers Munneke et al., 2012b, 2018). In turn,

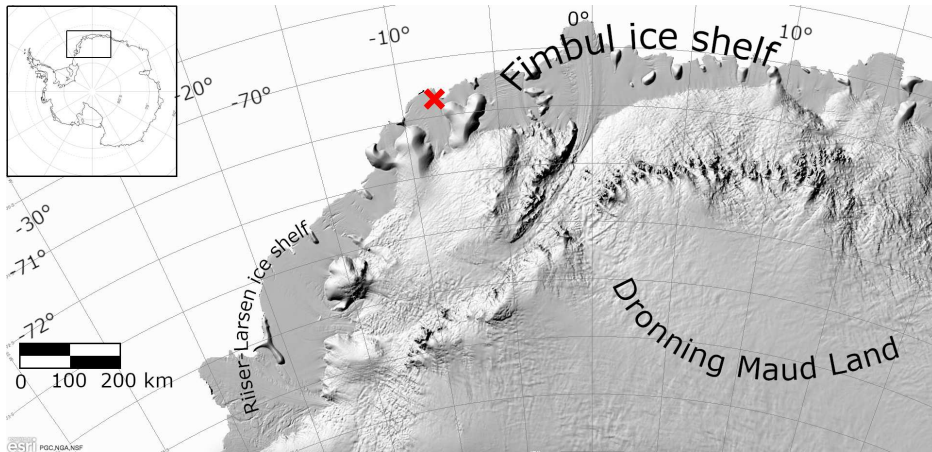


**Figure 3.1** Map of the Antarctic continent, the red cross indicates the location of Neumayer Station. Imagery ©2016 DigitalGlobe, Inc.

these enabled continent-wide melt rate estimates using calibrated satellite products based on backscatter strength of radio waves (Trusel et al., 2013, 2015).

These studies invariably demonstrate that in most parts of Antarctica, melt currently is a weak and intermittent process. In this melt regime, the positive snowmelt-albedo feedback plays a decisive role: when snow melts, meltwater may refreeze in the cold snowpack, resulting in considerably larger grains ( $\sim 1$  mm) than new snow or snow that has been subjected to only dry compaction ( $\sim 0.1$  mm). Larger snow grains reduce backward scattering of photons into the snowpack, increasing the probability of absorption, reducing the surface albedo especially in the near-infrared (Wiscombe and Warren, 1980; Gardner and Sharp, 2010). This further enhances absorption of solar radiation and melt. For pure, uncontaminated snow, the strength of the snowmelt-albedo feedback depends on multiple factors, e.g. the intensity and duration of the melt and the frequency and intensity of snowfall events, which provide new snow consisting of smaller grains. We therefore expect the snowmelt-albedo feedback to be spatially and temporally variable on Antarctic ice shelves.

Most studies on the snowmelt-albedo feedback address the removal of (seasonal) snow and the appearance of dark soil or water (Perovich et al.,

2002; Hall, 2004; Flanner et al., 2007; Qu and Hall, 2007), leading to further warming of the air/water. These studies commonly express the melt-albedo feedback in terms of air/water temperature sensitivity. Our aim is to quantify the impact on the melt rate of the darkening but not the disappearance of snow, a process addressed by far fewer studies (Box et al., 2012; Van As et al., 2013). To that end, we implement a snow albedo parameterization (Gardner and Sharp, 2010; Kuipers Munneke et al., 2011b) in an SEB model, which is then calibrated using observations and used to study the sensitivity of melt rates to snow properties that influence snow albedo. We use 24 years of high-quality in situ observations (König-Langlo, 2017) from the German research station Neumayer (Fig. 3.1) to calculate the SEB and melt rate. We investigate the effects of measurement uncertainties and model settings on the modelled cumulative amount of surface melt. We then analyse the main drivers of surface melt and the magnitude of the snowmelt-albedo feedback at Neumayer by switching on/off the feedback process in the albedo parameterisation.

The SEB model is explained in Sect. 3.2.1, followed by a description of the albedo parameterisation in Sect. 3.2.2. The meteorological data used to force the SEB model are described in Sect. 3.2.3. The results section is split into two parts; in Sect. 3.3 we present and discuss the SEB and melt rate that are obtained using the observed albedo. In Sect. 3.4 the albedo parameterisation is used instead and the snowmelt-albedo feedback is quantified and discussed. Finally, the results are discussed in Sect. 3.5.

## 3.2 Methods

### 3.2.1 Surface energy balance model

The one-dimensional energy balance model is a further development of the models presented by Reijmer et al. (1999), Reijmer and Oerlemans (2002), Van den Broeke et al. (2005a) and Kuipers Munneke et al. (2012b); here only the main features are described. The energy balance of an infinitesimally thin surface layer (the ‘skin’ layer) is defined as:

$$M = SW \downarrow + SW \uparrow + LW \downarrow + LW \uparrow + Q_S + Q_L + Q_G, \quad (3.1)$$

where positive fluxes are defined to be directed towards the surface.  $SW\downarrow$  and  $SW\uparrow$  are the incoming and reflected shortwave radiation,  $LW\downarrow$  and  $LW\uparrow$  are the downward and upward longwave radiation,  $Q_S$  and  $Q_L$  the turbulent sensible and latent heat fluxes and  $Q_G$  is the conductive subsurface heat flux. We neglect latent energy from rain.  $M$  is the energy used to melt snow or ice, and is non-zero only when the surface has reached the melting point of ice ( $T_s = 273.15$  K). Throughout this paper, melt and accumulation amounts are expressed in terms of mm water equivalent (mm w.e.), which equals  $\text{kg m}^{-2}$ .

In order to calculate  $Q_G$  and allow for densification, meltwater percolation and refreezing, a snow/firn model is used, initialised with 70 layers. The layer thickness varies from 1 cm at the top to 2 m at the bottom (25 m depth). We impose a no-energy flux boundary condition at the lowermost model level. New snow density is parameterised following the expression of Lenaerts et al. (2012), which relates it to the prevailing surface temperature ( $T_s$ ) and 10 m wind speed ( $V_{10\text{m}}$ ) and imposes a lower limit of new snow density  $\rho_{s,0}$ . Meltwater percolation is based on the tipping-bucket method (e.g. Ligtenberg et al., 2011), allowing for immediate downward transport (within a single time step of 10 s) of remaining water if a layer has attained its maximum capillary retention, as modelled using the expressions of Schneider and Jansson (2004). Meltwater refreezing increases the density and temperature of a layer. At the bottom of the firn layer, the meltwater is assumed to run off immediately, i.e. the model does not allow for slush/superimposed ice formation or lateral water movement. Turbulent fluxes are calculated following the ‘bulk’ method, which is based on Monin-Obukhov similarity theory (see e.g. Van den Broeke et al. (2006) for relevant equations) between a single measurement level (2 m for temperature and humidity, 10 m for wind) and the surface, assuming the latter to be saturated with respect to ice and using the stability functions according to Dyer (1974) for unstable and Holtslag and De Bruin (1988) for stable conditions.

Subsurface penetration of shortwave radiation is calculated using a spectral model (Kuipers Munneke et al., 2009), based on the parameterisation by Brandt and Warren (1993), which is in turn based on the two-stream radiation model of Schlatter (1972). The impact on modelled melt and the

quantification of the snowmelt-albedo feedback is discussed in the relevant sections.

The terms in Eq. (3.1) are either based on observations or can be expressed as a function of the skin temperature  $T_s$ . The SEB is solved iteratively by looking for a value of  $T_s$  that closes the SEB to within 0.005 K between iterations: if  $T_s > 273.15$  K, it is reset to 273.15 K and excess energy is used for surface melt  $M$ . To evaluate model performance, the modelled value of  $T_s$  is compared to observed  $T_s$  calculated from  $LW\uparrow$ , using Stefan-Boltzmann's law for a longwave emissivity  $\epsilon = 1$ :

$$LW\uparrow = \sigma T_s^4, \quad (3.2)$$

where  $\sigma = 5.67 \cdot 10^{-8} \text{ W m}^{-2} \text{ K}^{-4}$  is the Stefan-Boltzmann constant.

Surface roughness lengths for momentum, heat and moisture are related through the expression of Andreas (1987):

$$\ln\left(\frac{z_{0*}}{z_{0,m}}\right) = a_1 + a_2 \ln(\text{Re}_*) + a_3 \ln(\text{Re}_*)^2, \quad (3.3)$$

where  $z_{0*}$  represents either  $z_{0,h}$  or  $z_{0,q}$ , the roughness lengths for heat and moisture respectively,  $a_1$ ,  $a_2$  and  $a_3$  are coefficients determined by Andreas (1987) for various regimes of the roughness Reynolds number  $\text{Re}_* = \frac{u_* z_{0,m}}{\nu}$  with kinematic viscosity  $\nu$  and friction velocity  $u_*$ .

### 3.2.2 Albedo parameterisation

Because the shortwave radiation sensor faces the sky and includes a significant direct component, measured  $SW\downarrow$  suffers from relatively large uncertainties owing to poor sensor cosine response, sensor tilt and/or rime formation (Smeets et al., 2018). In order to improve the accuracy of observed net shortwave radiation used in the SEB calculations (Sect. 3.3), we calculate  $SW_{\text{net}}$  based on  $SW\uparrow$ , which is diffuse and hence much less sensitive to these errors. To further decrease the impact of these errors, we use a 24-hour moving average albedo, as described in Van den Broeke

et al. (2004b). In Sect. 3.4, in which albedo is parameterised to study melt-albedo feedbacks, for consistency we use measured  $\text{SW}\uparrow$  in combination with parameterised albedo to estimate  $\text{SW}_{\text{net}}$ .

In Sect. 3.4, the parameterised surface albedo  $\alpha$  is described as a base albedo  $\alpha_S$ , modified by perturbations describing the effect of changing solar zenith angle  $\theta$  ( $d\alpha_u$ ), the cloud optical thickness  $\tau$  ( $d\alpha_\tau$ ) and the concentration of black carbon in the snow ( $d\alpha_c$ ) (Gardner and Sharp, 2010; Kuipers Munneke et al., 2011b):

$$\alpha = \alpha_S + d\alpha_u + d\alpha_\tau + d\alpha_c. \quad (3.4)$$

For Antarctica, we neglect the impact of impurities in the snow ( $d\alpha_c = 0$ );  $d\alpha_u$  and  $d\alpha_\tau$  both depend on the base albedo  $\alpha_S$ ,  $d\alpha_u$  in addition depends on the solar zenith angle ( $u = \cos \theta$ ), and  $d\alpha_\tau$  on the cloud optical thickness  $\tau$ :

$$d\alpha_u = 0.53\alpha_S(1 - \alpha_S)(1 - 0.64x - (1 - x)u)^{1.2} \quad (3.5)$$

$$d\alpha_\tau = \frac{0.1\tau(\alpha_S + d\alpha_c)^{1.3}}{(1 + 1.5\tau)^{\alpha_S}}, \quad (3.6)$$

where  $x = \min\left(\frac{\sqrt{\tau}}{3u}, 1\right)$ .

The base albedo depends on the snow grain size  $r_e$  (in m):

$$\alpha_S = 1.48 - 1.27048r_e^{0.07}, \quad (3.7)$$

in which the snow grain size  $r_e$  on time step  $t$  is parameterised as

$$r_e(t) = [r_e(t-1) + dr_{e,\text{dry}} + dr_{e,\text{wet}}]f_o + r_{e,0}f_n + r_{e,r}f_r. \quad (3.8)$$

Here,  $dr_{e,\text{dry}}$  and  $dr_{e,\text{wet}}$  describe the metamorphism of dry and wet snow respectively,  $f_o$ ,  $f_n$  and  $f_r$  are the fractions of old, new and refrozen snow, and  $r_{e,0}$  and  $r_{e,r}$  are the grain sizes of new and refrozen snow.

Dry snow metamorphism is parameterised following Kuipers Munneke et al. (2011b)

$$\frac{dr_{e,\text{dry}}}{dt} = \left(\frac{dr_e}{dt}\right)_0 \left(\frac{\eta}{(r_e - r_{e,0}) + \eta}\right)^{1/\kappa}, \quad (3.9)$$

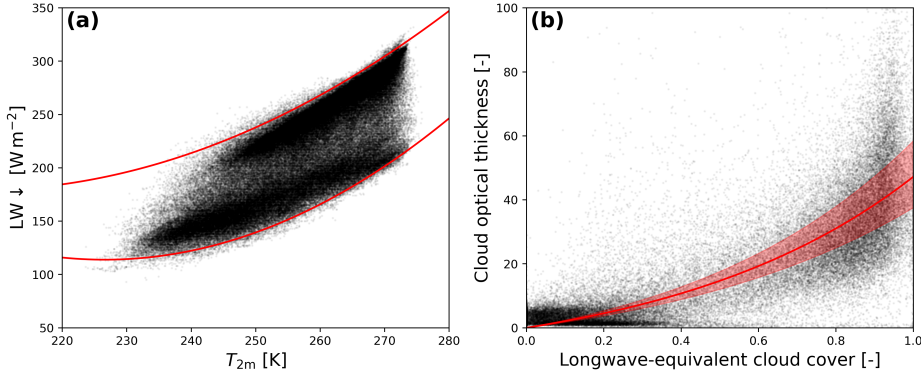


**Figure 3.2 (a)** Downward longwave radiation versus air temperature. The red lines are quadratic fits of the upper and lower 5 percentile boundaries. The longwave-equivalent cloud cover is determined by linear interpolation between these bounds. **(b)** Optical thickness versus cloud cover. The red line resembles the best fit to a function  $\tau = c_1 (e^{c_2 N_\epsilon} - 1)$ , the shaded area indicates the 95% uncertainty range.

where  $r_{e,0}$  is the new snow grain size, and the coefficients  $\left(\frac{dr_e}{dt}\right)_0$ ,  $\eta$  and  $\kappa$  are obtained from a look-up table. This look-up table is compiled based on simulations with the SNICAR model (Flanner and Zender, 2006), which calculates the snow metamorphism resulting from temperature gradient metamorphism.  $dr_{e,wet}$  is a function of the snow grain size  $r_e$  itself and the liquid water content  $f_{liq}$  (Brun et al., 1989):

$$\frac{dr_{e,wet}}{dt} = \frac{C f_{liq}^3}{4\pi r_e^2}, \quad (3.10)$$

where  $C$  is a constant ( $4.22 \cdot 10^{-13} \text{ m}^3 \text{ s}^{-1}$ ). The fractions  $f_o$ ,  $f_n$  and  $f_r$  are derived from the snow/firn model, and the grain sizes of new and refrozen snow are constants; the method for determining their values from a tuning exercise is described in Sect. 3.4.1.

To determine cloud optical thickness  $\tau$ , an empirical relation between  $\tau$  and the longwave-equivalent cloud cover  $N_\epsilon$  is used following Kuipers Munneke et al. (2011a):

$$\tau = c_1 (\exp(c_2 N_\epsilon) - 1), \quad (3.11)$$

with fitting parameters  $c_1$  and  $c_2$ .  $N_e$  is determined using a method described by Kuipers Munneke et al. (2011a) which relates hourly values of downward longwave radiation  $LW\downarrow$  to near-surface air temperature  $T_{2m}$  as illustrated in Fig. 3.2a. Red lines indicate quadratic fits through the upper and lower 5 percentile of the data, assuming to represent fully cloudy and clear conditions, respectively.  $N_e$  is obtained by linearly interpolating between these upper and lower bounds, yielding values between 0 and 1. Hourly values for cloud cover are then used to obtain values for  $\tau$  (Fig. 3.2b). The values used for the fit parameters  $c_1 = 5.404$  and  $c_2 = 2.207$  (both dimensionless) differ somewhat from Kuipers Munneke et al. (2011a), who used daily values for the fit.

### 3.2.3 Observational data

The SEB model is forced with data from the meteorological observatory at the German research station Neumayer, situated on the Ekström ice shelf (König-Langlo, 2017). The observatory has been operational since 1981, and was relocated in 1992 and 2009. In 2016, its location was  $70^\circ 40'S$ ,  $8^\circ 16'W$  (Fig. 3.1). The observatory is one of only four Antarctic stations –and the only one situated on an ice shelf– that is part of the Baseline Surface Radiation Network (BSRN), a global network of stations with high-quality (artificially ventilated) radiation observations, coordinated by the Alfred Wegener Institute (AWI).

We use hourly averages of 2 m temperature ( $T_{2m}$ ) and specific humidity ( $q_{2m}$ ), 10 m wind speed ( $V_{10m}$ ), surface pressure ( $p$ ) and radiation fluxes for the period April 1992–January 2016 (24 years) to force the SEB model; their uncertainty ranges are provided in Table 3.1. Approximately 4.1 % of the data points contained at least one missing variable, which mostly come from daily performed visual inspection of the data. To obtain a continuous data set, all missing data were replaced: pressure, relative humidity, wind speed, temperature and longwave radiation were simply linearly interpolated. In case of shortwave radiation, the missing value was replaced by imitating the average daily cycle of the two preceding days. As the measurement station is visited and maintained every day, the impact of rime formation is limited, as is the tilt of the observation mast, resulting in a high-quality meteorological data set.

**Table 3.1** Listing of used measurement variables and their associated measurement errors.

Variable	Neumayer errors
$V_{10\text{m}}$	max(0.5 m/s, 5%)
SW↓	5 W/m <sup>2</sup>
SW↑	5 W/m <sup>2</sup>
LW↓	5 W/m <sup>2</sup>
LW↑	5 W/m <sup>2</sup>
$T_{2\text{m}}$	0.1°C
RH <sub>2m</sub>	5%
$p$	0.5 hPa

Accumulation observations are only available from stake measurements, provided by AWI, which were performed weekly for the period April 1992–January 2009. As timing of precipitation is important for correctly simulating the effects of new snow on snow albedo, we combined the stake observations with precipitation predicted by the regional atmospheric climate model RACMO2.3p2 (Van Wessem et al., 2018) to obtain realistic timing of precipitation in between stake observations, as well as for the post-2009 period. The amount of precipitation modelled by RACMO2 was scaled such that the modelled surface height changes agree with stake measurements; this required a 15.3 % upward adjustment of the modelled precipitation flux.

### Local near-surface climate

Neumayer station is located on an ice shelf ~20 km from Halvfarryggen ice rise to the southeast, ~100 km from the ice-shelf break (grounding line) to the south, ~20 km from open water/sea ice to the north and ~5 km to open water/sea ice to the east. As a result, Neumayer experiences relatively mild conditions without significant impact from katabatic winds but with a pronounced influence of synoptic low-pressure systems passing mainly from west to east in the south Atlantic Ocean to the north of the station.

The seasonal cycles of 2 m temperature, 10 m wind and 2 m specific humidity are presented in Fig. 3.3a. Summer temperatures around -4°C and

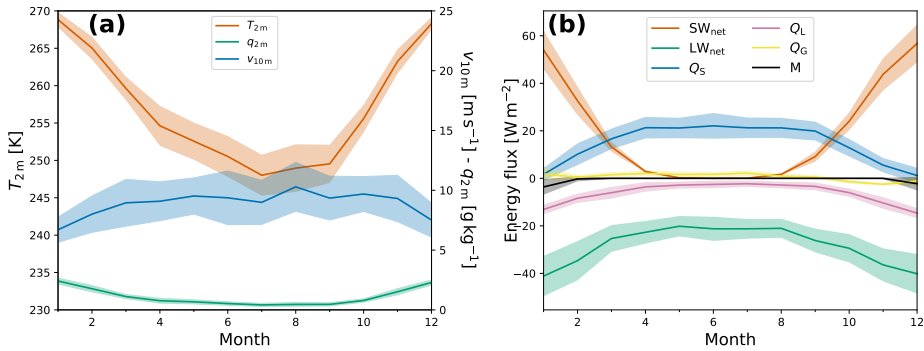


**Figure 3.3 (a)** Seasonal cycles of 2 m temperature (red, left axis), 10 m wind speed (blue, right axis) and 2 m specific humidity (green, right axis). Shaded areas indicate the standard deviations of monthly means. **(b)** Same as **(a)** for melt (black), net shortwave radiation (red), net longwave radiation (green), sensible heat (blue), latent heat (magenta) and ground heat (yellow).

winter temperatures around  $-25^{\circ}\text{C}$  imply a substantial ( $>20\text{ K}$ ) seasonal temperature amplitude based on monthly mean values. This is in line with the formation of a surface-based temperature inversion in winter, a phenomenon that is representative for the flat ice shelves as well as the interior ice domes and in contrast to the topographically steeper escarpment zone, where the quasi-continuous mixing by katabatic flow limits the formation of such an inversion (Van den Broeke, 1998). As expected from the strong link to the air temperature through the Clausius-Clapeyron relation and a high annual mean relative humidity of 82 % (relative to either water or ice, depending on the air temperature) because of the proximity of a saturated snow surface and the ocean, the seasonal cycle of  $q_{2m}$  closely follows that of temperature.

### 3.3 Results: surface energy balance and melt

#### 3.3.1 SEB model performance and uncertainties

There are several SEB model parameters for which the exact values or formulations are unknown, e.g. the surface roughness length for momentum

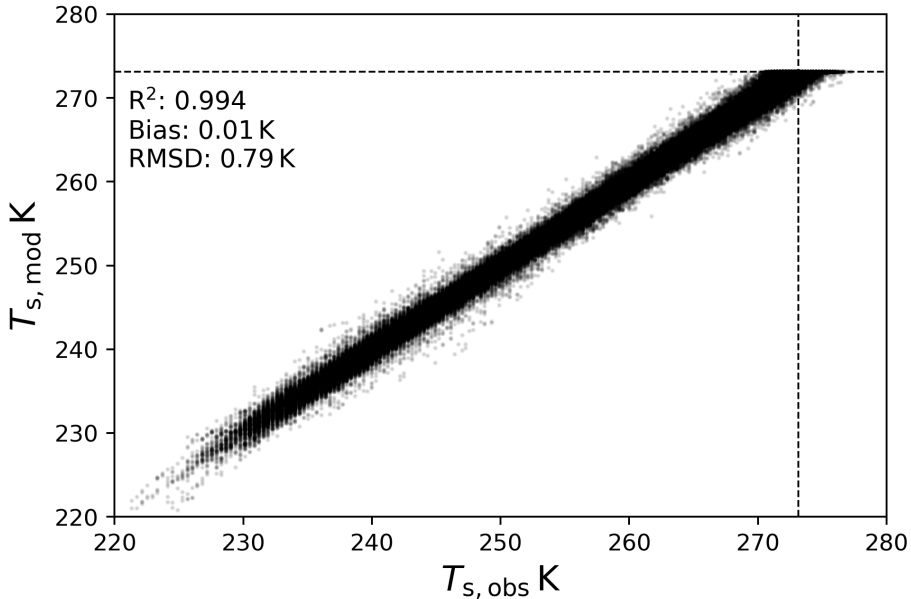


**Figure 3.4** Daily values of modelled versus measured  $T_s$  for the parameter settings used in this study:  $z_{0,m} = 1.65$  mm,  $\rho_{s,0} = 280$  kg m<sup>-3</sup>.

$z_{0,m}$ , the density of new snow  $\rho_s$ , the stability functions (required to calculate the turbulent scales) and the effective conductivity, which couples the magnitude of  $Q_G$  to the temperature gradient in the snow. We estimated the impact of observational and model uncertainties on modelled melt by running the model 600 times while randomly varying all hourly observations within the specified measurement uncertainty ranges (Table 3.1) and using multiple expressions for the heat conductivity and stability functions. Model performance is quantified by comparing modelled with observed  $T_s$  and assessing the changes in modelled 24-year cumulative melt. Note that in this section, the albedo based on observations is used to obtain  $SW_{net}$ .

The choice of expressions for the stability functions and heat conductivity did not significantly impact the modelled amount of melt (total within 30 mm w.e. or 2.7%, not shown). The model outcome is more sensitive to the choice of surface roughness length for momentum  $z_{0,m}$  and the lower

limit of density of new snow  $\rho_{s,0}$ : when  $z_{0,m}$  is varied between 0.5 mm and 50 mm and  $\rho_{s,0}$  between 150 and 500 kg m<sup>-3</sup>, the cumulative amount of surface melt over the 24-year period varies between 900–1220 mm w.e., with higher melt values for smaller values of  $z_{0,m}$  and  $\rho_{s,0}$ . Optimal values in terms of simulated  $T_s$  are  $z_{0,m} = 1.65$  mm and  $\rho_{s,0} = 280$  kg m<sup>-3</sup>, resulting in a  $T_s$  bias of 0.01 K and an RMSD of 0.79 K (Fig. 3.4). We use these values in the remainder of this study.

Figure 3.5a and b show modelled 24-year cumulative melt and annual melt (Mar–Feb) at Neumayer, combined with uncertainties associated with model parameters. The annual mean values for year  $X$  are obtained by averaging monthly values for March of year  $X$  until February of year  $X + 1$ . The total melt amounts to 1154 mm w.e., with a small uncertainty associated with measurement uncertainties ( $1\sigma \approx 3$  mm w.e., i.e. 0.3%). The adopted method to estimate this uncertainty has its limitations, as measurement errors are probably autocorrelated: if a measurement at one time is disturbed in some way, it is probably disturbed in a similar way at the next time step. Therefore, this result could be interpreted as a lower bound of the uncertainty range, which is supported by the larger uncertainty estimates ( $\sim 15\%$ ) by Van den Broeke et al. (2010b), who applied a constant systematic error which can be interpreted as an upper bound on the modelled uncertainty range. This also explains why the model outcome is much more sensitive to different values of  $z_{0,m}$ , as these runs effectively introduce a systematic error between the true (unknown) value and the chosen value. Furthermore, this approach assumes the true value to be constant, which likely is an oversimplification (Smeets and Van den Broeke, 2008).

The sensitivity of modelled cumulative melt to  $z_{0,m}$  is somewhat unexpected. Following Eq. (3.3) both  $z_{0,h}$  and  $z_{0,q}$  decrease for increasing  $z_{0,m}$ ; in combination with the bulk method this acts to dampen the effect of  $z_{0,m}$  on the magnitude of the turbulent fluxes. Our interpretation of this result is that decreasing  $z_{0,m}$  and  $\rho_{s,0}$  leads to a decrease of the turbulent fluxes as well as the ground heat flux  $Q_G$ . This reduces the efficiency with which heat is removed from the surface, in turn allowing more energy to be invested in melt. The obtained value of  $z_{0,m} = 1.65$  mm is high compared to

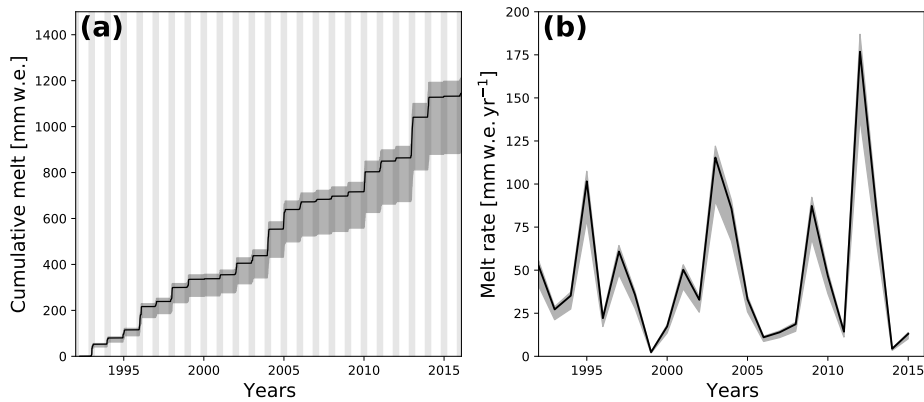


**Figure 3.5** Effect of model uncertainties on **(a)** cumulative melt and **(b)** seasonal melt. The shaded area indicates the  $1\sigma$  range due to model uncertainties (changing  $z_{0,m}$  and  $\rho_{s,0}$  between their respective values). The vertical grey patches in **(a)** indicate Nov–Feb of each season. Note that **(b)** ends earlier than **(a)** because the observations do not cover the 2015–16 melt season entirely.

the average value of  $z_{0,m} = 0.1$  mm found during a field campaign at Neumayer in 1982 (König, 1985) but it is not uncommon for snow surfaces (Amory et al., 2017).

Measured values of  $T_s$  in excess of the melting point in Fig. 3.4 only occurred in the first 6 seasons; from 1998–99 onwards they were removed by additional post-processing. These measurements mainly reflect uncertainties in the adopted unit value of longwave emissivity and in measured  $LW\uparrow$ , e.g. from sensor window heating (Smeets et al., 2018) and the fact that the downward facing radiation sensor also measures longwave radiation emitted by the relatively warm air between the surface and the sensor.

### 3.3.2 Surface energy balance

Annual (Mar–Feb) mean values of near-surface meteorological quantities and SEB components are presented in Table 3.2, with seasonal cycles of

**Table 3.2** Mean annual values and interannual variability (calculated as standard deviations of monthly means) of meteorological variables and SEB components. For precipitation and melt, total annual values are given.

Variable	Yearly mean	Variability
$T_{2\text{ m}}$ (K)	257.1	0.7
$T_s$ (K)	256.0	0.8
$q_{2\text{ m}}$ ( $\text{g kg}^{-1}$ )	1.1	0.1
$V_{10\text{ m}}$ ( $\text{m s}^{-1}$ )	8.9	0.6
$p$ (hPa)	981.6	2.0
$\text{SW}_{\text{net}}$ ( $\text{W m}^{-2}$ )	20	2
$\text{SW}_{\downarrow}$ ( $\text{W m}^{-2}$ )	127	3
$\text{SW}_{\uparrow}$ ( $\text{W m}^{-2}$ )	107	2
$\text{LW}_{\text{net}}$ ( $\text{W m}^{-2}$ )	-28	3
$\text{LW}_{\downarrow}$ ( $\text{W m}^{-2}$ )	218	5
$\text{LW}_{\uparrow}$ ( $\text{W m}^{-2}$ )	246	4
$Q_s$ ( $\text{W m}^{-2}$ )	14.5	2.7
$Q_L$ ( $\text{W m}^{-2}$ )	-6.3	1.2
$Q_G$ ( $\text{W m}^{-2}$ )	0.7	0.4
$M$ ( $\text{W m}^{-2}$ )	0.5	0.4
Precipitation (mm w.e.)	415	86
Melt (mm w.e.)	50	42

SEB components presented in Fig. 3.3b. These show that the summer-time SEB is dominated by the radiation fluxes; despite the high albedo of the snow surface,  $\text{SW}_{\text{net}}$  is the dominant heat source for the skin layer, whereas  $\text{LW}_{\text{net}}$  extracts energy from the surface, most efficiently so in summer when the surface is heated by the sun. In summer,  $Q_L$  becomes a significant heat loss in the SEB (sublimation), preventing strong negative  $Q_s$  (convection). The seasonal cycle of  $Q_G$  is small, indicating a small net transport of heat away from the surface in summer and towards the surface in winter. The net annually integrated amount is less than zero as a result of the refreezing of meltwater, warming the subsurface snow layers.

Statistically significant and previously unreported trends over the full 24-year period (not shown) are detected in  $\text{LW}_{\uparrow}$  ( $-0.28 \pm 0.14 \text{ W m}^{-2} \text{ yr}^{-1}$ ) and  $Q_s$  ( $+0.21 \pm 0.07 \text{ W m}^{-2} \text{ yr}^{-1}$ ). Both of these are a result of wintertime

trends.  $LW\uparrow$  is linked directly to  $T_s$ , which shows a statistically insignificant negative trend ( $-0.029 \pm 0.026 \text{ Kyr}^{-1}$ ), which in magnitude exceeds the negative trend in  $T_{2m}$  ( $-0.0045 \pm 0.02 \text{ Kyr}^{-1}$ ; assuming a normal distribution, the probability that the negative trend in  $T_s$  is greater in magnitude than the trend in  $T_{2m}$  is 0.76). As a result, the air temperature gradient near the surface has increased, enhancing  $Q_S$ . The negative trend in  $T_s$  originates from a decrease in  $LW\downarrow$  ( $-0.26 \pm 0.17 \text{ W m}^{-2} \text{ yr}^{-1}$ ), which is in turn driven by a slight decrease in cloud cover ( $-0.003 \pm 0.001 \text{ yr}^{-1}$ ). This is suggested independently by the decrease in average winter humidity ( $-0.004 \pm 0.002 \text{ g kg}^{-1} \text{ yr}^{-1}$ ). These findings agree with Herman et al. (2013) and Kuipers Munneke et al. (2011a), who determined from satellite observations that summer cloud cover has decreased over that part of coastal Antarctica in the period 1979–2011.

### 3.3.3 Melt season

Melt occurs at Neumayer from November until February (Fig. 3.6), but is highly variable from year to year. The mean annual amount of melt is 50 mm w.e. with an interannual variability of 42 mm w.e. and a range of 2 mm w.e. in 1999–2000 to 176 mm w.e. in 2012–13. Most melt occurs in December and January and the surface only sporadically reaches the melting point in February. Only in 2007 did melt occur in November, and no melt occurs outside these four months.

The cumulative melt occurring at Neumayer shows step-wise increases (Fig. 3.5a), which represent the peaked melt seasons, in which melt occurs on average on  $18 \pm 10$  days. The uncertainty in the number of melt days due to the chosen values of  $z_{0,m}$  and  $\rho_{s,0}$  is relatively small compared to the interannual variability in melt totals (Fig. 3.6), implying that this choice does not significantly affect the modelled melt duration, but it does affect the total melt.

To investigate the link between melt and climate, we compare the two summers with the highest (2003–04 and 2012–13, on average 145 mm w.e.) and lowest (1999–2000 and 2014–15, on average 4 mm w.e.) melt amounts. Figure 3.7 shows the meteorological and SEB components for these years,

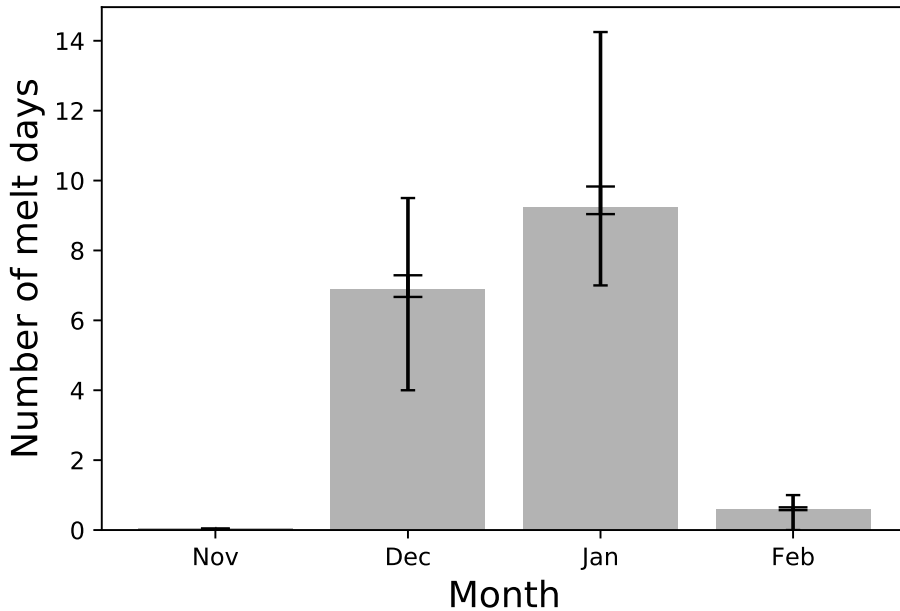


**Figure 3.6** Average number of melt days per month at Neumayer. The inner error bars (with larger caps) indicate the  $1\sigma$  uncertainty range resulting from the runs performed with different settings for roughness length  $z_0$  and lower limit of new snow density  $\rho_{s,0}$  (Sect. 3.3.1). The outer error bars (with smaller caps) indicate the  $1\sigma$  range of the interannual variability.

averaged over December and January. The largest differences are found in  $T_{2m}$  (+2.3 K) and  $SW_{net}$  (+17  $W m^{-2}$ ); based on the measurement uncertainties (Table 3.1), these differences are significant. In cold summers, the low  $T_{2m}$  corresponds to a stronger temperature inversion ( $T_{2m} - T_s$ ), more longwave cooling, less sublimation and a larger  $Q_S$ .  $SW\downarrow$  and  $LW\downarrow$  show almost no difference between high and low melt seasons; therefore, the difference in  $SW_{net}$  cannot be caused by a change in cloud cover and is likely caused solely by surface albedo, which suggests an important role for the snowmelt-albedo feedback. This will be elaborated upon in the next section. Finally, the direction of  $Q_G$  is reversed; in high melt years, the surface is warmed from below while in low melt years the surface loses

heat to the subsurface. More refreezing of meltwater in high melt years warms the near surface snow layers, which in turn leads to a conductive heat flux towards the surface.

Using the subsurface radiation model of Kuipers Munneke et al. (2009), the influence of subsurface penetration of shortwave radiation is estimated. Its inclusion increases the modelled cumulative amount of melt by 13 %, from 1154 mm w.e. to 1326 mm w.e. The absorbed shortwave radiation heats the subsurface layers, but the heat cannot be transported away as effectively as would happen at the surface by turbulent fluxes and long-wave radiation. This leads to an increase in total melt.

The findings presented in this section are in good agreement with Van den Broeke et al. (2010b), who used a similar approach to calculate the SEB at Neumayer, but used a lower value for  $z_{0,m} = 0.32$  mm and a higher snow density that was assumed constant with depth ( $420 \text{ kg m}^{-3}$  in their study versus  $280 \text{ kg m}^{-3}$  in this study). Compared to melt estimates from Larsen C ice shelf, obtained through a similar modelling approach by Kuipers Munneke et al. (2012b), melt at Neumayer is weak. Owing to its more northerly location, on Larsen C ice shelf an annual (2009–2011) average melt energy of  $2.8 \text{ W m}^{-2}$  is obtained, compared to the 2009–2011 annual average of  $0.7 \text{ W m}^{-2}$  obtained at Neumayer; furthermore, in November and February melt occurs much more frequently on Larsen C ice shelf.

### 3.4 Results: the snowmelt-albedo feedback

The snowmelt-albedo feedback is a well-known phenomenon, but has not before been quantified for Antarctica. The feedback occurs after the rapid growth of snow grains when meltwater penetrates into the subsurface and refreezes. Because a photon on average travels farther through snow with large particles than in new snow with smaller particles, the probability of it being absorbed is increased, effectively lowering the surface albedo (Gardner and Sharp, 2010). Even without melt, albedo decreases when snow ages, following grain growth from dry snow metamorphism, but this is a much slower process which mainly depends on temperature gradients in

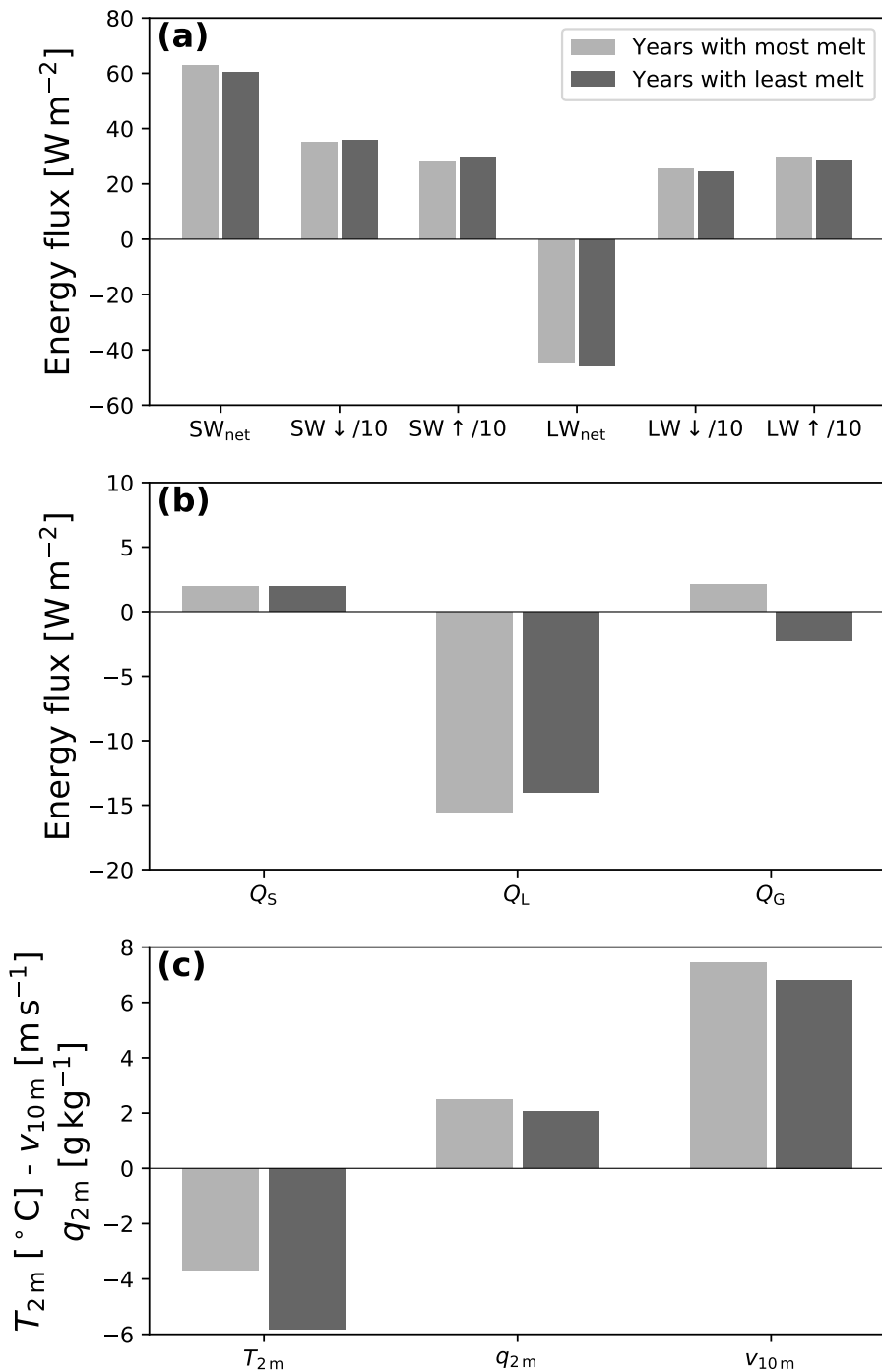


**Figure 3.7** Average values of some SEB components (a) and (b) and some meteorological variables (c) for December and January in the years with the highest (2003–04 and 2012–13, in light grey) and lowest (1999–2000 and 2014–15, in dark grey) amount of melt, as identified in Sect. 3.3.3. Note that  $SW_{\downarrow}$ ,  $SW_{\uparrow}$ ,  $LW_{\downarrow}$  and  $LW_{\uparrow}$  are scaled by a factor of 10 in (a) for clarification.

the snow, favouring moisture transport onto larger grains. Precipitation of new, fine-grained snow has been shown to inhibit the albedo decrease by metamorphism on the Antarctic plateau (Picard et al., 2012).

To quantify the snowmelt-albedo feedback at Neumayer, we need to be able to switch on and off the albedo dependency on melt-driven grain growth. To that end, we implemented an albedo parameterisation in the SEB model, as described in Sect. 3.2.2. Because no data on grain size are available from Neumayer, we optimised the albedo model performance by maximising the correspondence between 1) modelled and observed hourly  $SW\uparrow$ , and 2) the total melt obtained from the calculations based on observed albedo (Sect. 3.4.1). We compare  $SW\uparrow$  instead of the albedo itself because by doing so the hourly values are naturally weighted with its contribution to  $SW_{\text{net}}$  and hence its importance for the SEB. We then perform several runs with different processes switched on and off affecting the surface albedo to investigate the importance of the snowmelt-albedo feedback for melt at Neumayer (Sect. 3.4.2).

### 3.4.1 Optimising the albedo parameterisation

The albedo parameterisation, and especially the expression for snow grain size (Eq. (3.8)) contains several parameters that are not well constrained, such as new snow grain size  $r_{e,0}$  and refrozen snow grain size  $r_{e,r}$ . These parameters were varied within reasonable ranges to optimise the results: new snow grain size between 0.04 mm and 0.3 mm, refrozen snow grain size between 0.1 mm and 10 mm. The best comparison with observed albedo was achieved when using the look-up table for dry snow metamorphism  $dr_{e,\text{dry}}$  corresponding to a grain size of 0.055 mm.

The first step in optimising the parameterisation was to split the summer season into two parts, the ‘dry’ and the ‘wet’ season. The respective starts of the dry and wet seasons are the first day on which the sun rises more than  $15^\circ$  above the horizon and the first day that surface melt occurs. The wet season ends when the sun no longer rises higher than  $15^\circ$ . For the dry season, we varied the dry snow metamorphism factor and the new snow grain size to best match observed  $SW\uparrow$ . This resulted in a new snow grain

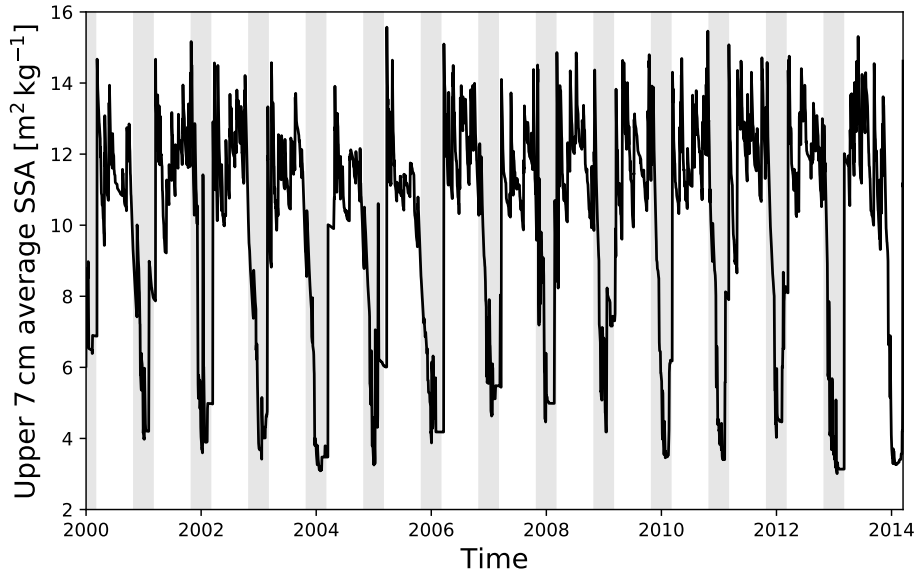


**Figure 3.8** Seasonal cycle of modelled average grain size in the upper 7 cm for the period 2000–2014. The grain size is expressed in terms of specific surface area ( $SSA = \frac{3}{\rho_i r_e}$ ) rather than grain size itself, to allow for a comparison with Fig. 6 of Libois et al. (2015). The vertical grey patches indicate Nov–Feb of each season.

size of 0.25 mm. This value is then used in the second step, in which the refrozen snow grain size  $r_{e,r}$  is varied to best match the modelled cumulative melt using observed albedo. This was achieved for a refrozen snow grain size of 1.45 mm.

This value for refrozen snow grain size is compatible with the typical largest grains in dry metamorphosed snow of  $O(1 \text{ mm})$ , and which Kuipers Munneke et al. (2011b) used as a lower limit for refrozen snow grains. Libois et al. (2015) and Picard et al. (2016) present observations of snow grain sizes on the Antarctic plateau during field campaigns in 2012–13 and 2013–14 as well as estimates from satellite observations. On the plateau, summer temperatures are comparable to Neumayer winter temperatures. Libois et al. (2015) report summertime snow grain size estimates

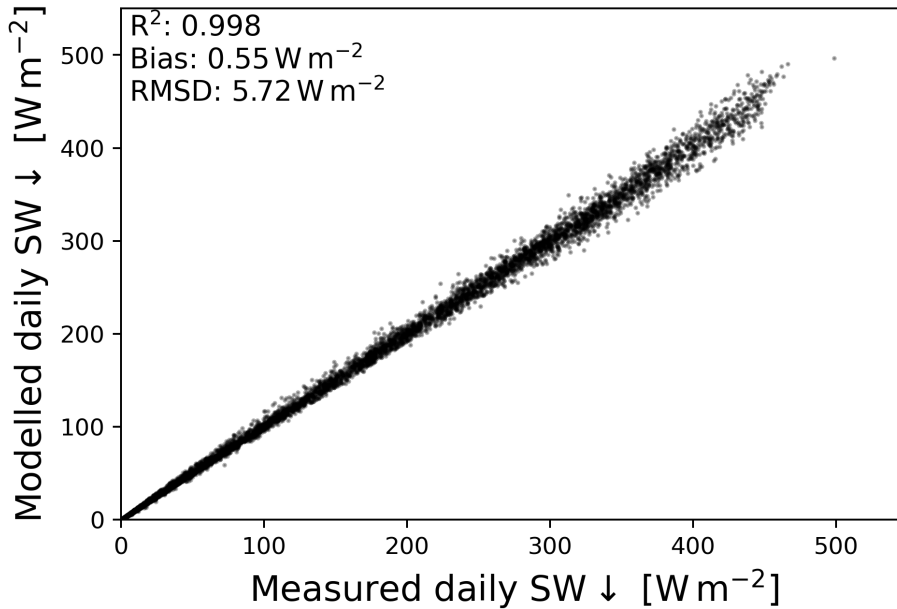


**Figure 3.9** Measured versus modelled daily average incoming shortwave radiation ( $SW\downarrow$ ). The modelled  $SW\downarrow$  is obtained by dividing the hourly measured  $SW\uparrow$  by the hourly modelled albedo.

of approximately 0.11 mm (Fig. 6 in their study, reported as a specific surface area  $SSA = \frac{3}{\rho_i r_e}$ , where  $\rho_i$  is the density of ice and  $r_e$  is the snow grain size). In our study, wintertime snow grain sizes approach 0.21 mm. The difference is expected as the plateau is generally much colder than Neumayer. The seasonal cycle of modelled average specific surface area in the upper 7 cm (Fig. 3.8) is comparable to the one presented in Libois et al. (2015), although the wintertime values are probably too low. For the purpose of this study however, the accurate representation of surface albedo during winter is less relevant as there is no shortwave radiation in winter.

When the adopted albedo values are combined with the observations of  $SW\uparrow$ , the model adequately reproduces the incoming shortwave radiation (Fig. 3.9, bias = +0.93  $W m^{-2}$ , RMSD = 7.3  $W m^{-2}$ ), providing confidence in the modelled albedo.

### 3.4.2 Magnitude of the snowmelt-albedo feedback

Three experiments with the SEB model were carried out in addition to the original run ( $R_0$ ) which uses the measured albedo:

- $R_1$ : the average measured albedo (0.84, determined by adding all  $SW\downarrow$  and  $SW\uparrow$  for all measurements when the Sun is higher than  $15^\circ$  above the horizon and taking the ratio between the two) is prescribed for the entire period;
- $R_2$ : the full albedo parameterisation is used;
- $R_3$ : refrozen snow does not contribute to the changing snow characteristics, i.e.  $f_r = 0$  in Eq. (3.8).

Figures 3.10a and b show time series of modelled cumulative and seasonal surface melt for the four experiments. Experiment  $R_1$  underpredicts melt in most seasons, yielding a mean annual amount of surface melt of  $39 \pm 27$  mm w.e. yr<sup>-1</sup> (compared to  $50 \pm 42$  mm w.e. yr<sup>-1</sup> for experiment  $R_0$ ). More melt was modelled in the 1995–96 melt season, which was characterised by frequent precipitation events and cloudy conditions, keeping observed albedo higher than the long-term mean. Because the albedo parameterisation (used in experiment  $R_2$ ) has been calibrated to match observed albedo, experiment  $R_2$  adequately reproduces the amount of seasonal melt ( $50 \pm 34$  mm w.e. yr<sup>-1</sup>), although melt in e.g. the 2012 melt season is underestimated. Run  $R_3$  represents the situation in which the snowmelt-albedo feedback has been switched off, leading to significantly underpredicted melt ( $21 \pm 16$  mm w.e. yr<sup>-1</sup>).

Defining the strength of the snowmelt-albedo feedback (SMAF) as the ratio between the total seasonal surface melt in experiments  $R_2$  and  $R_3$ , we obtain an average value of 2.6, with a range of 1.3 (1996–97) to 4.8 (1993–94, see Fig. 3.10c). The effect of subsurface penetration of shortwave radiation on this result is estimated by repeating the above experiments with inclusion of the radiation penetration model of Kuipers Munneke et al. (2009). This yielded an average SMAF of 2.3, ranging from 1.5 (2005–06) to 3.2 (2002–03). The main difference between the two experiments is the reduced interannual variability: including penetration of shortwave radiation does not yield SMAF values larger than 3.5. Shortwave radiation penetration heats the subsurface, causing subsurface melt which is

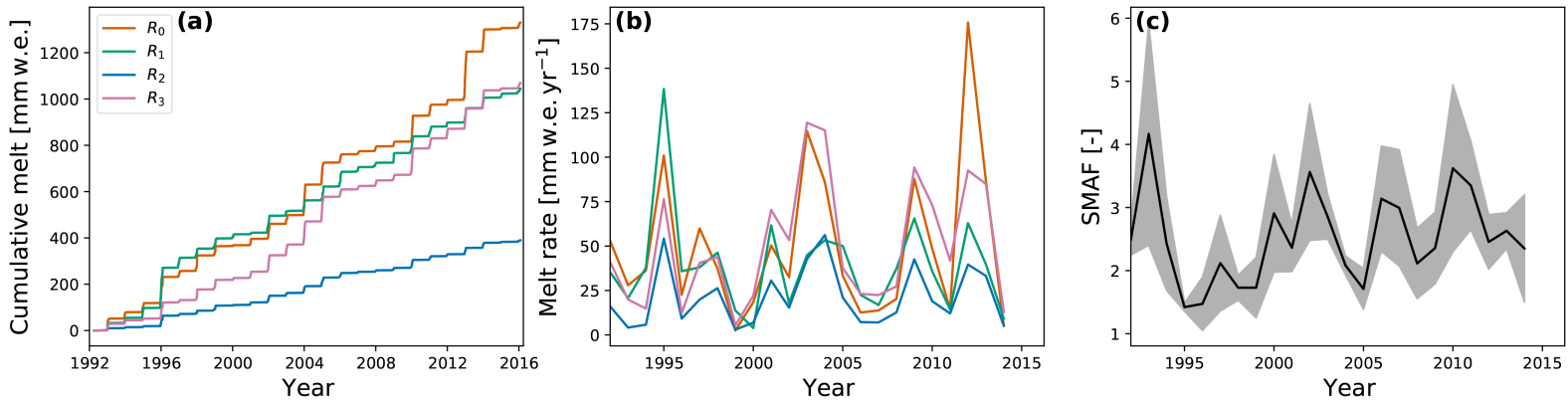


**Figure 3.10** (a) Time series of modelled cumulative amount of melt for the run with measured albedo ( $R_0$ , dark orange), a constant albedo of 0.84 ( $R_1$ , green), a run in which refrozen snow does impact snow grain size ( $R_2$ , blue) and a run in which snow grain size is not influenced by refrozen snow ( $R_3$ , purple). (b) Same as (a) but for seasonal amount of melt. (c) Ratio of modelled surface melt between blue and purple lines in (a) and (b) (runs  $R_2$  and  $R_3$  respectively). The grey area indicates the uncertainty coming from the uncertainty in the determination of  $\tau$  (Fig. 3.2b),  $\pm 5 \text{ W m}^{-2}$  measurement uncertainty in  $\text{SW}\uparrow$  and the inclusion of shortwave radiation penetration.

less affected by the snowmelt-albedo feedback because the radiative flux is smaller in the subsurface. Therefore, the ‘extreme’ years in the sense of SMAF are less distinct in the experiment with shortwave radiation penetration. The effect of shortwave radiation penetration is included in the uncertainties indicated in Fig. 3.10c. Combining this with the uncertainties in observed  $SW\uparrow$  and the determination of  $\tau$  (Fig. 3.2b) leads to uncertainties in the determination of the SMAF of typically 15 %, with a range of 4 % (1995–96) to 32 % (1993–94).

A weak positive correlation was found between SMAF and  $SW\downarrow$  ( $R^2 = 0.15$ ,  $p = 0.07$ ); if  $SW\downarrow$  increases, more energy is available at the surface for melting, which is then in turn further intensified by SMAF. Another weak negative correlation was found between SMAF and summer precipitation ( $R^2 = 0.13$ ,  $p = 0.1$ ); snowfall inhibits SMAF as it effectively ‘resets’ the surface albedo as was also shown by Picard et al. (2012) in a dry region.

Only few studies report on the snowmelt-albedo feedback concerning the darkening of snow rather than disappearance of it. Box et al. (2012) provide relationships between anomalies of seasonal  $T_{2m}$  and  $SW_{net}$  (Fig. 5 and 12 of Box et al. (2012)). They find a negative relationship for accumulation regions, i.e. lower 2 m temperatures are associated with smaller  $SW_{net}$ . No such relationship is found for Neumayer (not shown).

## 3.5 Conclusions

In this study, we used 24 years of high-quality meteorological and radiation observations from the BSRN station Neumayer, situated on Ekström ice shelf, East Antarctica, to force a surface energy balance model. The primary goal was to calculate the amount of melt at Neumayer and to investigate the importance of the snowmelt-albedo feedback. Model performance was evaluated based on the difference between modelled and measured surface temperature, and the modelled melt was tested for measurement and model parameter uncertainties.

We found that measurement uncertainties, when considered random in time, do not significantly impact modelled melt at Neumayer over the full

24-year period ( $<0.5\%$  difference). However, melt amount and model performance are sensitive to the values chosen for the surface roughness length for momentum  $z_{0,m}$  and lower limit of new snow density  $\rho_{s,0}$ , thus accurate measurements of these values would further improve future modelling studies. Our results confirm that melt at Neumayer is an intermittent process, occurring on average on only 18 days each summer, totalling 50 mm w.e. and with an interannual variability of 42 mm w.e. Melt occurs mainly in December and January, sporadically in February and only once melt was modelled in November. Significant and previously unreported trends were found in the net longwave radiation (decreasing) and the sensible heat flux (increasing), but these are unrelated to the melt at Neumayer as they mainly occur in winter and are attributed to a decrease in cloud cover.

The main difference between high and low melt years was found to be surface albedo, implying an important role for the snowmelt-albedo feedback (SMAF). We quantified SMAF by implementing and tuning an albedo parameterisation in the SEB model, which includes the effects of snowfall and wet and dry snow metamorphism on albedo. The albedo parameterisation adequately reproduces the seasonal variability in snow grain size, compared to measurements on the Antarctic Plateau (Libois et al., 2015). Our derived wintertime snow grain sizes at Neumayer are somewhat smaller than the satellite-derived summertime snow grain sizes at the Antarctic Plateau (Libois et al., 2015) owing to the lower temperatures on the plateau. Our main finding is that SMAF on average enhances surface melt at Neumayer by a factor of  $2.6 \pm 0.8$ .

Weak correlations were found of SMAF with summertime  $SW\downarrow$  and precipitation ( $0.1 < R^2 < 0.2$ ). To assess how the importance of the snowmelt-albedo feedback varies spatially and temporally, the next step in this research will be applying this method to other sites in Antarctica and a regional climate model (Van Wessem et al., 2018).

## 4. Evaluation of RACMO2

Surface melt on the coastal Antarctic ice sheet (AIS) determines the viability of its ice shelves and the stability of the grounded ice sheet, but very few in situ melt rate estimates exist to date. Here we present a benchmark dataset of in situ surface melt rates and energy balance from nine sites in the eastern Antarctic Peninsula (AP) and coastal Dronning Maud Land (DML), East Antarctica, seven of which are located on AIS ice shelves. Meteorological time series from eight automatic and one staffed weather station (Neumayer), ranging in length from 15 months to almost 24 years, serve as input for an energy-balance model to obtain consistent surface melt rates and energy-balance results. We find that surface melt rates exhibit large temporal, spatial and process variability. Intermittent summer melt in coastal DML is primarily driven by absorption of short-wave radiation, while non-summer melt events in the eastern AP occur during föhn events that force a large downward directed turbulent flux of sensible heat. We use the in situ surface melt rate dataset to evaluate melt rates from the regional atmospheric climate model RACMO2 and validate a melt product from the QuikSCAT satellite.

### 4.1 Introduction

For most of the Antarctic ice sheet (AIS), the near-surface climate is too cold to allow for widespread or continuous summer melting, such as occurs in the lower ablation zone of the Greenland ice sheet (Bell et al., 2018). Therefore, in most of Antarctica, surface melting is an intermittent process, associated with warm and moist air advection (Scott et al., 2019).

---

This Chapter is published as “A benchmark dataset of in situ Antarctic surface melt rates and energy balance”, *Journal of Glaciology*, **66**(256), 291–302, 2020, doi:10.1017/jog.2020.6.

An exception is the Antarctic Peninsula (AP), where the relatively mild summer climate allows for more extensive melt episodes (Kuipers Munneke et al., 2012a; Barrand et al., 2013; Luckman et al., 2014), while on the east side of the AP föhn events cause episodic surface melt throughout the year (Kuipers Munneke et al., 2018; Wiesenekker et al., 2018).

Most meltwater refreezes in the cold firn, and runoff currently represents a negligible contribution to AIS mass balance (Van Wessem et al., 2018). In spite of this, meltwater lakes are widespread on the AIS (Kingslake et al., 2017; Bell et al., 2017; Stokes et al., 2019), and have the potential to influence its dynamical evolution. On ice shelves in the eastern AP, firn saturation and meltwater ponding have been associated with ice-shelf hydrofracturing (Banwell et al., 2013; Kuipers Munneke et al., 2014). Ice shelves buttress the glaciers that feed them; therefore, ice-shelf disintegration causes glacier acceleration (Scambos et al., 2004), which in turn leads to grounded ice loss and sea level rise.

Trusel et al. (2015) suggest a melt rate threshold for ice-shelf viability of  $725 \text{ mm w.e. yr}^{-1}$ , but with considerable uncertainty associated with firn conditions, basal melt rates and ice-shelf stress regimes. As ice shelves are present along  $\sim 74\%$  of the margins of the AIS (Bindshadler et al., 2011), the developments in the AP could serve as an analogue for future ice-shelf disintegration and ice-sheet destabilisation elsewhere in Antarctica when the climate continues to warm, with different roles for local and large-scale atmospheric circulation and ice dynamics (Nicolas and Bromwich, 2014; Fürst et al., 2016; Reese et al., 2018). That is why a robust quantification and understanding of contemporary Antarctic surface melt is essential for improving future predictions of AIS mass loss and sea level rise (Trusel et al., 2015; DeConto and Pollard, 2016).

Nevertheless, very few studies exist that directly and robustly quantify in-situ surface melt rates in Antarctica. The main reason is that this requires accurate measurements, not only of near-surface climate variables (pressure, wind speed, temperature and humidity) but also incoming and outgoing shortwave and longwave radiation fluxes. Only then can the surface energy balance (SEB) be closed and the energy available for surface melt be quantified (e.g. Reijmer and Oerlemans, 2002; Van den Broeke et al., 2006; Kuipers Munneke et al., 2012b).

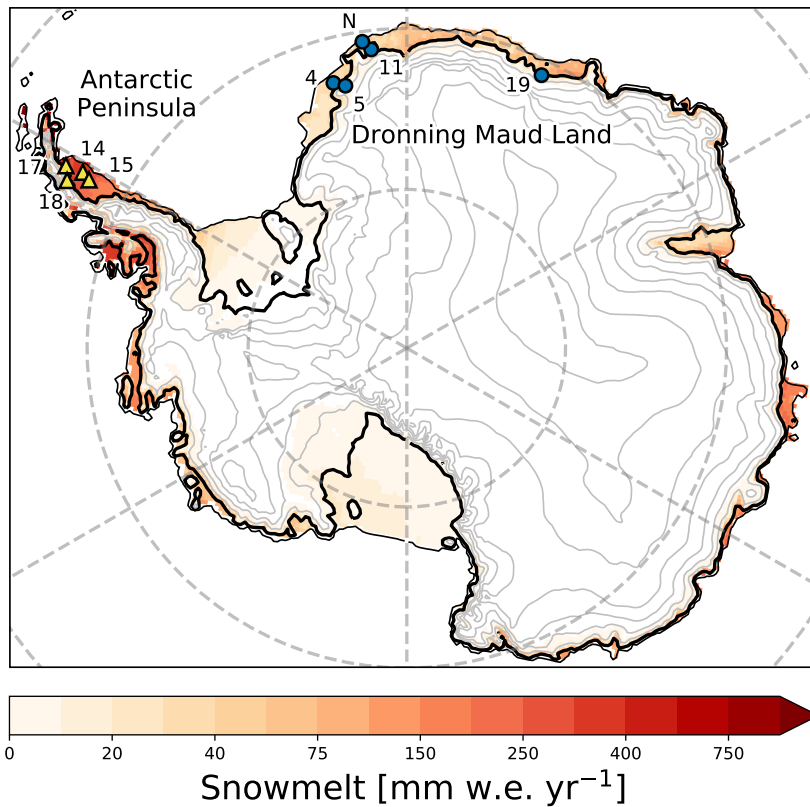


**Figure 4.1** Locations and identifiers of used automatic weather stations in the Antarctic Peninsula (yellow triangles) and Dronning Maud Land (blue dots). Neumayer station is denoted with an N (blue dot). Background colours represent period-average annual melt amounts (1979–2017) as simulated by the regional atmospheric climate model RACMO2 (Van Wessem et al., 2018). The thin black line represents the 10 m height contour (~ shelf edge), the thick black line represents the 150 m height contour (~ grounding line), grey lines indicate 500 m height intervals.

Apart from the remoteness and the harsh climate, in-situ observations in Antarctica are also hindered by accumulating snow, which buries the instruments if they are not regularly raised. Hence, very few Automatic Weather Stations (AWS) or even staffed meteorological stations on the ice

sheet are equipped with radiation sensors (Kuipers Munneke et al., 2014, 2018). The prime long-term (1981-present) site is Neumayer station, located on Ekström ice shelf in Dronning Maud Land (DML), which is part of the Baseline Surface Radiation Network and therefore also provides high-quality radiation measurements. Furthermore, it has the added benefit of being situated on the ice shelf, rather than on ice-free rock with very different surface characteristics (Van den Broeke et al., 2005a, 2010b; König-Langlo and Loose, 2007; Jakobs et al., 2019).

To circumvent the scarcity of suitable in-situ observations, several alternative methods have been developed to assess Antarctic surface melt rates. Temperature–index models rely solely on air temperature records and assume melt to occur when air temperature exceeds 0°C while adopting an index that couples the air temperature to surface melt rate. This method has proven valuable to obtain longer-term regional estimates for Antarctic surface melt patterns (Van den Broeke, 2005; Barrand et al., 2013; Leeson et al., 2017), but lacks a physical basis and properly constrained parameters (Wake and Marshall, 2015); for instance, it does not explicitly resolve the snowmelt–albedo feedback, which has the potential to enhance melt rates threefold in Antarctic regions with intermittent melt (Jakobs et al., 2019). Remote sensing provides a valuable tool for the direct, continent-wide observation of surface melt by measuring surface brightness temperatures (Picard et al., 2007) and by the attenuation of radar waves in the presence of liquid water in the near-surface snow (Trusel et al., 2012). By correlating satellite signal attenuation to in-situ surface melt, continent-wide maps of summer melt totals can be obtained (Trusel et al., 2013). Finally, surface melt rates can be modelled using (regional) climate models (King et al., 2015; Kuipers Munneke et al., 2017; Van Wessem et al., 2018; Donat-Magnin et al., 2019). These models generally perform adequately, but suffer from climate biases and limited resolution that smoothens the topography, especially in topographically steep regions such as the AP and the relatively steep escarpment zone in DML, East Antarctica. This smoothing results in biases in temperature, wind speed and surface melt (Van Wessem et al., 2014a).

All of these methods depend on in-situ observations of melt rates for calibration (temperature–index models, satellite melt rate), validation (satellite melt detection) or evaluation (climate models). That is why building a

benchmark dataset of consistently derived in-situ Antarctic melt rate observations is crucial. As of today, most studies that have explicitly quantified the SEB and melt rate in Antarctica were restricted to a single location, for example Larsen C ice shelf in the AP (Kuipers Munneke et al., 2012b; King et al., 2015, 2017), Berkner Island (Reijmer et al., 1999) or glaciers situated on islands close to the AP (e.g. Bintanja, 1995; Jonsell et al., 2012; Falk et al., 2018). While these studies provide important information about surface melt and its temporal variability, their spatial coverage remains limited.

Here we present a benchmark dataset of Antarctic surface melt rates and energy balance from one staffed research station (Neumayer) and eight Automatic Weather Stations (AWS). All sites are located in the Atlantic sector of Antarctica, ranging from the eastern Antarctic Peninsula (AP) to Dronning Maud Land (DML, Fig. 1). Although some individual results from Neumayer and three AWS have been published before (e.g. Van den Broeke et al., 2010b; Kuipers Munneke et al., 2012b, 2018; King et al., 2015, 2017; Wiesenekker et al., 2018; Jakobs et al., 2019), this study expands on previous work by updating the time series, using a single surface energy balance (SEB) model framework to process all station data and determine uncertainties in a consistent manner. Subsequently, we use the resulting in-situ melt data to assess the validity of simplified temperature-index models, evaluate Antarctic surface melt from the regional climate model RACMO2 and validate the QuikSCAT satellite melt product.

In the next section we describe the instruments used on the weather stations and introduce the SEB model. Next, we present the dataset and discuss its main characteristics including annual averages and seasonal and daily variability. We proceed to use the new dataset to calibrate, evaluate and validate alternative Antarctic melt products, followed by conclusions.

## 4.2 Methods

### 4.2.1 Automatic weather stations

Since 1995, the Institute for Marine and Atmospheric Research of Utrecht University (IMAU) has deployed and maintained 19 automatic weather

stations (AWS) in Antarctica. As of November 2019, four of these AWS are still operational. The stations have technically evolved from Type 1 (T1) to Type 3 (T3) (Table 4.1, see also Smeets et al., 2018). Here we only use data of T2 and T3 AWS as these measure the full radiation balance, i.e. incoming and reflected broadband shortwave radiation,  $SW\downarrow$  and  $SW\uparrow$ , and downward and upward broadband longwave radiation,  $LW\downarrow$  and  $LW\uparrow$ . In addition, the AWS measure near-surface air temperature ( $T$ ), wind speed (WS), wind direction (WD), relative humidity (RH), instrument height ( $H$ ), air pressure ( $p$ ) and snow temperature ( $T_{sn}$ ) at various depths. Specifications of the used sensors are presented in Table 4.1.

The stations sample every six minutes, after which 2-hourly (T2, until January 2001), hourly (T2, from January 2001 onwards) or half-hourly (T3) means are calculated, stored locally and transmitted through the Argos satellite system. The AWS are powered by lithium batteries, while T3 stations in addition use solar cells. The temperature/humidity and radiation sensors are not ventilated because of energy considerations, which may negatively affect their performance. The magnitude of the resulting error depends on the amount of incoming and reflected solar radiation, the wind speed and the type of radiation shield used (Van den Broeke et al., 2004c). Bintanja (2000) and Van As et al. (2005) show that, based on a comparison with ventilated instruments, the radiation error does not exceed the sensor accuracy listed in Table 4.1 for the T2 stations.

Due to the low temperatures encountered at several sites, some of the sensors are operated outside of their range of operational specifications. This mostly affects the relative humidity and longwave radiation observations. The relative humidity observations are corrected based on the method described by Anderson (1994) and Van den Broeke et al. (2004a). The accuracy of the radiation sensors, which are affected by icing/riming, tilt, low sun angles and window heating offset, is discussed in Van den Broeke et al. (2004c). They conclude that with an accuracy of 5% for the daily averages, the radiation sensors perform better than their specifications; we follow their methods to check for rime formation. To reduce net shortwave radiation errors on sub-daily time scales, we calculate a 24 h running mean albedo, which is then applied to the reflected shortwave radiation to obtain incoming and net shortwave radiation fluxes. For all variables, erroneous values were removed by automated and manual detection.

**Table 4.1** Sensors used on the different type of automatic weather stations. EADT = Estimated Accuracy for Daily Totals. For technical details of the observations at Neumayer the reader is referred to König-Langlo and Loose (2007) and Jakobs et al. (2019).

Sensor	Station type	Sensor Type	Range	Accuracy
Atmospheric pressure	T2	Vaisala PTB101B	600–1060 hPa	±4 hPa
	T3	Freescale Xtrinsic MPL3115A2	200–1100 hPa	±0.4 hPa
Air temperature	T2	Vaisala HMP35AC	-80–56°C	±0.3°C
	T3	NTC thermistor	-60–40°C	<0.1°C
Relative humidity	T2	Vaisala HMP35AC	0–100 %	±2% (RH<90 %) 3% (RH>90 %)
	T3	Sensirion SHT35	0–100 %	±1.5 %
Wind speed	T2/3	Young 05103	0–60 m s <sup>-1</sup>	±0.3 m s <sup>-1</sup>
Wind direction	T2/3	Young 05103	0–360°	±3°
Pyranometer	T2	Kipp and Zonen CNR1	305–2800 nm 0–2000 W m <sup>-2</sup>	±10 % EADT
	T3	Kipp and Zonen CNR4	300–2800 nm 0–2000 W m <sup>-2</sup>	±10 % EADT
Pyrradiometer	T2	Kipp and Zonen CNR1	5–50 μm -250–250 W m <sup>-2</sup>	±10 % EADT
	T3	Kipp and Zonen CNR4	4.5–42 μm -250–250 W m <sup>-2</sup>	±10 % EADT
Sonic height ranger	T2	Cambell SR50	0.5–10 m	0.01 m or 0.4 %
	T3	MaxBotix HRXL MaxSonar WRS	0.5–5 m	<1 %

We use data of four AWS on ice shelves in the eastern AP and four in Dronning Maud Land (DML), East Antarctica (indicated in Fig. 4.1). Furthermore, we use data of Neumayer Station, located on Ekström ice shelf in DML (König-Langlo, 2017) (also indicated in Fig. 4.1). The Neumayer meteorological observatory is operated by the Alfred Wegener Institute and is part of the Baseline Surface Radiation Network, a global network of artificially ventilated, high-quality radiation observations, with instantaneous individual broadband fluxes more accurate than 5 W m<sup>-2</sup> (see König-Langlo and Loose (2007) for technical specifications and Jakobs et al. (2019) for measurement accuracies). The same variables are mea-

**Table 4.2** Overview of AWS used in this study: locations, elevations and period of operation (see also Fig. 4.1). Except for AWS 5 and 11, all stations are located on ice shelves (denoted by IS).

Station name	Latitude (°S)	Longitude (°E)	Elevation (m a.s.l.)	Time period	Geographical location
Dronning Maud Land					
Neumayer	70.63	-8.26	17	Apr 92 – Jan 16	Ekström IS
AWS 4	72.75	-15.48	35	Dec 97 – Dec 02	Riiser-Larsen IS
AWS 5	73.1	-13.17	~360	Feb 98 – Feb 14	Aboa/Wasa stations
AWS 11	71.17	-6.8	~690	Jan 07 – Jan 19	Halvfarryggen ice rise
AWS 19	70.95	26.27	~50	Dec 14 – Feb 16	Roi Baudouin IS
Antarctic Peninsula					
AWS 14	67.02	-61.5	~50	Jan 09 – Jun 15	Larsen C IS
AWS 15	67.57	-62.15	~50	Jan 09 – May 14	Larsen C IS
AWS 17	65.93	-61.85	~50	Feb 11 – Mar 16	Larsen B IS (remnant)
AWS 18	66.4	-63.73	~70	Nov 14 – Sep 18	Cabinet Inlet, Larsen C IS

sured at Neumayer as by the AWS except for the sonic height ranger, which is not present at Neumayer. Instead, height changes are measured at Neumayer by weekly stake measurements.

Table 4.2 provides station names, locations, altitudes and observation period of the stations used in this study. AWS 4 was located on the flat Riiser-Larsen ice shelf, AWS 5 was located inland of the grounding line in the steep escarpment zone, dominated by katabatic winds (Van den Broeke et al., 1999; Van Wessem et al., 2014a). Neumayer is located on Ekström ice shelf, which is prone to low-pressure systems passing north of the station. This results in frequent strong synoptically-forced easterly winds, advecting warm moist air (Herman et al., 2013). AWS 11 was located relatively close to Neumayer but on an ice rise; its higher elevation leads to significantly less surface melt. AWS 19 was located close to the grounding line on the Roi Baudouin ice shelf, where föhn winds occur frequently (Lenaerts et al., 2017). In the AP, AWS 18 is also prone to frequent föhn events, located close to the grounding line just east of the AP mountain range (Kuipers Munneke et al., 2018; Wiesenekker et al., 2018). Farther from the grounding line on the flat ice shelf, AWS 14 and 15 are affected much less by föhn winds. AWS 17 was located more to the north on Scar Inlet, the Larsen B remnant. Because of the northerly location, it experienced more melt than AWS 14 and 15.

### 4.2.2 Surface Energy Balance model

Surface melt energy is calculated by solving the Surface Energy Balance (SEB) equation:

$$\begin{aligned} M &= SW \downarrow + SW \uparrow + LW \downarrow + LW \uparrow + Q_S + Q_L + Q_G \\ &= SW_{\text{net}} + LW_{\text{net}} + Q_S + Q_L + Q_G, \end{aligned} \quad (4.1)$$

in which  $SW_{\text{net}}$  and  $LW_{\text{net}}$  are the net short- and longwave radiation fluxes,  $Q_S$  and  $Q_L$  are the turbulent fluxes of sensible and latent heat,  $Q_G$  the conductive subsurface heat flux, and  $M$  the energy available for surface melt respectively. By convention, positive fluxes are directed towards the surface. The turbulent fluxes  $Q_S$  and  $Q_L$  are calculated using the flux-profile method between the measurement level and the surface, using Monin-Obukhov similarity theory with the stability functions from Dyer (1974) for unstable conditions and those from Holtslag and De Bruin (1988) for stable conditions. Energy added through liquid precipitation is neglected as rainfall is rare in Antarctica.

$M$  is zero when the surface temperature  $T_s$  is below the freezing point (273.15 K).  $T_s$  is derived by assuming the energy balance equation to be valid for an infinitesimally thin surface layer (*skin* layer). To that end, all terms in Eq. (4.1), apart from  $SW_{\text{net}}$  and  $LW_{\text{net}}$ , are expressed as a function of  $T_s$  after which Eq. (4.1) is solved iteratively for  $T_s$  so that the SEB is closed. A more detailed description of the model can be found in Reijmer et al. (1999).

The snowpack is initialised with 70 layers of varying thickness: 1 cm at the top, gradually increasing to 2 m at 25 m. The lowest layer is kept at a constant, prescribed temperature: the annually averaged air temperature. Layer thickness can vary as a result of dry snow densification, meltwater refreezing and mass changes by sublimation or deposition. Meltwater percolation is modelled with the tipping-bucket method (e.g. Ligtenberg et al., 2014), in which meltwater is assumed to percolate downwards instantaneously when a layer has reached its maximum capillary retention, which is parameterised following Schneider and Jansson (2004). Short-wave radiation penetration into the subsurface is calculated using a spectral model from Kuipers Munneke et al. (2009), based on Schlatter (1972)

and Brandt and Warren (1993). Temperature and specific humidity are recalculated to 2 m values and wind speed to 10 m values using Monin-Obukhov similarity theory.

For all stations, we use the same constant value for surface momentum roughness length  $z_{0,m}$  of 1.65 mm, following Jakobs et al. (2019). Currently, insufficient data are available to make  $z_{0,m}$  time-dependent across the stations in a consistent manner. The surface roughness lengths for moisture and heat are calculated using the expressions of Andreas (1987). The density of new snow is determined for each station separately by running the model multiple times and minimising the difference between modelled  $T_s$  and observed  $T_s$  derived from LW $\uparrow$ . The sensitivity to different choices for  $z_{0,m}$ , new snow density and the inclusion of shortwave radiation penetration are used to estimate the uncertainty in the determined heat fluxes and surface melt rates following the method outlined in Jakobs et al. (2019).

## 4.3 Results

### 4.3.1 Annual means and seasonal cycles

Table 4.3 lists annual (July–June) totals (snowmelt, sublimation) and average values of climatological variables and SEB components for the nine sites. Surface melt and sublimation rates are expressed in mm w.e. yr<sup>-1</sup>, which is equal to kg m<sup>-2</sup> yr<sup>-1</sup>. Uncertainties in  $Q_S$ ,  $Q_L$ ,  $Q_G$ ,  $M$ , snowmelt and sublimation are derived from sensitivity experiments (following Jakobs et al., 2019), the other uncertainties are derived from measurement uncertainties (Table 4.1). The large uncertainty in  $Q_G$  is a result of taking radiation penetration into account; when it is accounted for, energy that would have been provided to the surface by SW $\downarrow$  is instead absorbed in the subsurface, which is eventually provided to the surface through  $Q_G$ .

The table shows that in general, stations on the eastern AP ice shelves experience typically an order of magnitude more melt than those in DML (Table 4.3), mainly driven by the difference in annual average net radiation  $R_{\text{net}}$  ( $\equiv \text{SW}_{\text{net}} + \text{LW}_{\text{net}}$ ). Although SW $\downarrow$  is slightly larger in the AP, the

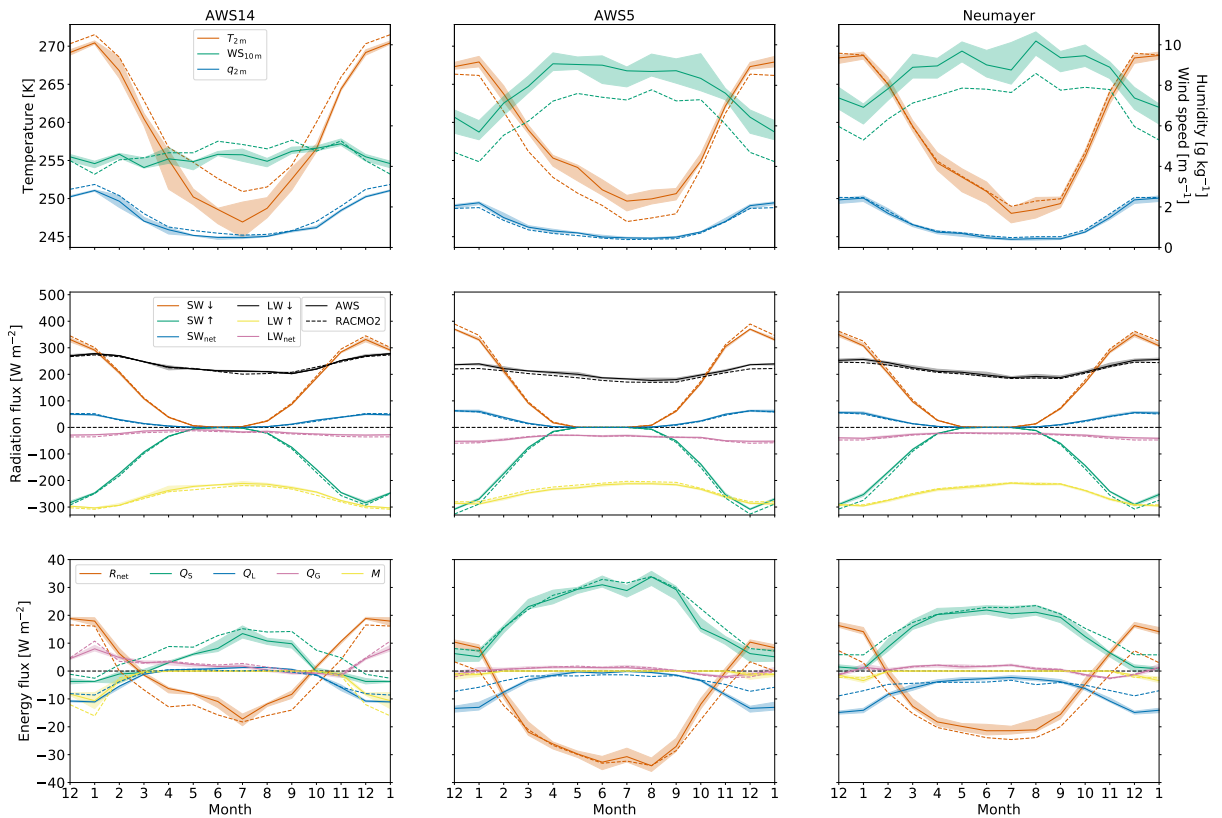
higher precipitation amounts increase the surface albedo sufficiently to result in an  $SW_{\text{net}}$  similar to what is observed in DML. However, the warmer air on the eastern AP ice shelves increases  $LW\downarrow$ , resulting in a larger  $R_{\text{net}}$ . Subsequently, the larger  $Q_G$  is a result of refreezing that occurs in the subsurface snow layers. Refreezing raises the subsurface temperature, and keeps it close to the melting point after melt events.

Figure 4.2 shows the seasonal cycles of monthly average 2 m temperature, specific humidity and 10 m wind speed (top row), the radiation balance (middle row) and the SEB components (bottom row) for AWS 14, 5 and Neumayer. These three locations were selected because of their relatively long observation period, which demonstrates that they represent three distinct climate regions: the eastern AP ice shelves (AWS 14, left column) and for DML an inland and coastal ice shelf location (AWS 5 and Neumayer, centre and right). The shading in Fig. 4.2 indicates the standard deviations of the monthly means.

A comparison of the seasonal cycles shows that the highest summer near-surface temperatures are observed in the eastern AP, owing to its more northerly location and exposure to milder maritime air masses. In winter, an interesting result is that AWS 5 and Neumayer, located in DML, experience higher temperatures than the eastern AP. This is caused by stronger wintertime winds at the DML stations, typically  $8\text{--}10\text{ m s}^{-1}$  (Van den Broeke et al., 2004b), compared to  $4\text{ m s}^{-1}$  at AWS 14 (Kuipers Munneke et al., 2012b; King et al., 2015). The climate of AWS 5, which is located in the escarpment zone, is characterised by katabatic winds that efficiently mix relatively warm air from aloft towards the surface, preventing the formation of a strong surface-based temperature inversion and leading to warming of the surface and near-surface air (Van den Broeke et al., 1999; Van Wessem et al., 2014a). At Neumayer, the ice-shelf surface is nearly flat and the resulting katabatic forcing is weak. Here, the higher wind speeds are synoptic in nature, owing to the vicinity of the Atlantic climatological low-pressure system and the associated passage of low-pressure systems to the north of the station (Herman et al., 2013). In contrast, AWS 14, also located on a flat ice shelf, is under the influence of cold air that is transported by barrier winds along the spine of the AP (Turner et al., 2002); in combination with the relatively low wind speeds,

**Table 4.3** Annual (Jul–Jun) values of climatological variables and SEB components for AWS and Neumayer station. \*The values of AWS19 are averages of Jan–Dec, as there is no full Jul–Jun period available for that station. The top row indicates whether the station is located in Dronning Maud Land (DML) or the Antarctic Peninsula (AP), the third row indicates the period of observation (mm/yy–mm/yy). Uncertainties in  $Q_S$ ,  $Q_L$ ,  $Q_G$ ,  $M$  (melt energy),  $SM$  (snowmelt) and  $SU$  (sublimation) are derived from sensitivity experiments (following Jakobs et al., 2019), the other uncertainties are derived from measurement uncertainties (Table 4.1).

Variable	DML					AP			
	Neumayer 4/92–1/16	AWS 4 12/97–12/02	AWS 5 2/98–2/14	AWS 11 1/07–1/19	AWS 19* 12/14–2/16	AWS 14 1/09–6/15	AWS 15 1/09–5/14	AWS 17 2/11–3/16	AWS 18 11/14–9/18
$T_{2m}$ (K)	257.1 ± 0.1	254.4 ± 0.3	257.1 ± 0.3	256.0 ± 0.3	259.0 ± 0.3	257.6 ± 0.3	257.4 ± 0.3	258.8 ± 0.4	260.9 ± 0.3
$q_{2m}$ (g kg <sup>-1</sup> )	1.1 ± 0.0	1.0 ± 0.0	1.0 ± 0.0	1.0 ± 0.0	1.2 ± 0.0	1.3 ± 0.0	1.3 ± 0.0	1.3 ± 0.0	1.5 ± 0.0
$WS_{10m}$ (m s <sup>-1</sup> )	8.9 ± 0.6	6.4 ± 0.4	8.1 ± 0.4	9.6 ± 0.4	9.9 ± 0.4	4.5 ± 0.4	4.6 ± 0.4	4.8 ± 0.4	3.6 ± 0.4
$SW↓$ (W m <sup>-2</sup> )	128 ± 5	123 ± 27	130 ± 29	127 ± 28	140 ± 28	130 ± 29	128 ± 29	138 ± 31	134 ± 30
$SW↑$ (W m <sup>-2</sup> )	-107 ± 5	-107 ± 24	-108 ± 24	-109 ± 25	-117 ± 25	-112 ± 25	-114 ± 25	-115 ± 26	-122 ± 27
$SW_{net}$ (W m <sup>-2</sup> )	20.4 ± 0.4	16 ± 4	22 ± 5	18 ± 4	23 ± 4	19 ± 4	15 ± 3	24 ± 5	17 ± 4
$LW↓$ (W m <sup>-2</sup> )	218 ± 5	222 ± 15	205 ± 15	214 ± 15	214 ± 15	242 ± 15	240 ± 15	238 ± 15	240 ± 15
$LW↑$ (W m <sup>-2</sup> )	-246 ± 5	-237 ± 15	-241 ± 15	-237 ± 15	-258 ± 15	-254 ± 15	-248 ± 15	-257 ± 15	-268 ± 153
$LW_{net}$ (W m <sup>-2</sup> )	-28 ± 4	-24 ± 10	-39 ± 10	-27 ± 10	-39 ± 10	-20 ± 10	-20 ± 10	-18 ± 10	-19 ± 10
$R_{net}$ (W m <sup>-2</sup> )	-8 ± 3	-8 ± 14	-17 ± 15	-9 ± 14	-16 ± 14	-1 ± 14	-5 ± 13	6 ± 15	-2 ± 13
$Q_S$ (W m <sup>-2</sup> )	14.2 ± 0.8	10 ± 1	21 ± 2	12.3 ± 0.7	20.4 ± 0.7	3.7 ± 0.1	7.6 ± 0.5	0.8 ± 0.6	10 ± 1
$Q_L$ (W m <sup>-2</sup> )	-6.4 ± 0.3	-2.1 ± 0.3	-5 ± 1	-3.9 ± 0.2	-5.3 ± 0.2	-3.0 ± 0.1	-2.6 ± 0.2	-6.9 ± 0.2	-7.2 ± 0.5
$Q_G$ (W m <sup>-2</sup> )	1 ± 8	0 ± 7	0 ± 9	0 ± 6	3 ± 6	2 ± 7	2 ± 5	4 ± 7	4 ± 4
$M$ (W m <sup>-2</sup> )	-0.5 ± 0.1	-0.2 ± 0.4	-0.1 ± 0.1	-0.1 ± 0.0	-2.1 ± 0.2	-2 ± 3	-2 ± 2	-4 ± 4	-5 ± 4
$SM$ (mm w.e. yr <sup>-1</sup> )	50 ± 3	14 ± 6	34 ± 7	7 ± 2	196 ± 2	213 ± 13	139 ± 12	405 ± 9	451 ± 32
$SU$ (mm w.e. yr <sup>-1</sup> )	71 ± 3	23 ± 4	50 ± 15	40 ± 2	59 ± 2	33.5 ± 0.9	29 ± 3	76 ± 3	81 ± 5



**Figure 4.2** Seasonal cycles (based on monthly means) of near-surface climate, surface radiation and surface energy balance for AWS 14 (left column), AWS 5 (centre column) and Neumayer (right column). The top panels show the seasonal cycles of 2 m temperature, 10 m wind speed and 2 m specific humidity. The middle panels show the seasonal cycles of upward and downward broadband radiation fluxes, as well as net radiation, and the bottom panels show the seasonal cycles of the SEB components. The shading indicates the standard deviations of the monthly means, based on the available period. December and January are repeated for clarity. Note that these average seasonal cycles are derived using data from different time periods (see Table 4.2). Output for the same period from RACMO2 are shown with dashed lines.

this enables the formation of a strong surface-based temperature inversion, which keeps the climate of Larsen C ice shelf relatively cold in winter (Marshall and King, 1998).

The seasonal cycles of the radiation balance (Fig. 4.2, middle row) show that the minimum in  $LW\downarrow$  is shifted by 1–2 months with respect to  $SW\downarrow$ .

This is a result of the delay in atmospheric heating in response to slow ambient warming. Net radiation is strongly negative in winter and becomes weakly positive in summer, when in spite of the high surface albedo, absorbed shortwave radiation exceeds the longwave energy loss. Furthermore, as a result of the longer polar night at AWS 5 and Neumayer, the net radiation flux is negative for a longer period than at AWS 14. As stated above, strong winds at AWS 5 and Neumayer enhance  $Q_S$ , increasing the surface temperature and therewith longwave radiation heat loss (Van den Broeke et al., 2010b; Jakobs et al., 2019). As a result, net radiation at AWS 14 is  $\sim 10 \text{ W m}^{-2}$  higher in summer and  $\sim 20 \text{ W m}^{-2}$  higher in winter compared to AWS 5 and Neumayer. The resulting annual mean net radiation flux is almost zero at AWS 14, while it is negative at AWS 5 and Neumayer station. At AWS 17, annual net radiation is positive. The reason for this is twofold: at this site, regular melting decreases surface albedo; owing to the dry climate, the albedo is not frequently reset by fresh snow, thus increasing  $SW_{\text{net}}$ . Secondly, the absence of katabatic winds over the flat ice shelf reduces turbulent heating of the surface, limiting longwave heat losses.

The seasonal cycles of all SEB components (Fig. 4.2, bottom row) show how the differences in surface climate impact surface energy exchange and melt rate. In winter, the high wind speeds at sites AWS 5 and Neumayer result in larger  $Q_S$ , heating the surface and cooling the atmosphere. This results in additional longwave heat loss, leading to more negative wintertime net radiation (Van den Broeke et al., 2010b; Jakobs et al., 2019). This process is much weaker at AWS 14, where wind speeds are low year-round. In summer at AWS 14,  $Q_S$  becomes negative, indicating the presence of a (daytime) weakly convective boundary layer (Kuipers Munneke et al., 2012b; Välisuo et al., 2014; King et al., 2015). This is a result of the regular occurrence of melt at this site: it lowers the albedo through wet snow metamorphism, enhancing  $SW_{\text{net}}$  and creating negative surface-to-air temperature gradients before melting starts. Surface warming is further enhanced through  $Q_G$ , which increases significantly in response to warming of the subsurface snow when meltwater refreezes. As melt rates are small at AWS 5 and Neumayer, these effects are weaker there. At all three stations, sublimation ( $Q_L$ ) becomes the largest source of heat loss in summer, when temperatures are sufficiently high to allow for signifi-

cant surface-to-air specific humidity gradients. At AWS 14,  $Q_L$  becomes weakly positive in winter, indicating deposition of atmospheric moisture (rime formation) at the surface (Kuipers Munneke et al., 2012b; Välisuo et al., 2014; King et al., 2015).

At all stations, average summer melt energy is typically small, and all SEB components are important in determining its magnitude. To look at the surface melt process in more detail, the following section discusses two case studies, using the full temporal resolution of the dataset.

### 4.3.2 Two case studies: meteorological drivers of surface melt

The high temporal resolution of the dataset provides an opportunity to investigate surface melt and its drivers more closely. Figure 4.3 contrasts two melt events in DML (AWS 4 and AWS 5, 27–31 December 1998, left) and on Larsen C ice shelf in the eastern AP (AWS 14 and AWS 18, 7–13 April 2015, right). Note that the AP AWS store data at hourly intervals, while AWS 4 and 5 stored data at a two-hourly time resolution. AWS 4 was situated on the flat Riiser-Larsen ice shelf and AWS 5 85 km to the ESE, just off the shelf on the grounded ice sheet, but still close to sea level. At this small distance, they experience similar daily cycles. In this relatively cold part of Antarctica, surface melt is intermittent and only occurs during daytime in summer, when insolation is strong enough to raise the surface temperature to the melting point.

The selected midsummer period (27–31 December 1998) for AWS 4 and 5 represents a radiation-dominated melt event typical for this location; these daily cycles during the midnight sun are dominated by the net radiation flux being positive when solar radiation is sufficiently large and negative otherwise (Fig. 4.3a and b). Melt occurs when net radiation becomes significantly positive ( $\sim 50 \text{ W m}^{-2}$ ) and surface heat sinks (convection, sublimation, subsurface heat conduction) are not strong enough to prevent the surface from reaching the melting point.

While both stations experience roughly similar meteorological conditions (Fig. 4.4a–d), melt does not necessarily occur simultaneously at the two

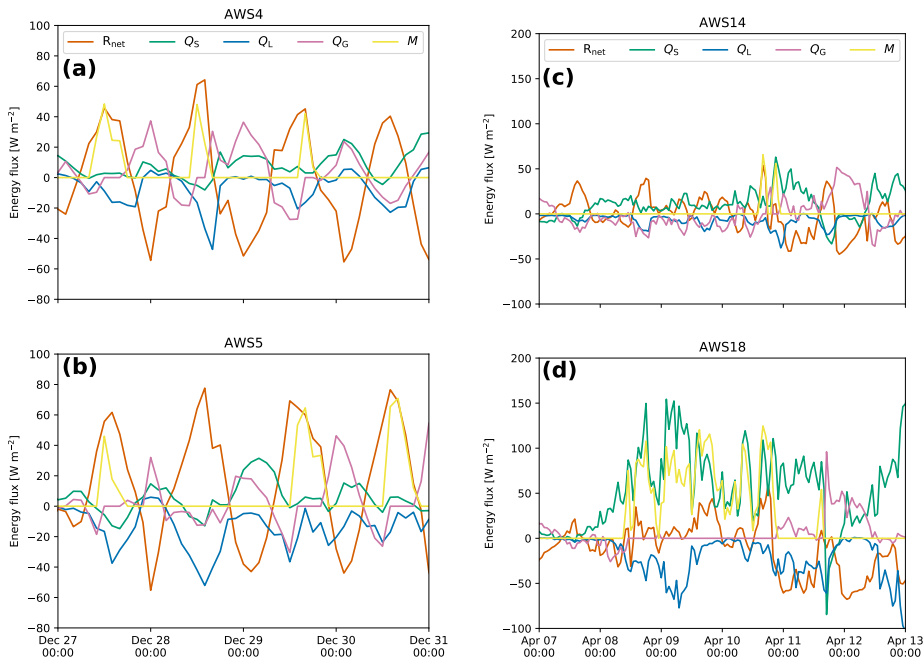


**Figure 4.3** High-resolution time series of SEB components for AWS 4 and 5 in Dronning Maud Land (**a** and **b**, 27–31 Dec 1998, 2 h resolution) and AWS 14 and 18 in the Antarctic Peninsula (**c** and **d**, 7–13 Apr 2015, 1 h resolution). Note the different vertical axes (**a** and **b** compared to **c** and **d**).

locations. For example, on 28 December 1998 melt occurred at AWS 4 but not at AWS 5; on this day, a lower relative humidity and a higher wind speed at AWS 5 enabled stronger sublimation, removing sufficient energy from the surface to prevent surface melt. Note that  $R_{net}$  was similar at both stations: the higher cloud cover at AWS 4 reduced  $SW_{net}$  but increased  $LW_{net}$ , which effectively cancelled each other.

Conversely, two days later on 30 December 1998, melt occurred at AWS 5 but not at AWS 4, with higher winds and surface cooling by sublimation this time occurring over the ice shelf. We conclude that surface melt in coastal DML is the result of a delicate balance between daytime surface heat sources and heat sinks, and highly sensitive to differences in cloud cover, atmospheric humidity and wind speed.

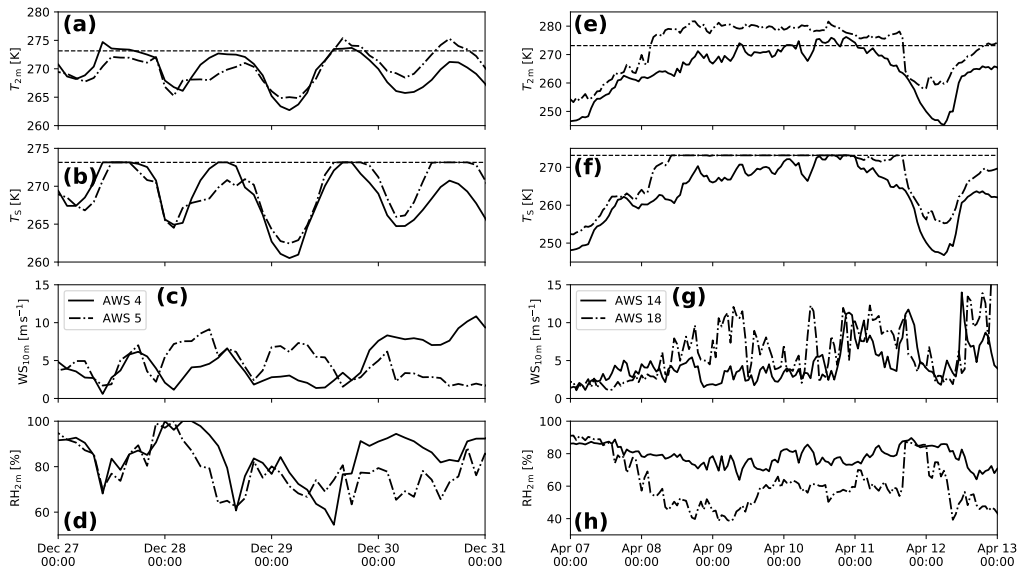


**Figure 4.4** Time series of  $T_{2m}$ ,  $T_s$ ,  $WS_{10m}$  and  $RH_{2m}$  for AWS 4 and 5 (a–d) and AWS 14 and 18 (e–h) for the same periods as in Fig. 4.3.

On Larsen C ice shelf, surface melt also occurs in non-summer months and even during the polar night. Under the influence of strong circum-polar westerlies, föhn winds can develop at the lee (eastern) side of the south-north oriented spine of the AP (Elvidge et al., 2014; King et al., 2017; Kuipers Munneke et al., 2018). During these events, warm and dry air reaches the ice shelf at the foot of the mountains. Turton et al. (2018) and Wiesenekker et al. (2018) show that föhn events at AWS 18 between November 2014 and December 2016 occur 14 % of the time. Even in mid-winter, 2 m air temperatures can reach values as high as  $10^{\circ}\text{C}$ , while relative humidity decreases to values below 50 %.

AWS 14 and 18 are both located on Larsen C ice shelf in the eastern AP (Fig. 4.1). AWS 18 is located in Cabinet Inlet, one of the main contributing ice streams of the Larsen C ice shelf. AWS 14 is located  $\sim 120$  km SE of AWS 18, in the middle of the ice shelf and significantly closer to the ice-shelf edge. The spine of the AP causes the occurrence of frequent föhn events at AWS 18 (see e.g. Kuipers Munneke et al., 2018; Wiesenekker et al., 2018); owing to its location farther from the mountain range, these events are less frequent and less severe at AWS 14 (Turton et al., 2018).

Figures 4.3c–d and 4.4e–h show the SEB and near-surface climate at AWS 14 and 18, for a six-day period in April 2015. This event was chosen because of the short overlap between the two stations' observational record, resulting in this event as one of the few events registered by both stations. During this period, a well-developed and long-lasting föhn event was registered at AWS 18, with air temperatures as high as 8.5°C. Surface melt occurred continuously for 60 h, from ~8 April 10:00 until ~10 April 21:00, with a cumulative melted mass of 37 kg m<sup>-2</sup>. The most important energy source was  $Q_S$ , reaching peak hourly averaged values of 150 W m<sup>-2</sup>, aided by the strong winds (11–12 m s<sup>-1</sup>) and the large temperature gradient between the warm air and the melting surface, which cannot adjust its temperature further upwards. Relative humidity remained as low as 40 %, characteristic of föhn winds, leading to significant sublimation with peak hourly average values of 75 W m<sup>-2</sup>. Without this heat sink, cumulative melt would have been ~44 % higher. At AWS 14, owing to its location farther from the AP spine, the föhn effect is significantly less pronounced, with above-freezing air temperatures occurring only towards the end of the episode and cumulative melt totalling 2 kg m<sup>-2</sup>, 5.4 % of that at AWS 18. At AWS 14, the surface temperature remained below freezing for most of the period, with  $Q_G$  gradually increasing indicating warming of the snowpack by  $Q_S$  and  $LW_{net}$ , resulting in some surface melt in the final hours of the föhn event. This shows that AP föhn events and the associated melt are spatially highly heterogeneous, and tend to peak in intensity and duration at the foot of the AP mountains.

## 4.4 Evaluation of other surface melt products

### 4.4.1 Temperature–index models

Temperature–index models are used where radiation observations are not available. By relating surface melt rates to air temperature, an estimate of the former can be determined solely from temperature observations. Typically, these models relate period-total melt amounts to the period-sum of daily  $T - T_c$  when  $T > T_c$ , where  $T_c$  is a freely chosen threshold

temperature (usually  $T_c = 0^\circ\text{C}$ ) and  $T$  is the daily average air temperature (usually at 2 m) (see e.g. Braithwaite, 1995; Hock, 2003; Van den Broeke et al., 2010a). The proportionality constant between daily average  $T - T_c$  and daily melt amount is the *degree day factor* (DDF), expressed in  $\text{mm d}^{-1} \text{K}^{-1}$ . Commonly used values for DDF are in the range  $3\text{--}8 \text{ mm d}^{-1} \text{K}^{-1}$  (Hock, 2003).

Applying this method to all stations with  $T_c = 0^\circ\text{C}$  yields DDFs between  $3.3 \text{ mm d}^{-1} \text{K}^{-1}$  (AWS 18) and  $55.6 \text{ mm d}^{-1} \text{K}^{-1}$  (AWS 19). The results indicate that DDF is spatially highly variable, with an average value of  $26.6 \text{ mm d}^{-1} \text{K}^{-1}$  for DML stations and  $5.9 \text{ mm d}^{-1} \text{K}^{-1}$  for eastern AP shelf stations. The very high degree day factors for DML are caused by the intermittent nature of the melt, giving rise to frequent melt days for which average daily temperatures do not exceed  $0^\circ\text{C}$  (see also Fig. 4.4).

The variability in the DDF over larger areas was also shown by Van den Broeke et al. (2010a) for the Greenland ice sheet. As  $T$  is the daily average air temperature, melt days on which daily average  $T < 0^\circ\text{C}$  are not recognised as melt days, which results in a significant amount (72.5 % in terms of total melt) of melt events not being accounted for. This effect is most pronounced in DML, where only 7.6 % of the melt days have a daily average  $T > 0^\circ\text{C}$ , compared to 34.7 % on eastern AP ice shelves.

By choosing  $T_c < 0^\circ\text{C}$ , e.g. when  $T_c$  is set to  $-10^\circ\text{C}$  (following Van den Broeke et al., 2010a), all melt events are accounted for; however, the correlation coefficient between predicted and observed daily melt  $R^2$  decreases from 0.36 to 0.33, further lowering the validity of this method. This simple application of the in-situ melt rate dataset shows that continent-wide estimates for surface melt cannot be based solely on temperature records and a positive-degree day method.

#### 4.4.2 RACMO2

We compare the in-situ surface melt rates to the output of the polar version of the Regional Atmospheric Climate Model (version RACMO2.3p2, from now on RACMO2), which is developed at IMAU in collaboration with

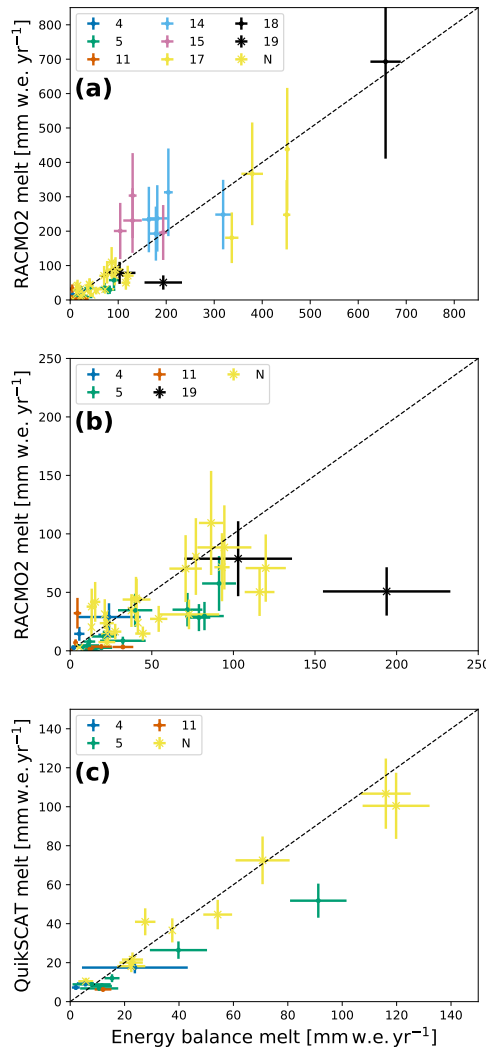


**Figure 4.5** In-situ versus **(a,b)** RACMO2-modelled and **(c)** QuikSCAT-derived yearly (Jul–Jun) melt. AWS are indicated by station numbers and Neumayer by N. **(a)** shows all stations, **(b)** focuses on DML stations for clarity. Correlation coefficients are **(a)** 0.83, **(b)** 0.51 and **(c)** 0.92. The error bars for RACMO2 **(a,b)** and QuikSCAT **(c)** are empirically determined by calculating the relative deviation from each observation and taking the average; this average relative deviation is then imposed on each model point. The errors of the in-situ melt values are derived from a parameter uncertainty study with the SEB model (similar to Jakobs et al., 2019).

the Royal Netherlands Meteorological Institute (KNMI). The model combines the dynamics of the regional model HIRLAM (Undén et al., 2002) with the physics parameterisations of ECMWF-IFS (ECMWF, 2009), assuming hydrostatic balance and using 40 vertical levels. It is interactively coupled to a multilayer snow model that calculates melt, refreezing, percolation and runoff of meltwater (Ettema et al., 2010). It furthermore includes a snow albedo scheme based on snow grain size evolution (Kuipers Munneke et al., 2011b; Van Angelen et al., 2012) as well as a drifting snow scheme that simulates the redistribution and sublimation of suspended snow particles (Lenaerts et al., 2012). We refer the reader to Van Wessem et al. (2014a) and Van Wessem et al. (2014b) for more technical details of RACMO2.

Here we use the latest gridded 27 km product spanning the period 1979–2017 and covering the entire continent (Fig. 4.1). The model run is forced at the lateral boundaries and in the upper atmosphere by the ERA-interim reanalysis product (Dee et al., 2011). Previous studies have evaluated RACMO2 for temperature, wind speed and SEB components in Antarctica; Van Wessem et al. (2018) showed that RACMO2 reproduces surface temperatures and net shortwave radiation with high accuracy ( $R^2 > 0.9$ ), and turbulent fluxes, net longwave radiation and wind speed with fair accuracy ( $R^2 > 0.5$ ). The RACMO2 melt product has not been compared to in-situ melt data but only to QuikSCAT data, which showed a correlation of  $R^2 = 0.81$  and a bias of  $-15 \text{ Gt yr}^{-1}$  for the entire AIS ( $\sim 13\%$  of average annual snowmelt) (Van Wessem et al., 2018). Furthermore, RACMO2 has been evaluated in terms of SEB components (King et al., 2015) and Surface Mass Balance (Kuipers Munneke et al., 2017).

Here, we compare the RACMO2 surface melt rates to the in-situ melt rate dataset (Fig. 4.5). The RACMO2 error bars are empirically determined by calculating the relative deviation from each observation and taking the average; this average relative deviation is then imposed on each model melt point. The errors of the in-situ melt values are derived from a parameter uncertainty study with the SEB model (similar to Jakobs et al., 2019). The result that deviates most from the baseline run is assumed to represent the uncertainty. Figure 4.5 presents annual (Jul–Jun) surface melt rates for **(a)** all stations and **(b)** DML stations only, and shows good

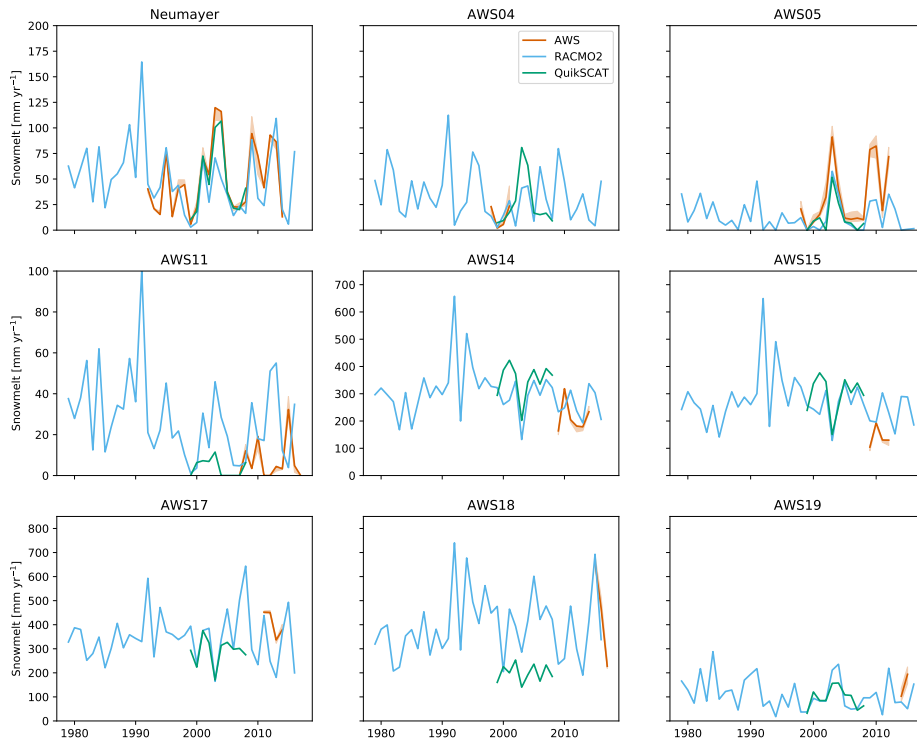


**Figure 4.6** Time series of in-situ melt rate (dark orange), RACMO2 (blue) and QuikSCAT (green). The two in-situ melt values for AWS 19 (bottom right) cover only the summer months Dec–Feb and Nov–Jan respectively, and therefore do not fully capture the melt seasons.

correlation ( $R^2 = 0.83$ ). On average RACMO2 somewhat underestimates melt (bias =  $-7.3 \text{ mm w.e. yr}^{-1}$ ). When both regions are considered separately the correlation weakens, with  $R^2 = 0.59$  for stations located on the ice shelves in the eastern AP, and  $R^2 = 0.51$  for stations in DML.

Figure 4.6 presents time series of annual melt (1979–2017) from QuikSCAT (green), discussed in the next section, RACMO2 (blue) and the in-situ melt rates (dark orange) for the nine observational sites. The shading indicates the uncertainty based on the SEB-model parameter uncertainty tests. The figure shows that surface melt is extremely variable from year to year. We also note that the interannual variability significantly exceeds

the uncertainty of the in-situ melt rate. Although at some locations the difference between the in-situ surface melt and RACMO2 is substantial (e.g. AWS 15), the average annual melt amount and its interannual variability are similar ( $p < 0.01$  in Fig. 4.5a). Elevation differences between the nearest grid point in RACMO2 and the actual station elevation do not explain these differences: performing a linear regression of modelled melt on elevation does not significantly improve the overall result (not shown).

Figure 4.2 compares observed seasonal SEB cycles with RACMO2 (dashed lines). Qualitatively, the modelled seasonal cycles compare well to the observed ones. The lag in  $LW_{\text{net}}$  compared to  $SW_{\text{net}}$  is represented well by the model, as well as average and month-to-month variations in wind speed. As the fluxes are generally small, minor differences in one flux can have large implications for the total SEB. At AWS 14, modelled winter temperatures are  $\sim 4^\circ\text{C}$  higher than observed. As a result, wintertime  $Q_S$  and  $LW_{\downarrow}$  are larger and  $LW_{\uparrow}$  is more negative because of the higher surface temperature. At AWS 5, modelled temperatures are slightly lower than observed. Furthermore, modelled  $SW_{\uparrow}$  is larger in summer, indicating a higher modelled surface albedo. As a result,  $R_{\text{net}}$  is lower throughout the summer season.  $LW_{\uparrow}$  is less negative, indicating a lower surface temperature, which leads to a greater surface-to-air temperature gradient and larger  $Q_S$ . At Neumayer, RACMO2 models higher winter temperatures, leading to larger  $Q_S$  in winter. The modelled surface albedo is higher in summer, as  $SW_{\uparrow}$  is larger. As a result, modelled  $R_{\text{net}}$  is lower in summer, leading to slightly less surface melt. The possibility to perform such detailed SEB comparisons underlines the usefulness of the in-situ SEB and melt data.

### 4.4.3 QuikSCAT

As a final application we present a comparison of our melt dataset with satellite-derived melt amounts. Trusel et al. (2013) present 1999–2009 annual (Jul–Jun) continent-wide maps of cumulative surface melt at 8–10 km effective resolution. It is based on data from the SeaWinds radar scatterometer onboard the QuikSCAT satellite. The detection of liquid

water in the snowpack relies on the high dielectric constant of liquid water compared to snow. As a result, radar backscatter is greatly reduced in the presence of liquid water, which is detectable even at small amounts in the snowpack. The method used by Trusel et al. (2013) calibrates seasonally summed reductions in radar backscatter during melt with in-situ melt products from AWS across Antarctica. AWS 14, 15 and Neumayer are among the stations that were used for the calibration, stations of which the meteorological data are also part of this study.

Figure 4.5c compares annual surface melt rates from QuikSCAT (1999–2009) with the in-situ melt rates. Unfortunately, the overlap in time period available for QuikSCAT and our dataset is limited, resulting in data from only 4 stations available for the comparison. Data from Neumayer are dominating the comparison, which shows a good correlation ( $R^2 = 0.92$ ). Note that since data from Neumayer were used to calibrate QuikSCAT, these results are not independent. If the Neumayer values are omitted from Fig. 4.5c, the correlation coefficient increases ( $R^2 = 0.98$ ) but the slope becomes significantly smaller than one. Figure 4.5c furthermore shows that all in-situ surface melt rates for AWS 4, 5 and 11 are higher than those from QuikSCAT. As melt is intermittent in DML, it is possible that some melt events occur between consecutive passes of the QuikSCAT satellite. As melt amounts are low at AWS 4, 5 and 11, this affects the QuikSCAT signal more strongly at those sites than at Neumayer.

The QuikSCAT surface melt estimates are displayed in green in Fig. 4.6, allowing for a direct comparison with the in-situ and RACMO2 annual melt rates. Unfortunately, there is little temporal overlap between the QuikSCAT data and the in-situ observations. Nevertheless, Fig. 4.6 shows that the interannual variability as observed and as modelled by RACMO2 are similar, adding confidence to the long-term continent-wide melt estimates of RACMO2.

## 4.5 Summary and conclusions

This paper presents a benchmark dataset of consistent, in-situ Antarctic SEB and surface melt rates at five locations in coastal Dronning Maud

Land (DML) and four locations in the eastern Antarctic Peninsula (AP), at high temporal resolution (1–2 h).

Uncertainties in the in-situ surface melt and energy balance calculations are based on SEB model parameter uncertainty (Jakobs et al., 2019). The results show that DML and the eastern AP have very different melt climates. In the relatively cold climate of DML, melt is driven by absorption of solar radiation, with melt occurrence and rate determined by a delicate balance between processes that add (absorption of shortwave radiation) and remove (sublimation) heat from the surface. Melt is more extensive in space and time on the ice shelves in the eastern AP, owing to their more northerly location and frequent föhn events (e.g. Turton et al., 2018; Wiesenekker et al., 2018). These föhn events can lead to continuous melting for multiple days, even outside summer, but our analysis shows that continuous melt is confined to the foot of the AP mountains and does not extend far onto the ice shelf.

Despite the relatively short time series of the in-situ melt rates and SEB, they are powerful tools to calibrate/validate/evaluate other melt products such as temperature–index models, regional climate models and satellite products. We show that temperature index models are unsuitable to estimate melt rates in the intermittent melt climate of coastal Antarctica. On the other hand, seasonal melt rates from the QuikSCAT satellite (Trusel et al., 2013) and the regional climate model RACMO2 (Van Wessem et al., 2018) agree generally well with the in-situ data. Although at some locations surface melt is not reproduced properly by RACMO2, for example at AWS 19 (Fig. 4.5), the correlation with the entire dataset is very high ( $R^2 = 0.83$  in Fig. 4.5a), providing confidence in the performance of these melt products.

These pilot applications demonstrate the value of consistently derived in-situ surface melt and energy balance products from the Antarctic ice sheet, and stress the urgent need for similar observations from other coastal Antarctic sites.



## 5. SMAF in Antarctica

Surface melt is an important process for the stability of ice shelves, and therewith the Antarctic ice sheet. In Antarctica, absorption of solar radiation is mostly the largest energy source for surface melt, which is further enhanced by the snowmelt–albedo feedback (SMAF): refrozen snow has a lower albedo than new snow, which causes it to absorb more solar radiation, further increasing the energy available for surface melt. This feedback has previously been shown to increase surface melt by approximately a factor of 2.5 at Neumayer Station in East Antarctica. In this study, we use a regional climate model to quantify SMAF for the entire Antarctic ice sheet. We find that it is most effective on ice shelves in East Antarctica, and is less important in the Antarctic Peninsula and on the Ross and Filchner-Ronne ice shelves. We identify a relationship between SMAF and average summer air temperatures, and find that SMAF is most important around  $265 \pm 2$  K. On a sub-seasonal scale, we identify several parameters that contribute to SMAF: the length of dry periods, the time between significant snowfall events and snowmelt events, and prevailing temperatures. We then apply the same temperature-dependency of SMAF to the Greenland ice sheet and find that it is potentially active in a narrow band around the ice sheet, and finally discuss how the importance of SMAF could change in a warming climate.

### 5.1 Introduction

The Antarctic ice sheet (AIS) contains approximately 26 million km<sup>3</sup> of ice, equivalent to a global mean sea level change of 58 m (Morlighem et al.,

---

This Chapter is published as “Spatial variability of the snowmelt–albedo feedback in Antarctica”, *Journal of Geophysical Research: Earth Surface*, 2021, doi:10.1029/2020JF005696.

2020). In recent years, accelerated mass loss from the AIS has been observed; Shepherd et al. (2018) report a mass loss rate of  $109 \pm 56 \text{ Gt yr}^{-1}$  over the period 1992–2017. The highest mass loss is observed in West Antarctica, as a result of the thinning and disappearing of ice shelves, the floating extensions of the grounded ice sheet. Ice shelves are present along  $\sim 74\%$  of the AIS (Bindshadler et al., 2011), buttressing the grounded ice sheet. They experience basal melt through ocean–ice heat exchange (Pritchard et al., 2012; Massom et al., 2018), as well as surface melt by energy exchange at the ice-shelf surface (Van den Broeke, 2005; Kingslake et al., 2017).

The recent collapse of Larsen A and B ice shelves on the east side of the Antarctic Peninsula (AP) was preceded by extensive surface melt, inducing hydrofracturing (Van den Broeke, 2005; Glasser and Scambos, 2008). On the west side of the AP, break-up events on Wilkins ice shelf have been associated with increased basal melt rates, leading to changes in buoyant forces (Braun et al., 2009; Padman et al., 2012). Ice-shelf thinning and break-up have both been associated with the acceleration of its feeding glaciers (Scambos et al., 2004; Rott et al., 2011), causing the high mass loss rates in coastal West Antarctica and the AP (Wouters et al., 2015; Turner et al., 2017). Ice-shelf stability is thus crucial for the future mass balance of the AIS. Because both basal and surface melt are expected to increase in a warming climate also for the more southerly ice shelves (Trusel et al., 2015), a proper representation of ice-shelf melt processes is essential in climate modeling.

In this paper we focus on surface melt processes. Weather stations, satellites and climate models have been used to estimate surface melt rates on Antarctic ice shelves (Bromwich et al., 2013; Trusel et al., 2015; Van Kampenhout et al., 2017; Van Wessem et al., 2018; Agosta et al., 2019; Souverijns et al., 2019). In-situ observations show that in the cold climate of Antarctica, insolation is usually the most important energy source for surface melt (Van den Broeke et al., 2005a; Jonsell et al., 2012; King et al., 2015; Jakobs et al., 2020). The absorption of solar radiation is in turn enhanced by the snowmelt–albedo feedback (SMAF) (Jakobs et al., 2019): when snow melts, meltwater percolates into the subsurface snow layers where it can refreeze. As refrozen snow consists of larger snow grains than

new snow, it reduces the backward scattering of photons (Wiscombe and Warren, 1980), i.e. it has a lower albedo. As a result, the surface absorbs more incoming solar radiation, leading to more surface melt, representing a positive feedback. Therefore, it is crucial for climate models to use a snow albedo parameterisation that includes this melt–albedo feedback (Cullather et al., 2014; Van Dalum et al., 2019; Alexander et al., 2019).

In a previous study, we used high-quality meteorological observations from Neumayer Station, located on Ekström ice shelf in East Antarctica, to quantify the effect of SMAF on surface melt rates (Jakobs et al., 2019). We used a surface energy balance (SEB) model that includes a grain-size-dependent albedo parameterisation, and found that on average, SMAF enhanced surface melt (1992–2016) at Neumayer Station by a factor of 2.5, but with significant interannual variability. The current study aims to extend our previous work to the entire AIS, using the regional climate model RACMO2. This climate model is specifically developed to simulate polar climates and has been extensively evaluated (Van Wessem et al., 2018; Jakobs et al., 2020). Its albedo parameterisation makes it well-suited to study SMAF at the continental scale.

In the next section, we introduce the climate model RACMO2 and describe the albedo parameterisation used. In Section 5.3 we present a map of SMAF in Antarctica (Section 5.3.1), discussing its spatial variability as well as the interannual variability at different locations (Section 5.3.2). We identify regions in Antarctica that are most affected by SMAF (Section 5.4.1) and present local case studies on a daily timescale to identify conditions where SMAF is largest (Section 5.4.2). In Section 5.4.3, we comment on the potential importance of SMAF in Greenland, and how SMAF will affect surface melt in the future on both ice sheets, followed by conclusions in Section 5.5.

## 5.2 Methods

### 5.2.1 Model descriptions

The regional climate model RACMO2 is developed by the Royal Netherlands Meteorological Institute (KNMI). It is a hydrostatic model that combines the dynamics of the High Resolution Limited Area Model (HIRLAM,

Undén et al. (2002)) with the physics parameterisations of the Integrated Forecast System (IFS, version CY33r1) of the European Centre for Medium-Range Weather Forecast (ECMWF) (ECMWF, 2009).

For this study, we use the latest polar version (RACMO2.3p2, from now on referred to as RACMO2), which has been specifically developed for use over glaciated regions (Reijmer et al., 2005; Van Wessem et al., 2018). The atmosphere is represented by 40 vertical levels and the model is forced by the ERA-Interim reanalysis product at its lateral boundaries as well as in the upper atmosphere (Van de Berg and Medley, 2016). The atmospheric component is coupled to a multilayer snow model (Ettema et al., 2010), which allows for meltwater percolation, refreezing and runoff. Furthermore, RACMO2 uses an albedo parameterisation in which the albedo depends on snow grain size (Gardner and Sharp, 2010; Kuipers Munneke et al., 2011b) and a drifting-snow scheme that simulates horizontal transport of snow by near-surface winds (Lenaerts et al., 2012).

Van Wessem et al. (2018) compared the output of RACMO2 with in-situ measurements of surface temperature, radiation fluxes, turbulent fluxes and wind speed. They found that RACMO2 yields reliable estimates of surface temperatures and net short-wave radiation ( $R^2 > 0.9$ ), and performs adequately in modeling turbulent fluxes, net long-wave radiation and wind speed ( $R^2 > 0.5$ ). They furthermore found a good correlation ( $R^2 = 0.81$ ) of surface melt rates with the results from the QuikSCAT satellite. Jakobs et al. (2020) showed that RACMO2 reproduces surface melt rates with reasonable accuracy: compared to in-situ melt estimates from (automatic) weather stations in the AP and Dronning Maud Land, RACMO2 slightly underestimates surface melt rates (bias=-7.3 mm w.e. yr<sup>-1</sup>) but overall, the agreement is good ( $R^2 > 0.8$ ).

RACMO2 solves the surface energy balance (SEB) equation, which describes the energy exchange between the surface, the sub-surface and the atmosphere and determines the amount of energy available for surface melt:

$$M = R_{\text{net}} + Q_S + Q_L + Q_G, \quad (5.1)$$

where  $R_{\text{net}}$  is net radiation, the sum of net short-wave and net long-wave radiation,  $Q_S$  and  $Q_L$  are the turbulent fluxes of sensible and latent heat,

respectively, and  $Q_G$  is the surface value of the subsurface heat flux.  $M$  is the energy available for surface melt, which is equal to 0 when the surface temperature is below the melting point of ice (273.15 K). In an iterative procedure, the surface temperature is determined so that the SEB is closed. If this temperature would exceed 273.15 K, it is forced to this value and excess energy is available for surface melt.

The turbulent fluxes  $Q_S$  and  $Q_L$  are determined using Monin-Obukhov similarity theory, which relates the fluxes to the near-surface gradients of wind speed, potential temperature and humidity (see e.g. Van den Broeke et al. (2005b)). The subsurface heat flux  $Q_G = k \frac{\partial T}{\partial z}$ , where  $k$  is the effective thermal conductivity of the snow/ice and  $\frac{\partial T}{\partial z}$  the temperature gradient in the near-surface snowpack. The snow model solves the heat-conductivity equation to obtain the subsurface temperature profile and therewith  $Q_G$  (Ettema et al., 2010):

$$\rho c_p \frac{\partial T}{\partial t} = - \frac{\partial}{\partial z} \left( k \frac{\partial T}{\partial z} \right) + q_{\text{refr}}, \quad (5.2)$$

where  $q_{\text{refr}}$  is the energy released by the refreezing of meltwater per unit time per area. Penetration of short-wave radiation is not considered in this version of RACMO2.

This version of RACMO2 uses the albedo parameterisation of Gardner and Sharp (2010), in which the albedo is described as a base value  $\alpha_S$  with modifications due the solar zenith angle  $\theta$  ( $d\alpha_u$ ), the cloud optical thickness  $\tau$  ( $d\alpha_\tau$ ) and the concentration of black carbon in the snow ( $d\alpha_c$ ). The impact of snow impurities is assumed negligible for Antarctica and thus  $d\alpha_c = 0$  (Warren and Clarke, 1990; Grenfell et al., 1994; Bisiaux et al., 2012; Marquetto et al., 2020)).

The base albedo  $\alpha_S$  is given by (Gardner and Sharp, 2010):

$$\alpha_S = 1.48 - 1.27048 r_e^{0.07}, \quad (5.3)$$

where  $r_e$  is the snow grain size, in turn parameterised as

$$r_e(t) = [r_e(t-1) + dr_{e,\text{dry}} + dr_{e,\text{wet}}] f_o + r_{e,0} f_n + r_{e,r} f_r, \quad (5.4)$$

where  $dr_{e,dry}$  and  $dr_{e,wet}$  describe grain growth due to dry and wet snow metamorphism, respectively.  $r_{e,0}$  and  $r_{e,r}$  denote the grain sizes of new and refrozen snow, set to constant values of  $r_{e,0} = 54$  mm (Kuipers Munneke et al., 2011b) and  $r_{e,r} = 1000$  mm (Van Wessem et al., 2018).  $f_o$ ,  $f_n$  and  $f_r$  are the fractions of old, new and refrozen snow. Equations for  $d\alpha_u$ ,  $d\alpha_\tau$ ,  $dr_{e,dry}$  and  $dr_{e,wet}$  can be found in Gardner and Sharp (2010).

Gardner and Sharp (2010) consider the effect of the second snow layer by changing the modification due to black carbon concentration ( $d\alpha_c$ ):

$$d\alpha'_c = (\alpha_c^{btm} - \alpha_s^{top}) + A (\alpha_c^{top} - \alpha_c^{btm}), \quad (5.5)$$

where top and btm indicate the top and bottom layers respectively, and  $A$  is a factor dependent on  $\alpha_s^{top}$  and the top-layer thickness  $z$ . However, as we set  $c = 0$ , the second layer is not taken into account. This approach is different from Kuipers Munneke et al. (2011b) and Jakobs et al. (2019), who used more than two layers to calculate the surface albedo, irrespective of the value of  $c$ .

## 5.2.2 Quantifying SMAF

To quantify the effect of SMAF in Antarctica, we performed two simulations with RACMO2 at 27 km horizontal resolution for the period 1979–2018: a baseline run  $R_0$  in which the full albedo parameterisation is used as described above, and a sensitivity run  $R_1$ , in which the contribution of refrozen snow to snow grain size, and hence surface albedo, is disabled by setting  $f_r = 0$  in Eq. (5.4). The same approach was used by Jakobs et al. (2019) to quantify SMAF at Neumayer Station in East Antarctica. The term ‘period-average’ is used throughout this article, referring to the period 1979–2018.

There are several ways to quantify SMAF. The most robust definition is  $SMAF_t$ , the ratio of the total (‘t’) cumulative amounts of surface melt in  $R_0$  and  $R_1$  over the entire period available (in this study 1979–2018). We use this measure to interpret the spatial variability of SMAF and e.g. its correlation with period-average temperature. SMAF can also be determined on a seasonal (‘s’) basis, i.e. the ratio of seasonal (in this study Jul–Jun) melt in  $R_0$  and  $R_1$ , and is denoted by  $SMAF_s$ . Time series of  $SMAF_s$  are used to study the interannual variability of SMAF and the connection to the SEB.

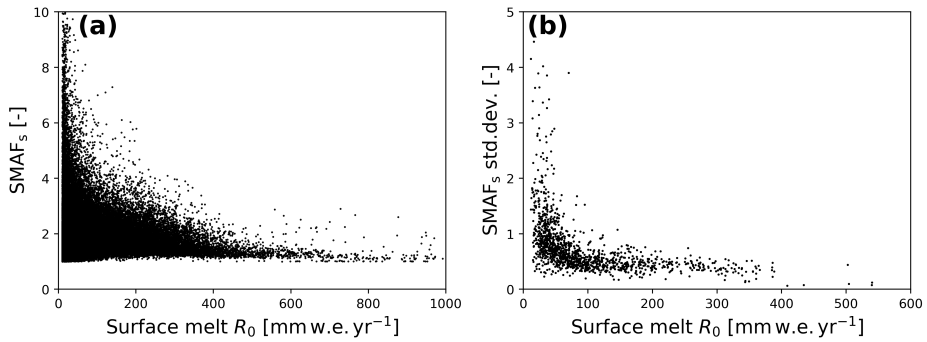


**Figure 5.1 (a)** Relationship between surface melt rate and  $\text{SMAF}_s$ . Each dot represents one season with at least 10 mm w.e. for all grid points within the model domain. **(b)** Period-average seasonal surface melt versus  $\text{SMAF}_s$  standard deviation for all grid points with period-average seasonal surface melt  $\geq 5$  mm w.e.

## 5.3 Results

### 5.3.1 Spatial distribution of SMAF

Since SMAF is defined as the ratio of surface melt in two different runs, we first present the relation between seasonal surface melt rates and  $\text{SMAF}_s$  in Fig. 5.1a, for seasons with at least 10 mm w.e. of surface melt, for each model grid cell. The figure shows that the highest  $\text{SMAF}_s$  values occur in low-melt regions, while in high-melt regions  $\text{SMAF}_s$  is close to 1. It furthermore shows that melt is not the only driver of  $\text{SMAF}_s$ . In this section we study the spatial distribution of SMAF and surface melt; in Sect. 5.4 we then discuss possible other drivers of SMAF.

To identify the regions where SMAF is most important, we first need to know the spatial distribution of surface melt in Antarctica. This is presented in Fig. 5.2a, with the highest values occurring on both sides of the AP, locally exceeding  $300 \text{ mm w.e. yr}^{-1}$ . Extreme values ( $>500 \text{ mm w.e. yr}^{-1}$ ) occur on small islands north of the AP. The highest surface melt rates in East Antarctica are found on Shackleton ice shelf (indicated in Fig. 5.2c with an ‘S’), due to its northerly location. The lowest values are

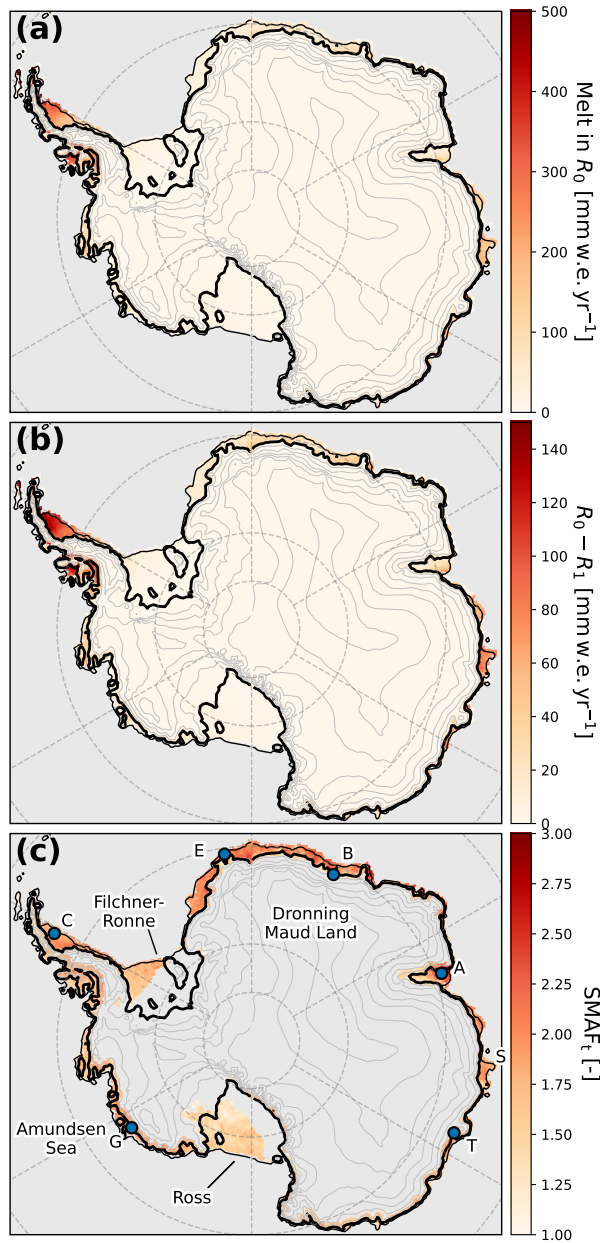
found on the Ross and Filchner-Ronne ice shelves. The absolute increase in seasonal average melt because of SMAF ( $R_0 - R_1$ ) is shown in Fig. 5.2b. A pattern similar to Fig. 5.2a emerges, with the highest values in the AP and on Shackleton ice shelf, but also in coastal Dronning Maud Land and the Amundsen Sea sector.

Figure 5.2c shows the resulting  $\text{SMAF}_t$ , ranging from 1 to  $\sim 2.8$ , for locations with at least 5 mm w.e. of period-average seasonal surface melt. The highest values are found in coastal Dronning Maud Land and the Amundsen Sea sector; these locations have relatively low seasonal surface melt rates, combined with an increase because of SMAF that is relatively large. Lower values are found in low-melt regions such as on the Ross and Filchner-Ronne ice shelves, and high-melt regions such as the northern AP. These patterns are discussed in more detail in Sect. 5.4.1, but first we consider the temporal variability of  $\text{SMAF}_s$ .

### 5.3.2 Temporal variability of SMAF

For six locations, indicated by blue dots in Fig. 5.2c, time series of seasonal snow melt for both runs ( $R_0$  and  $R_1$ ) are presented in Fig. 5.3. The ratio between these two yields the seasonal  $\text{SMAF}_s$  value; indicated in top-right are  $\text{SMAF}_t$  and the average and standard deviation of  $\text{SMAF}_s$ . The average of  $\text{SMAF}_s$  is greater than  $\text{SMAF}_t$ ; this is a result of the lower limit of  $\text{SMAF}_s$ , which is by definition 1. Especially in low-melt regions, summers with high  $\text{SMAF}_s$  have a larger effect on its average than on  $\text{SMAF}_t$ .

These locations were selected to illustrate the different SMAF regimes. On Larsen C ice shelf (Fig. 5.3f), SMAF leads to an increase in surface melt by a relatively constant factor every year, characterised by a low standard deviation of  $\text{SMAF}_s$ . This is different from e.g. Amery ice shelf (Fig. 5.3c), where  $\text{SMAF}_s$  varies strongly from year to year (high standard deviation of  $\text{SMAF}_s$ ). For the other locations, the standard deviation ranges between these extremes. Note that Larsen C and King Baudouin ice shelves have significant melt events outside of the summer months, because of regular Föhn events (Lenaerts et al., 2017; Wiesennecker et al., 2018). These are however not sensitive to SMAF, as they are not driven by short-wave radiation but rather by turbulent heat fluxes.



**Figure 5.2** (a) Period-average seasonal surface melt rates modelled by RACMO2, with the full albedo parameterisation (run  $R_0$ ). (b) Difference in average seasonal surface melt rates between runs  $R_0$  and  $R_1$ . (c)  $\text{SMAF}_t$  for all grid points with period-average seasonal surface melt  $\geq 5$  mm w.e. Blue dots indicate sites for which Fig. 5.3 presents time series of surface melt: Ekström (E), King Baudouin (B), Amery (A), Totten (T), Getz (G) and Larsen C (C) ice shelves. Shackleton ice shelf is indicated with an S.

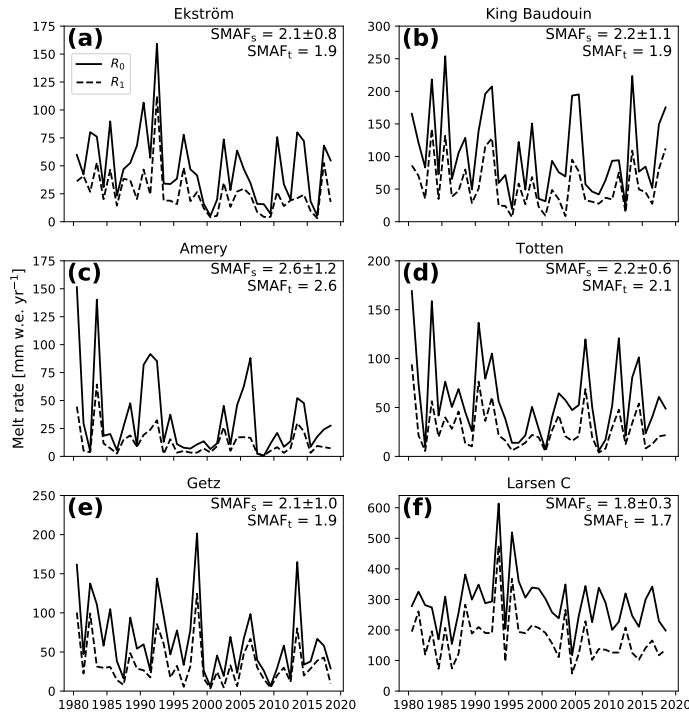


**Figure 5.3** Time series of seasonal surface melt rates at various ice shelves around the Antarctic ice sheet (see Fig. 5.2c). Melt in  $R_0$  is indicated with a solid line, in  $R_1$  with a dashed line; the ratio between the two gives the seasonal  $\text{SMAF}_s$  value. Numbers in the top right corner are  $\text{SMAF}_t$ , the average of  $\text{SMAF}_s$  and its standard deviation.

Figure 5.1b shows a decrease of  $\text{SMAF}_s$  interannual variability with increasing melt. In low-melt regions ( $< 100 \text{ mm w.e. yr}^{-1}$ ), melt is highly intermittent and the albedo remains generally high. If melt occurs, the albedo decreases significantly and surface melt increases relatively strongly, yielding large  $\text{SMAF}_s$  values. In contrast, high-melt regions have a lower surface albedo to start with due to the higher prevailing temperatures; the albedo-lowering effect of melt is therefore less influential and melt is only slightly enhanced, leading to low  $\text{SMAF}_s$  values and variability.

Figures 5.1 and 5.2 present the relationship between surface melt and

SMAF. However, these figures also suggest there are more drivers determining SMAF. These are the subject of Sect. 5.4.1, where we identify climatic regions where SMAF is most active. Section 5.4.2 focusses on how SMAF is related to the SEB on a daily timescale, for different regimes.

## 5.4 Discussion

### 5.4.1 Climatic drivers of SMAF

To understand the spatial patterns in Fig. 5.2c, we investigated the relationship between  $\text{SMAF}_t$  and several quantities: summer (Nov–Feb) air temperature, summer precipitation and seasonal surface melt rate. The most discernible pattern is observed in the correlation with temperature, which is therefore used below to describe large-scale climate drivers of  $\text{SMAF}_t$ . Precipitation and surface melt are used to discuss SMAF on a sub-seasonal scale in Sect. 5.4.2.

Figure 5.4 presents the relation between  $\text{SMAF}_t$  and mean summer air temperature. It shows that the highest  $\text{SMAF}_t$  values are found in regions with an average summer air temperature of  $\sim 265$  K (defined as  $T_c$ ), where  $\text{SMAF}_t$  reaches an average value of 1.9. This pattern is not very sensitive to the chosen period; it is similar if the time period is limited to an arbitrary 10-year or 20-year period throughout the total period (not shown). Its shape suggests a ‘peak bandwidth’ rather than a single peak value. Therefore, in the following we consider a 2 K bandwidth around  $T_c$ , i.e.  $T_c = 265 \pm 2$  K.

In regions with temperatures above or below  $T_c$ ,  $\text{SMAF}_t$  gradually decreases to 1. In the colder regions ( $T < 263$  K), surface melt rates are generally low (mostly  $< 30$  mm w.e.  $\text{yr}^{-1}$ ) and SMAF only moderately enhances surface melt ( $\sim 40$ – $50\%$ ). In warmer regions ( $T > 267$  K), such as the AP, SMAF is also less important for surface melt; due to the relatively mild conditions, the contribution of turbulent heat fluxes is more important to melt energy than absorption of short-wave radiation. This causes melt events that are less affected by the surface albedo, limiting the influence of SMAF. This is discussed in more detail in Sect. 5.4.2.

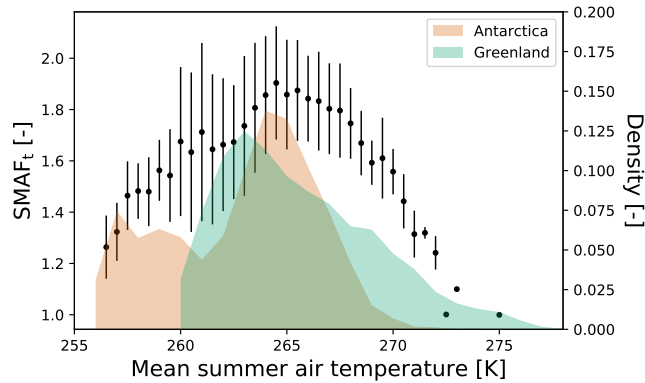


**Figure 5.4**  $\text{SMAF}_t$  as a function of binned (0.5 K) Nov–Feb average air temperature for all grid points with period-average seasonal surface melt of at least 5 mm w.e. (black dots, lines indicate the standard deviation; the three rightmost dots have no lines because there is only 1 data point within the temperature bin). **Right axis** The shading indicates the normalised distribution of average summer air temperature for all grid points with period-average seasonal surface melt of at least 5 mm w.e. in Antarctica (orange, Nov–Feb) and in Greenland (green, accumulation zone only, May–Aug).

Figure 5.5 shows the spatial distribution of the deviation of average summer air temperature from  $T_c$  in Antarctica (Fig. 5.5a) and Greenland (Fig. 5.5b, discussed in Sect. 5.4.3). The Ross, Filchner-Ronne and Amery ice shelves extend far to the south and are the coldest areas which experience surface melt in Antarctica, with average summer air temperatures of 260 K and lower. These ice shelves represent the left tail of the temperature– $\text{SMAF}_t$  relation (Fig. 5.4), where SMAF has a limited effect on surface melt rates. The AP is the warmest region of Antarctica, with average summer air temperatures of 270 K and higher. It is located in the right tail of the temperature– $\text{SMAF}_t$  relation, where surface melt is semi-continuous, mainly driven by high air temperatures, and SMAF is also of limited importance for surface melt rates.

The remaining, smaller ice shelves in East and West Antarctica experience average summer air temperatures around  $T_c$ , displayed in white in Fig. 5.5a, with the 2 K bandwidth indicated with red contours. This indi-

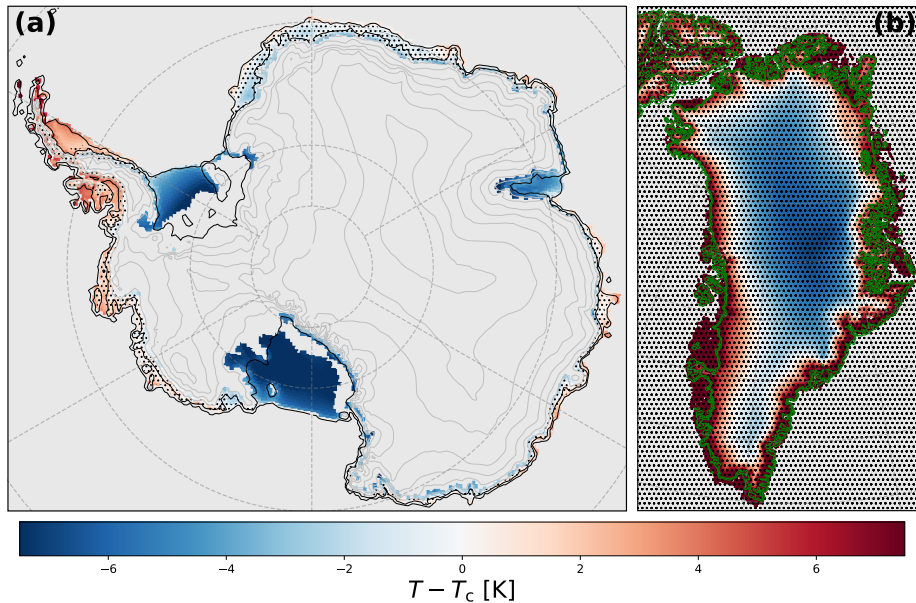


**Figure 5.5** Temperature deviation from  $T_c \equiv 265$  K, the temperature at which SMAF plateaus (see Fig. 5.4), for Antarctica **(a)** and Greenland **(b)**. Blue areas indicate regions where SMAF will become increasingly important when air temperatures rise. White areas indicate regions where SMAF is now enhancing surface melt the most. Red areas indicate regions where air temperatures / melt are too high for an optimal SMAF. Black dots indicate the 2 K bandwidth around  $T_c$ , the green contour in **(b)** indicates the ice-sheet margin.

cates that SMAF is currently significantly ( $\sim$ doubling) enhancing surface melt on ice shelves all around the AIS. In this high-SMAF regime, surface melt is an intermittent process; the meteorological circumstances that favor SMAF are identified in the next section.

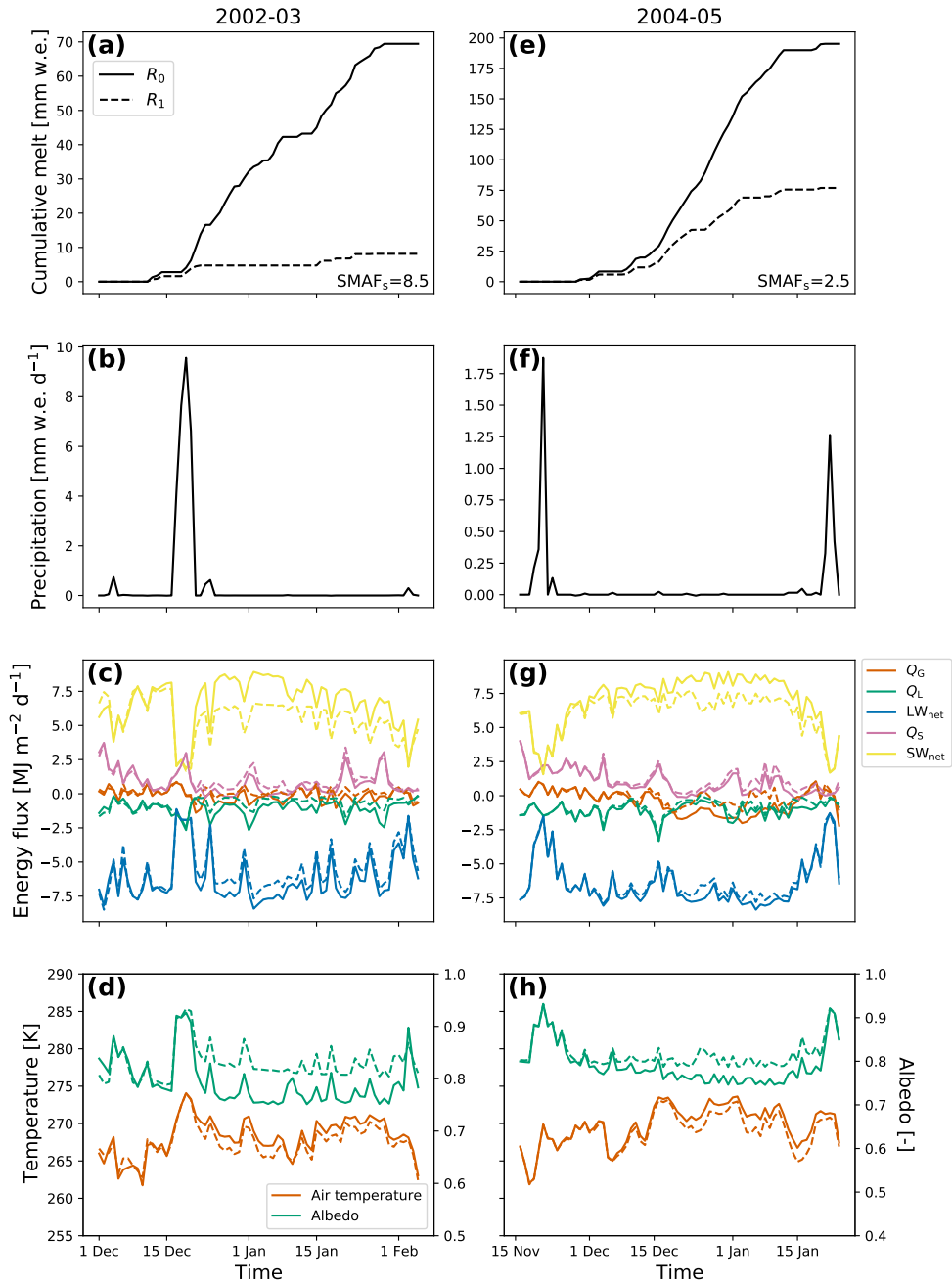
#### 5.4.2 SMAF and its connection to the SEB

To investigate SMAF and its drivers more closely, we compare summers with different SMAF values at four locations: King Baudouin ice shelf, Ross ice shelf, Larsen C ice shelf and Amery ice shelf (see Fig. 5.2c for

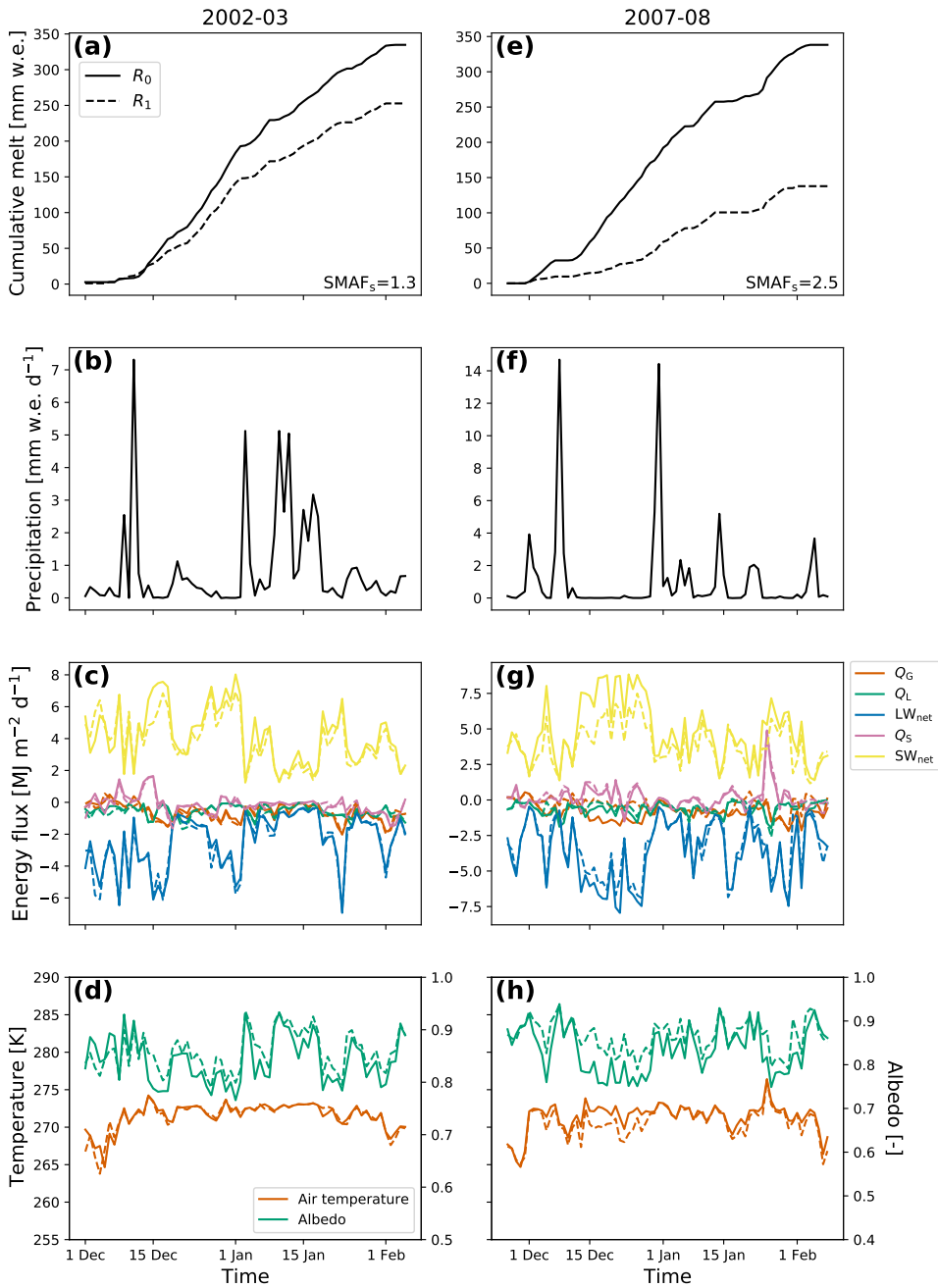
locations). These locations were selected because they represent different SMAF regimes: moderate temperature, strong SMAF (King Baudouin, Fig. 5.6), high temperature, weak SMAF (Larsen C, Fig. 5.7), low temperature, weak SMAF (Ross, Fig. 5.8), and low temperature, strong SMAF (Amery, Fig. 5.9).

Figure 5.6 shows melt-season time series for a location on King Baudouin ice shelf, located in coastal Dronning Maud Land, (indicated by ‘B’ in Fig. 5.2c) in a moderate-temperature, strong-SMAF region (Fig. 5.5a). Figure 5.3b has shown that in this location,  $SMAF_s$  experiences a large inter-annual variability. Figure 5.6 shows daily cumulative surface melt (**a,e**), precipitation (**b,f**), the surface energy balance components (SEB, **c,g**) and temperature and albedo (**d,h**) for experiments  $R_0$  and  $R_1$  (see Sect. 5.2.2). In the melt season 2002–03, around 15 Dec, a melt episode occurs immediately after a strong precipitation event (Fig. 5.6a and b). Because of refreezing, the albedo drops from 0.9 to  $\sim 0.75$  (Fig. 5.6d). As no more significant snowfall events follow, the albedo remains low for the remainder of the season, resulting in significantly elevated  $SW_{net}$  values (Fig. 5.6c) and a prolonged period of surface melt in  $R_0$ . The surface albedo is not reset to that of new snow until the end of the melt season. As grain growth by refreezing is inactive in  $R_1$ , the decrease in albedo after the melt event is smaller; it stabilises at  $\sim 0.82$ . As the surface now reflects more solar radiation,  $SW_{net}$  is significantly lower and melt ceases after the first melt event following the precipitation event. In  $R_0$  melt totalled  $\sim 70$  mm w.e. during this season, while in  $R_1$  it totalled only 8 mm w.e., yielding a high  $SMAF_s$  value of 8.5 (Fig. 5.6a).

At the same location but two seasons later (2004–05), a similar dry period occurred (Fig. 5.6e-h). Contrary to 2002–03, melt did not start immediately after the last significant snowfall event. Rather, the albedo decreases steadily because of dry snow metamorphism in both  $R_0$  and  $R_1$ . Before the first melt of the season, the albedo had decreased to  $\sim 0.82$  in both runs. Similar to 2002–03, the albedo decreases more in  $R_0$  than in  $R_1$  during the melt event. However the effect of SMAF is now less pronounced than in 2002–03 because the albedo was already lowered, making the additional contribution of refrozen snow less important. The difference in  $SW_{net}$  is therefore also smaller, as well as the difference in surface melt



**Figure 5.6** Time series of daily totals of (a,e) surface melt, (b,f) precipitation, (c,g) fluxes of surface energy balance components, and (d,h) average temperature and surface albedo, during the summer of 2002–03 (a–d) and 2004–05 (e–h) at King Baudouin ice shelf, Dronning Maud Land, East Antarctica (see Fig. 5.2c, indicated by B). In all panels solid lines indicate  $R_0$  and dashed lines indicate  $R_1$ .

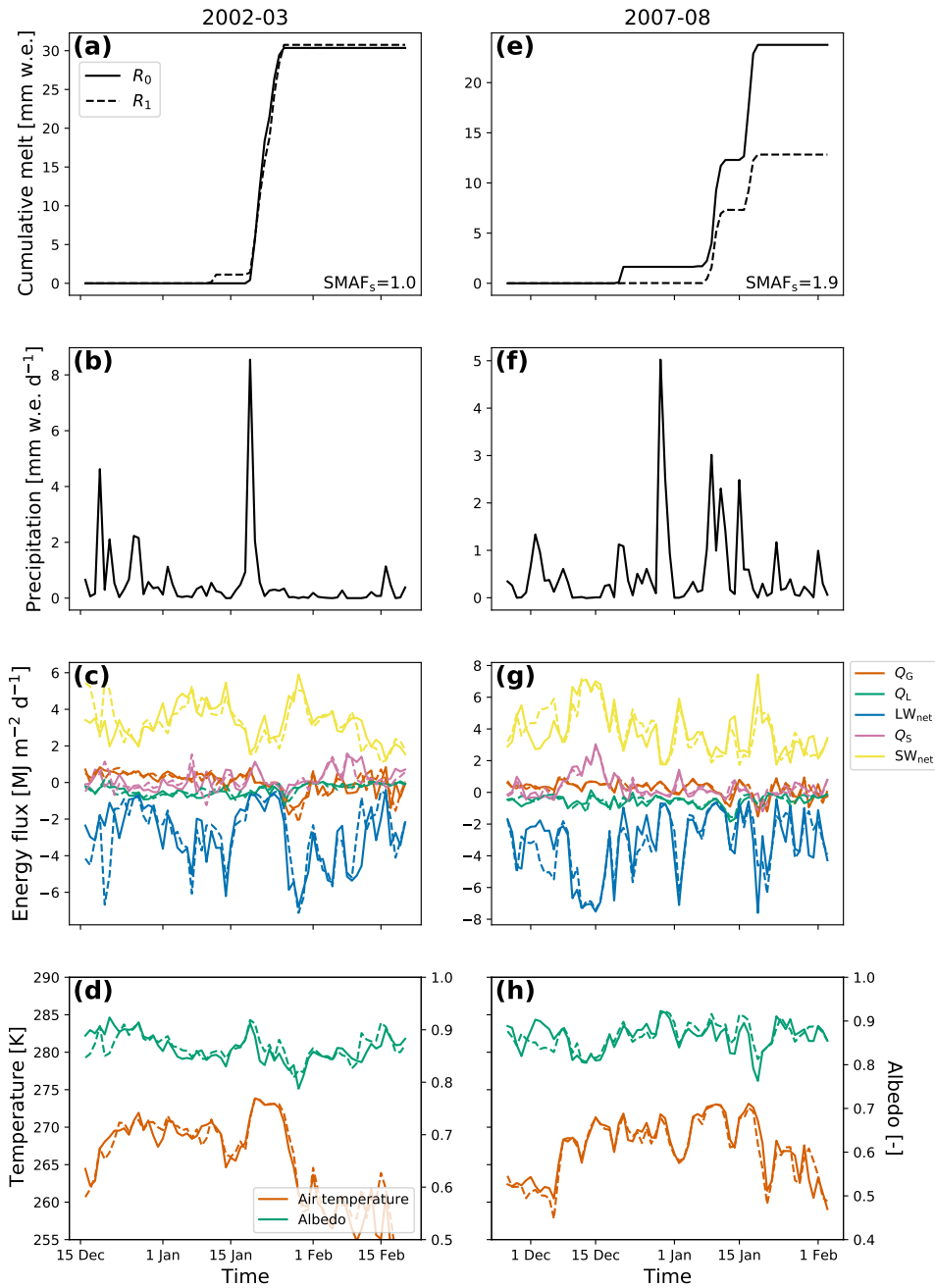


**Figure 5.7** Same as Fig. 5.6 for Larsen C ice shelf, Antarctic Peninsula (see Fig. 5.2c, indicated by C).

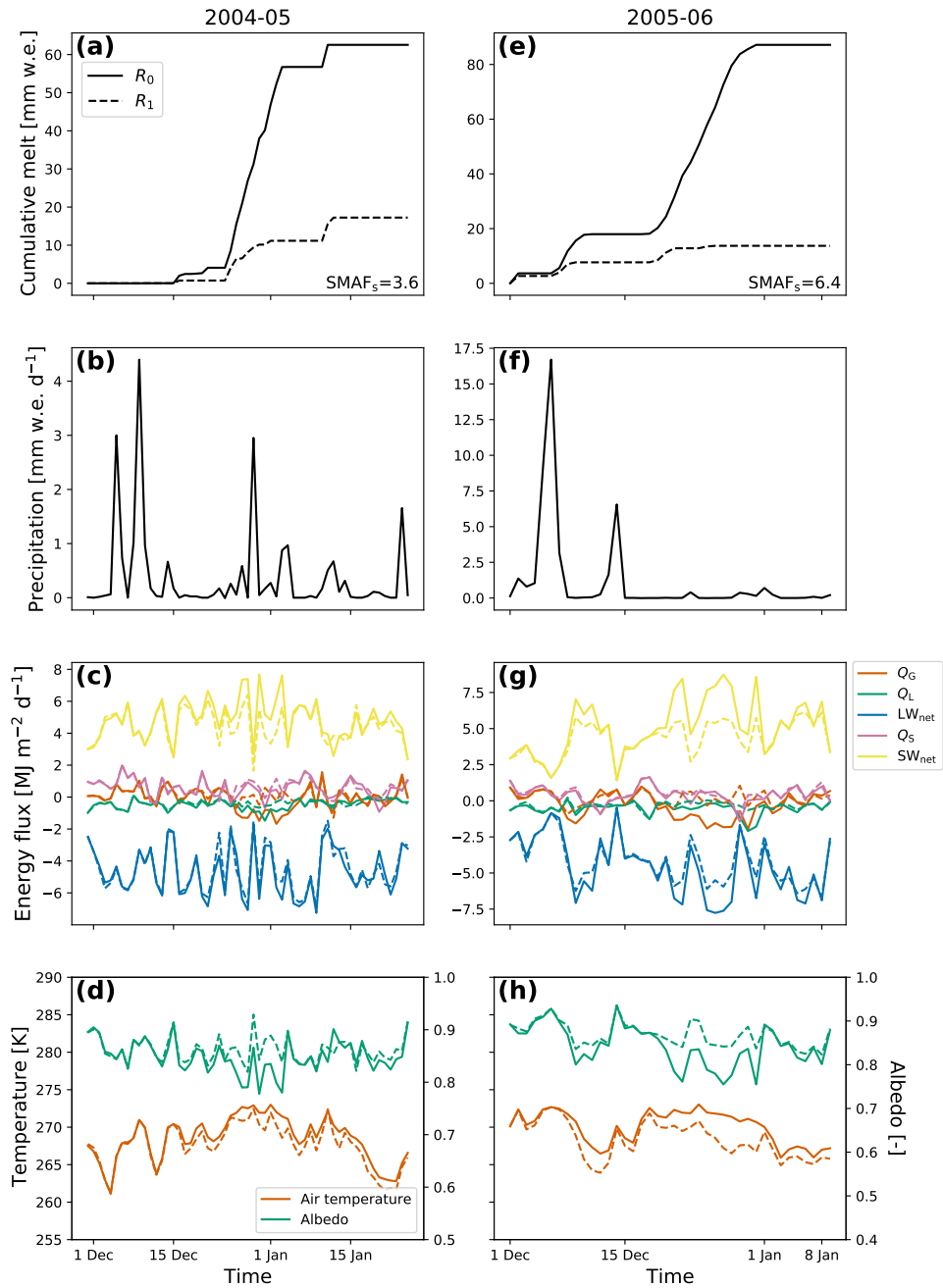
rates throughout the season. The total 2004–05 surface melt amounts are  $\sim 200$  mm w.e. in  $R_0$  and  $\sim 80$  mm w.e. in  $R_1$ , giving a  $\text{SMAF}_s$  of 2.5 (Fig. 5.6e).

Figure 5.7 shows results for a location on Larsen C ice shelf in the AP (indicated by ‘C’ in Fig. 5.2c), a region that experiences relatively high surface melt rates and higher temperatures than King Baudouin ice shelf, due to its more northerly location. Melt is enhanced by SMAF most efficiently between 15 Dec 2007 and 1 Jan 2008, during a prolonged dry period (Fig. 5.7e and f). The subsequent difference in albedo (Fig. 5.7h) resulted in significantly more absorption of solar radiation during this period (Fig. 5.7g) while temperatures were high enough to sustain surface melt. The absence of such a dry period in 2002–03 prevented SMAF from affecting surface melt as efficiently. Furthermore, the air temperature is close to the melting point throughout the season, which allowed sustained surface melt in both  $R_0$  and  $R_1$  runs. In the end, SMAF enhanced surface melt by only  $\sim 30\%$  compared to  $\sim 140\%$  in 2007–08, which again underlines the importance of dry periods for the effectiveness of SMAF. The effect is considerably smaller than on King Baudouin ice shelf (Fig. 5.6) because of the higher temperature on Larsen C, which allows for surface melt to proceed even in the absence of SMAF ( $R_1$ ). This also explains the smaller interannual variability that is observed in Fig. 5.3f.

Figure 5.8 shows results for a location on Ross ice shelf, the largest ice shelf in Antarctica (see Fig. 5.2c). Due to its southerly location, temperatures are significantly lower than on King Baudouin ice shelf and, therefore, melt is more intermittent and less extensive. Although in 2007–08 (Fig. 5.8e–h) the air temperature occasionally reaches the melting point, sustained melt does not occur. Melt is limited to short melt events during which SMAF is unable to enhance surface melt over a longer period. However, because melt energies are so low, small absolute melt differences still induce a significant  $\text{SMAF}_s$  value for this season. In another year (2002–03), there was one significant melt event without any melt enhancement because of SMAF (Fig. 5.8a). Figure 5.8c shows that during the melt event, both  $\text{SW}_{\text{net}}$  and  $\text{LW}_{\text{net}}$  are approaching zero, indicating heavily overcast conditions. Melt energy is for an important part provided by  $Q_s$ , which is insensitive to surface albedo. As a result, SMAF did not enhance surface melt during this event.



**Figure 5.8** Same as Fig. 5.6 for Ross ice shelf (see Fig. 5.2c).



**Figure 5.9** Same as Fig. 5.6 for Amery ice shelf, Dronning Maud Land (see Fig. 5.2c, indicated by A).

Figure 5.9 shows daily melt, precipitation, SEB, temperature and albedo for a location on Amery ice shelf, East Antarctica (indicated by ‘A’ in Fig. 5.2c), which experiences relatively low average temperatures for its latitude. The first season (panels a–d) represents the high-SMAF summer 2004–05 without a prolonged dry period; even the precipitation event on 30 Dec was not able to sufficiently reset the surface albedo. During this event, melt continued because of the persistent high temperature and with its high  $Q_S$ . As a result the new snow was quickly removed from the surface. The difference in  $SW_{\text{net}}$  in the following days is sufficient to cause high  $SMAF_s$ . In the summer of 2005–06 (panels e–h) an even higher  $SMAF_s$  occurs, resulting from a long dry episode. A remarkably large difference in air temperature is observed (Fig. 5.9h) during the persistent melt episode in  $R_0$  which is absent in  $R_1$ . This is caused by persistently higher surface temperatures, following larger  $SW_{\text{net}}$  and refreezing.

These examples show the different meteorological circumstances that can lead to different SMAF values. The moderate-temperature regions have the highest  $SMAF_t$  values, because SMAF causes the albedo to be lowered sufficiently such that enhanced absorption of solar radiation causes continuous melt, which is absent in  $R_1$ . In warm regions, even in cases when the albedo is higher, melt continues in  $R_1$  (see Fig. 5.7d). Finally, in cold regions, sustained melt does not occur because of the low temperatures. Melt is limited to single-day melt events instead, rendering SMAF unable to enhance surface melt for a prolonged period, resulting in small  $SMAF_s$  and  $SMAF_t$  values.

These examples illustrate that especially prolonged dry periods in temperate summer climates enable SMAF to greatly enhance summer melt amounts, due to the lack of snowfall resetting the surface albedo. Quantifying the correlation between dry periods and  $SMAF_s$  remains difficult. The exact timing of precipitation and early melt events is equally important: when dry snow metamorphism has already lowered the surface albedo before surface melt starts, SMAF is strongly reduced.

We conclude that, in order to properly simulate the Antarctic melt climate, a climate model must accurately represent surface albedo, precipitation timing and intensity, and air and snow temperature.

### 5.4.3 Outlook: Greenland and the future

The shaded areas in Fig. 5.4 indicate the normalised distributions of temperature for all grid points with period-average seasonal surface melt of at least 1 mm w.e. in Antarctica (orange) and in Greenland (green, accumulation zone only). The Ross, Filchner-Ronne and Amery ice shelves correspond to the left peak of this distribution, where the impact of SMAF on surface melt rates is limited (Sect. 5.4.1). The right peak of this temperature distribution represents the remaining ice shelves along East and West Antarctica. The higher temperatures are a result of their more northerly location than the Ross, Filchner-Ronne and Amery ice shelves. This shows that in the current climate, the majority of melt points fall in a regime with moderate SMAF, with only few locations significantly above  $T_c$ .

In a warmer climate, the distributions in Fig. 5.4 will shift towards the right. The East Antarctic ice shelves, located in the right peak of the orange distribution, will slowly become less affected by SMAF. On the other hand, the Ross, Filchner-Ronne and Amery ice shelves, which are in the left peak of this distribution, will gradually be exposed to higher SMAF values. As SMAF will become more important on these ice shelves, surface melt will increase relatively more strongly in these regions than for example on coastal Dronning Maud Land ice shelves. This might negatively affect the stability of the ice shelves through processes such as increased firn saturation, increased ice temperatures and hydrofracturing, and therewith affects the future of the AIS (Trusel et al., 2015).

The temperature distribution of melt points in Greenland is shown in green shading in Fig. 5.4 (accumulation zone only). The absence of large, flat ice shelves results in large differences with the distribution of Antarctica. The bulk of the Greenland distribution is centered around 260 K, which represents the high and flat interior accumulation zone. Figure 5.10 shows the melt–temperature relation for Antarctica and Greenland (accumulation zone only), relating the period-average summer melt and summer temperature (Nov–Feb for Antarctica, May–Aug for Greenland). The Greenland curve seems to be an extension of the Antarctica curve, suggesting that when temperatures increase in the southern hemisphere, the Antarctic melt climate will increasingly resemble the contemporary Greenland melt climate. Note also that the temperature–SMAF relationship

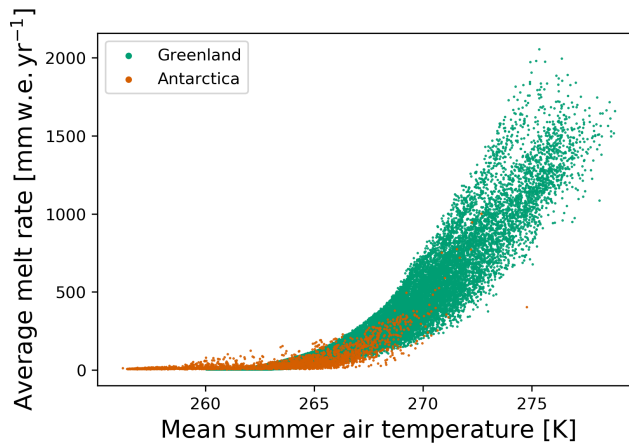


**Figure 5.10** Period-average summer air temperature versus average seasonal surface melt for Greenland (green, accumulation zone only) and Antarctica (orange) for all grid points with period-average seasonal surface melt of at least 5 mm w.e. Summer is defined as Nov–Feb in Antarctica and May–Aug in Greenland.

(Fig. 5.4) is not very sensitive to the time period for which it is calculated (not shown). This suggests that this relationship might also be applicable to Greenland. In order to assess how SMAF might affect surface melt in Greenland, we therefore apply the temperature–SMAF relationship to the Greenland temperature distribution.

Figure 5.5b shows the temperature deviation from  $T_c$  for Greenland. Similar to Fig. 5.5a, white areas indicate the regions where SMAF is currently most optimal for enhancing surface melt, red areas are too warm for a strong SMAF, and blue areas are currently too cold. In the current climate and based on our results from the AIS, it shows that SMAF is active in a large part of the interior ice sheet in southern Greenland, and a narrow band in the middle-elevated accumulation zone around the rest of the ice sheet. In a warming climate, the SMAF region will migrate inland, corresponding to a right-ward shift of the green temperature distribution in Fig. 5.4. This leads to a rapid increase of the area being affected by SMAF when air temperatures over Greenland continue to rise.

## 5.5 Conclusions

In this study we investigate the spatial and temporal variability of the snowmelt–albedo feedback (SMAF) on the Antarctic ice sheet (AIS). This is done by performing two simulations with the regional atmospheric climate model RACMO2, covering the period 1979–2018. This model uses a parameterisation that relates the surface albedo to the grain size of snow; by disabling the contribution of refrozen snow to albedo lowering, this allows us to explicitly model the effect of SMAF on surface melt. One simulation is performed with the full albedo parameterisation ( $R_0$ ), in the other simulation this refrozen-snow contribution is disabled ( $R_1$ ). Following Jakobs et al. (2019), we define SMAF as the ratio of cumulative surface melt between these two simulations, a value of 1 indicating no effect, a value of  $X$  indicating that melt is enhanced  $X$ -fold because of SMAF.

We find that SMAF is spatially highly variable on the AIS, ranging from values close to 1 in cold, low-melt regions such as the Ross and Filchner-Ronne ice shelves, to values up to 3 in coastal Dronning Maud Land (Fig. 5.2). Relating  $\text{SMAF}_t$  to average summer (Nov–Feb) air temperature reveals a maximum around 265 K ( $T_c$ , Fig. 5.4). Many Antarctic ice shelves are located in the temperature regime where SMAF is currently optimal, except for the three largest ice shelves (Ross, Filchner-Ronne and Amery), which are too cold, and the entire Antarctic Peninsula (Fig. 5.5a), which is too warm.

Investigating the link between SMAF and the surface energy balance reveals that the timing of significant snowfall events with respect to surface melt is important. Seasonal SMAF is highest when melt occurs immediately after the last snowfall event at the onset of the melt season and in the absence of significant precipitation throughout the remainder of the season. The reason is that in this case the surface albedo is not reset to the new-snow value and enhanced melt occurs continuously. When snowfall is not immediately followed by surface melt, the surface albedo is lowered by dry snow metamorphism. The effect of refrozen snow on seasonal albedo is subsequently much smaller than in the previous example, and therefore SMAF is less important.

In cold regions such as the Ross ice shelf, the air temperature is generally too low to accommodate continuous surface melt. When surface melt occurs, it is mostly constrained to a single melt day; as a result, SMAF is not able to significantly enhance surface melt. On Larsen C ice shelf, located in the mild AP, the air temperature is normally high enough to facilitate near-continuous surface melt; SMAF does enhance surface melt but it does not determine whether surface melt continues or ceases. This is contrary to moderate-temperature locations, where SMAF can be the determining factor for the start and continuation of surface melt.

Although a large part of Antarctica is currently too cold for an optimal SMAF, which occurs at  $\sim 265$  K, rising temperatures in the future could expose even the largest ice shelves to a strong increase in surface melt because of SMAF. Applying the same threshold to the Greenland ice sheet shows that a large part of southern Greenland is in the SMAF-sensitive temperature regime (Fig. 5.5b), indicating that SMAF is an important driver for surface melt in that area.

## 6. Conclusions and outlook

### 6.1 Conclusions

The aim of this thesis is to quantify the importance of the snowmelt–albedo feedback (SMAF) for melt at the surface of the Antarctic ice sheet (AIS). This positive feedback occurs when meltwater refreezes in the near-surface snow layers. This causes the albedo to drop, allowing the surface to absorb more energy, which further enhances surface melt (Fig. 6.1). Surface melt is important for the stability of ice shelves, which buttress the grounded ice sheet, slowing down its flow into the ocean. Properly understanding SMAF and its effect on surface melt is necessary to further the development of the simulation of surface melt processes in climate models.

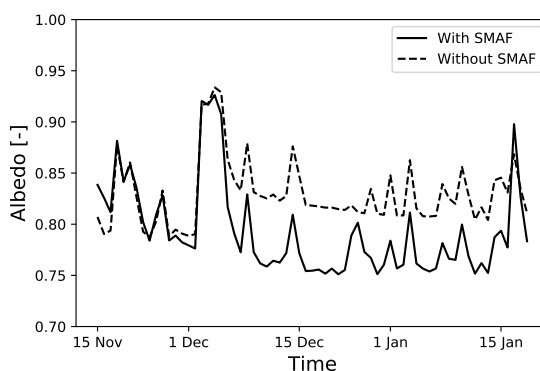


**Figure 6.1** Surface albedo in RACMO2 during the 2002–03 melt season on King Baudouin ice shelf in East Antarctica. The solid line represents a simulation in which SMAF is active, the dashed line represents a simulation in which it is disabled.

We first quantified SMAF on a local scale, using meteorological observations from Neumayer Station in East Antarctica (Chapter 3). This station

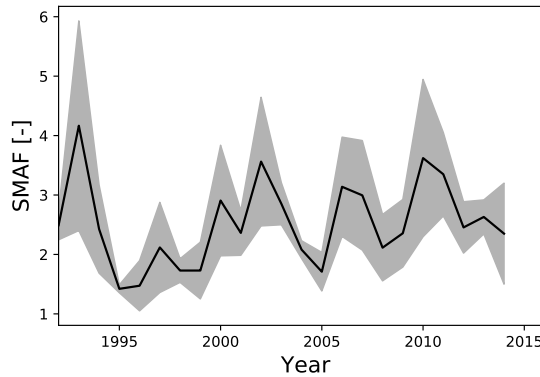


**Figure 6.2** Temporal variability of SMAF at Neumayer.

was chosen because it is the only station on the AIS with long-term accurate radiation observations, which are necessary for robust surface melt calculations. These data were used to force a Surface Energy Balance (SEB) model, in order to calculate surface melt rates. The SEB model predicts an average seasonal melt rate of  $50 \text{ mm w.e. yr}^{-1}$  at Neumayer, with considerable interannual variability. This variability is mainly driven by differences in absorbed solar radiation, which hints that SMAF plays an important role in the surface melt process.

To test this, we expanded the SEB model with an albedo parameterisation based on snow grain size. Next, we define SMAF as the ratio between surface melt rates obtained from two simulations: one that includes the feedback mechanism, and one in which it is disabled. We found that SMAF enhances surface melt at Neumayer by a factor of 2.6, but also exhibits significant interannual variability (Fig. 6.2).

As an intermediate step towards producing a map of SMAF over the entire AIS, we evaluated surface melt rates in the regional atmospheric climate model RACMO2 (Chapter 4). Using meteorological observations from nine automatic weather stations in Antarctica in combination with the data from Neumayer, we used the same SEB model to calculate surface melt rates for these ten locations on or close to Antarctic ice shelves. We

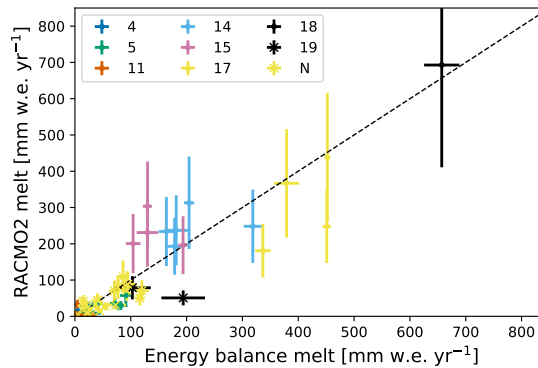


**Figure 6.3** Comparison of in-situ melt rates and RACMO2-modelled melt rates.

identified two types of surface melt events: radiation-driven and turbulence-driven. Turbulence-driven melt events mostly occur in the Antarctic Peninsula (AP), where the local topography causes Föhn winds. These transport warm, dry air onto the eastern AP ice shelves, enhancing turbulence-driven melt. On the other hand, radiation-driven melt events are most common on ice shelves in East Antarctica. On these ice shelves, temperatures are relatively low and solar radiation is the main driver of surface melt.

Using these data, we found that RACMO2 adequately reproduces the Antarctic melt climate (Fig. 6.3). Although on average RACMO2 slightly underestimates surface melt rates, the interannual variability is reproduced accurately. A comparison with the melt product of the QuikSCAT satellite provides further confidence in the surface melt rates modelled by RACMO2.

In Chapter 5, the spatial variability of SMAF in Antarctica was determined by performing two simulations with the regional climate model RACMO2 at 27 km resolution for the period 1979–2018. We found that SMAF is largest on East Antarctic ice shelves, where it enhances surface melt rates typically by a factor of 2.5 (Fig. 6.4). In the AP and on the Ross, Filchner-Ronne and Amery ice shelves, SMAF plays a smaller role. We found a relationship between SMAF and average summer air temperature, which shows that SMAF peaks at  $265 \pm 2$  K.

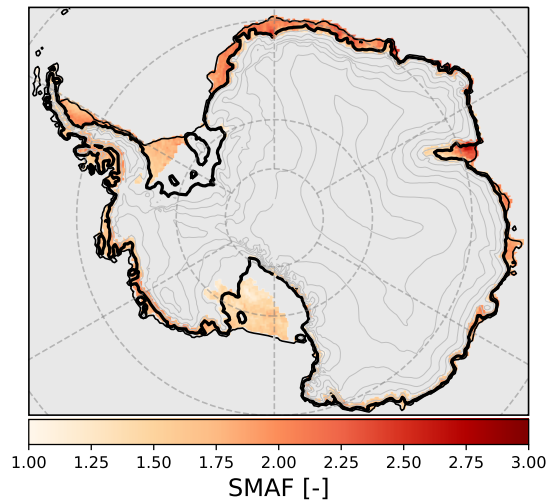


**Figure 6.4** Spatial variability of period-average (1979–2018) SMAF in Antarctica, modelled by RACMO2 at 27 km horizontal resolution.

To further increase our understanding of SMAF, we investigated climatic drivers of SMAF and the SEB on a sub-seasonal timescale for four locations. We found that SMAF is sensitive to the occurrence of dry periods during the summer season, the time between the last significant snowfall event and the onset of the melt season, and the average prevailing temperatures. During dry periods, the feedback is not interrupted by snowfall events that reset the surface albedo, causing relatively high SMAF values for that season. If snowfall is immediately followed by surface melt, the high albedo of the fresh snow layer is quickly lowered by SMAF, again causing a high SMAF value. In a warm summer, surface melt is also driven by turbulent fluxes and long-wave radiation rather than the absorption of solar radiation. As these fluxes are largely independent of surface albedo, SMAF is smaller at such locations.

In this thesis, we provide the first robust estimates of SMAF in Antarctica, and its spatial and temporal variability. As SMAF is capable of enhancing surface melt by a factor of 3, a proper representation of snow albedo in climate models is necessary to obtain realistic surface melt estimates.

Moreover, because of the dependency of SMAF on the sub-surface snow-pack, precipitation and temperature, a climate model should also have proper representations of these processes and variables. Although currently SMAF is largest on the most northerly located East Antarctic ice shelves, there are indicators that SMAF will become a significant factor on the largest, more southerly Antarctic ice shelves (Ross and Filchner-Ronne) when the climate continues to warm. Finally, we briefly discussed the current impact of SMAF on surface melt on the Greenland ice sheet.

## 6.2 Outlook

### 6.2.1 Antarctica's future climate and Greenland

For the first time, SMAF has been estimated in time and space over the Antarctic ice sheet. The most obvious next step is to carry out a similar experiment for Greenland. The Greenland ice sheet (GrIS) does not have large ice shelves, but in contrast to the AIS, the main contributor to ice-sheet mass loss is meltwater being transported away from the ice sheet. Thus, surface snowmelt already has a direct influence on current ice sheet mass loss. A dedicated Greenland simulation can tell us which locations are most affected by SMAF, and subsequently which areas are most sensitive to an increase of surface melt. Furthermore, a SMAF–temperature relationship can be established from a dedicated Greenland simulation, which can either confirm or reject the assumption made in Sect. 5.4.3 that the same SMAF–temperature relationship holds for both Greenland and Antarctica, and potentially other glaciated regions such as Svalbard or the Canadian Arctic.

We also assumed in Sect. 5.4.3 that the temperature–SMAF relationship holds in a warmer climate. The observed relationship showed no change when calculated for separate 10- and 20-year intervals, but also no significant temperature increase has been observed in those years in Antarctica (Fig. 1.3). A dedicated RACMO2 simulation into the future can shed light on this assumption as well. It can furthermore reveal whether some parts of Antarctica are especially susceptible to atmospheric warming, which could lead to other regions becoming vulnerable to SMAF than highlighted in Chapter 5.

## 6.2.2 RACMO2 improvements

From the sub-seasonal case studies in Sect. 5.4.2, we learned that SMAF is partly dependent on precipitation timing and the duration of dry periods. Van Wessem et al. (2018) point out that the cloud scheme and the parameterisation of precipitation in RACMO2 still require further development. Currently, precipitation is assumed to reach the surface in the same time step and grid column where it is formed. This assumption is acceptable when using a model at a low resolution, because in that case most precipitation will not be transported out of the grid box within the time step. However, when the climate model is run at a higher spatial resolution, the fraction of precipitation that is transported out of the grid box before it reaches the surface, will also increase. An update of RACMO2 to incorporate the physics parameterisations from a later version of the ECMWF Integrated Forecast System is currently underway. This update includes a prognostic precipitation scheme, in which snow is tracked over multiple grid boxes before it reaches the surface. A more sophisticated precipitation scheme could also improve the snowfall rates in RACMO2: the model is known to favour frequent small snowfall events over less-frequent, larger events (Van de Berg, 2020, personal communication).

In order to properly model SMAF, the near-surface snow layers must be represented well in the model. The tipping-bucket scheme for meltwater percolation, used in both RACMO2 and the SEB model, is a reasonable approximation when studying large-scale processes. However, SMAF depends on near-surface grain-size evolution, which is sensitive to water percolation and refreezing, and it is unknown how sensitive the obtained SMAF estimates are to the choice of these parameterisations. One could for example use a more sophisticated snow model such as SNOWPACK (Steger et al., 2017), or implement a more physical parameterisation of meltwater percolation (Van de Berg, 2020, personal communication).

Furthermore, during experiments carried out for Chapter 3, we noticed that radiation penetration can be an important process for the grain size evolution. However, RACMO2 currently does not consider radiation penetration. Van Dalum et al. (2019) introduced a new spectral snow albedo scheme that includes radiation penetration and a more sophisticated grain-size evolution model. This upgrade has been shown to improve the albedo product of RACMO2 in Greenland (Van Dalum et al., 2020).

### 6.2.3 Towards a non-hydrostatic climate model on an adaptive grid

Because of the ever-increasing computational power of high-performance computing facilities, it is becoming more feasible to run climate models at a higher resolution. However, when using model grids finer than 5 km, new physical limitations come into play. The most apparent of these is the hydrostatic approximation, in which vertical accelerations are neglected. As mentioned in Sect. 2.4, this is usually a reasonable approximation at low resolutions, but at higher resolutions, vertical accelerations can no longer be neglected. If higher resolutions are deemed necessary in climate modelling of the AIS, a transition to a non-hydrostatic model such as HCLIM becomes inevitable (Mottram et al., 2017).

The geography of the AIS however does not require a high resolution for the entire ice sheet. The centre of the ice sheet is relatively flat, and the added benefit of high-resolution modelling probably does not outweigh the costs of increased computational time. This can be mitigated by not employing the same grid over the entire domain, but rather an adaptive grid. In locations where important topographical features are poorly resolved, the horizontal resolution can be increased, while in the flat ice-sheet interior, a lower resolution can be maintained.



# Bibliography

- Agosta, C., C. Amory, C. Kittel, A. Orsi, V. Favier et al. “Estimation of the Antarctic surface mass balance using the regional climate model MAR (1979-2015) and identification of dominant processes.” *The Cryosphere*, 13:281–296, 2019. doi:10.5194/tc-13-281-2019.
- Alexander, P. M., A. N. LeGrande, E. Fischer, M. Tedesco, X. Fettweis et al. “Simulated Greenland Surface Mass Balance in the GISS ModelE2 GCM: Role of the Ice Sheet Surface.” *Journal of Geophysical Research: Earth Surface*, 124:750–765, 2019. doi:10.1029/2018JF004772.
- Amory, C., H. Gallée, F. Naaim-Bouvet, V. Favier, E. Vignon et al. “Seasonal Variations in Drag Coefficient over a Sastrugi-Covered Snowfield in Coastal East Antarctica.” *Boundary-Layer Meteorology*, 164:107–133, 2017. doi:10.1007/s10546-017-0242-5.
- Anderson, P. S. “A Method for Rescaling Humidity Sensors at Temperatures Well below Freezing.” *Journal of Atmospheric and Oceanic Technology*, 11:1388–1391, 1994. doi:10.1175/1520-0426(1994)011<1388:AMFRHS>2.0.CO;2.
- Andreas, E. L. “A theory for the scalar roughness and the scalar transfer coefficients over snow and sea ice.” *Boundary-Layer Meteorology*, 38:159–184, 1987. doi:10.1007/BF00121562.
- Arthern, R. J., D. G. Vaughan, A. M. Rankin, R. Mulvaney, and E. R. Thomas. “In situ measurements of Antarctic snow compaction compared with predictions of models.” *Journal of Geophysical Research*, 115(F03011), 2010. doi:10.1029/2009JF001306.
- Banwell, A. F., D. R. MacAyeal, and O. V. Sergienko. “Breakup of the Larsen B Ice Shelf triggered by chain reaction drainage of supraglacial lakes.” *Geophysical Research Letters*, 40:5872–5876, 2013. doi:10.1002/2013GL057694.
- Barrand, N. E., D. G. Vaughan, N. Steiner, M. Tedesco, P. Kuipers Munneke et al. “Trends in Antarctic Peninsula surface melting conditions from observations and regional climate modeling.” *Journal of Geophysical Research: Earth Surface*, 118:315–330, 2013. doi:10.1029/2012JF002559.
- Bassis, J. N. and C. C. Walker. “Upper and lower limits on the stability of calving glaciers from the yield strength envelope of ice.” *Proceedings of the Royal Society A*, 468:913–931, 2012. doi:10.1098/rspa.2011.0422.

- Bell, R. E., A. F. Banwell, L. D. Trusel, and J. Kingslake. "Antarctic surface hydrology and impacts on ice-sheet mass balance." *Nature Climate Change*, 8:1044–1052, 2018. doi:10.1038/s41558-018-0326-3.
- Bell, R. E., W. Chu, J. Kingslake, I. Das, M. Tedesco et al. "Antarctic ice shelf potentially stabilized by export of meltwater in surface river." *Nature*, 544:344–348, 2017. doi:10.1038/nature22048.
- Bindschadler, R., H. Choi, A. Wichlacz, R. Bingham, J. Bohlander et al. "Getting around Antarctica: new high-resolution mappings of the grounded and freely-floating boundaries of the Antarctic ice sheet created for the International Polar Year." *The Cryosphere*, 5:569–588, 2011. doi:10.5194/tc-5-569-2011.
- Bintanja, R. "The local surface energy balance of the Ecology Glacier, King George Island, Antarctica: measurements and modelling." *Antarctic Science*, 3:315–325, 1995. doi:10.1017/S0954102095000435.
- Bintanja, R. "Surface heat budget of Antarctic snow and blue ice: Interpretation of spatial and temporal variability." *Journal of Geophysical Research*, 105(D19):24387–24407, 2000. doi:10.1029/2000JD900356.
- Bisiaux, M. M., R. Edwards, J. R. McConnell, M. A. J. Curran, T. D. Van Ommen et al. "Changes in black carbon deposition to Antarctica from two high-resolution ice core records, 1850–2000 AD." *Atmospheric Chemistry and Physics*, 12:4107–4115, 2012. doi:10.5194/acp-12-4107-2012.
- Box, J. E., X. Fettweis, J. C. Stroeve, M. Tedesco, D. K. Hall et al. "Greenland ice sheet albedo feedback: thermodynamics and atmospheric drivers." *The Cryosphere*, 6:821–839, 2012. doi:10.5194/tc-6-821-2012.
- Braithwaite, R. J. "Positive degree-day factors for ablation on the Greenland ice sheet studied by energy-balance modelling." *Journal of Glaciology*, 41(137):153–160, 1995. doi:10.3189/S0022143000017846.
- Brandt, R. E. and S. G. Warren. "Solar-heating rates and temperature profiles in Antarctic snow and ice." *Journal of Glaciology*, 39(131):99–110, 1993. doi:10.3189/S0022143000015756.
- Braun, M., A. Humbert, and A. Moll. "Changes of Wilkins Ice Shelf over the past 15 years and inferences on its stability." *The Cryosphere*, 3:41–56, 2009. doi:10.5194/tc-3-41-2009.
- Bromwich, D. H. "Satellite Analysis of Antarctic Katabatic Wind Behavior." *Bulletin of the American Meteorological Society*, 70(7):738–749, 1989. doi:10.1175/1520-0477(1989)070<\$<0738:SAOAKW\$>\$2.o.CO;2.

- Bromwich, D. H., J. P. Nicolas, A. J. Monaghan, M. A. Lazzara, L. M. Keller et al. “Central West Antarctica among the most rapidly warming regions on Earth.” *Nature Geoscience*, 7:139–145, 2012. doi:10.1038/ngeo1671.
- Bromwich, D. H., F. O. Otieno, K. M. Hines, K. W. Manning, and E. Shilo. “Comprehensive evaluation of polar weather research and forecasting model performance in the Antarctic.” *Journal of Geophysical Research: Atmospheres*, 118:274–292, 2013. doi:10.1029/2012JD018139.
- Brun, E., E. Martin, V. Simon, C. Gendre, and C. Coléou. “An Energy and Mass Model of Snow Cover Suitable for Operational Avalanche Forecasting.” *Journal of Glaciology*, 35(121):333–342, 1989. doi:10.3189/S0022143000009254.
- Cape, M. R., M. Vernet, P. Skvarca, S. Marinsek, T. A. Scambos et al. “Foehn winds link climate-driven warming to ice shelf evolution in Antarctica.” *Journal of Geophysical Research: Atmospheres*, 120:11037–11057, 2015. doi:10.1002/2015JD023465.
- Cazenave, A. and B. e. a. W. G. S. L. B. G. Meyssignac. “Global sea-level budget 1993–present.” *Earth System Science Data*, 10:1551–1590, 2018. doi:10.5194/essd-10-1551-2018.
- Clem, K. R., R. L. Fogt, J. Turner, B. R. Lintner, G. J. Marshall et al. “Record warming at the South Pole during the past three decades.” *Nature Climate Change*, 2020. doi:10.1038/s41558-020-0815-z.
- Coléou, C. and B. Lesaffre. “Irreducible water saturation in snow: experimental results in a cold laboratory.” *Annals of Glaciology*, 26:64–68, 1998. doi:10.1017/S0260305500014579.
- Cook, A. J., P. R. Holland, M. P. Meredith, T. Murray, A. Luckman et al. “Ocean forcing of glacier retreat in the western Antarctic Peninsula.” *Science*, 353(6296):283–286, 2016. doi:10.1126/science.aae0017.
- Cook, A. J. and D. G. Vaughan. “Overview of areal changes of the ice shelves on the Antarctic Peninsula over the past 50 years.” *The Cryosphere*, 4:77–98, 2010. doi:10.5194/tc-4-77-2010.
- Cullather, R. I., S. M. J. Nowicki, B. Zhao, and M. J. Suarez. “Evaluation of the Surface Representation of the Greenland Ice Sheet in a General Circulation Model.” *Journal of Climate*, 27:4835–4856, 2014. doi:10.1175/JCLI-D-13-00635.1.
- DeConto, R. M. and D. Pollard. “Contribution of Antarctica to past and future sea-level rise.” *Nature*, 531:591–597, 2016. doi:10.1038/nature17145.
- Dee, D. P., S. M. Uppala, A. J. Simmons, P. Berrisford, P. Poli et al. “The ERA-Interim Reanalysis: Configuration and Performance of the Data Assimilation System.” *Quarterly Journal of the Royal Meteorological Society*, 137(656):553–597, 2011. doi:10.1002/qj.828.

- Denby, B. and W. Greuell. "The use of bulk and profile methods for determining surface heat fluxes in the presence of glacier winds." *Journal of Glaciology*, 46(154):445–452, 2000. doi:10.3189/172756500781833124.
- Donat-Magnin, M., N. Jourdain, H. Gallée, C. Amory, C. Kittel et al. "Interannual Variability of Summer Surface Mass Balance and Surface Melting in the Amundsen Sector, West Antarctica." *The Cryosphere Discussions*, 2019. doi:10.5194/tc-2019-109.
- Dyer, A. J. "A review of flux-profile relationships." *Boundary-Layer Meteorology*, 7:363–372, 1974. doi:10.1007/BF00240838.
- ECMWF. *Part IV: Physical Processes*. Number 4 in IFS Documentation. ECMWF, 2009. Accessed 25 May 2020.
- Edwards, T. L., M. A. Brandon, G. Durand, N. R. Edwards, N. R. Golledge et al. "Revisiting Antarctic ice loss due to marine ice-cliff instability." *Nature*, 566:58–64, 2019. doi:10.1038/s41586-019-0901-4.
- Elvidge, A. D., I. A. Renfrew, J. C. King, A. Orr, T. A. Lachlan-Cope et al. "Foehn jets over the Larsen C Ice Shelf, Antarctica." *Quarterly Journal of the Royal Meteorological Society*, 141:698–713, 2014. doi:10.1002/qj.2382.
- Ettema, J., M. R. Van den Broeke, E. Van Meijgaard, W. J. Van de Berg, J. L. Bamber et al. "Higher surface mass balance of the Greenland ice sheet revealed by high-resolution climate modeling." *Geophysical Research Letters*, 36(L12501), 2009. doi:10.1029/2009GL038110.
- Ettema, J., M. R. Van den Broeke, E. Van Meijgaard, W. J. Van de Berg, J. E. Box et al. "Climate of the Greenland ice sheet using a high-resolution climate model - Part 1: Evaluation." *The Cryosphere*, 4:511–527, 2010. doi:10.5194/tc-4-511-2010.
- Falk, U., D. A. López, and A. Silva-Busso. "Mult-year analysis of distributed glacier mass balance modelling and equilibrium line altitude on King George Island, Antarctic Peninsula." *The Cryosphere*, 12:1211–1232, 2018. doi:10.5194/tc-12-1211-2018.
- Farinotti, D., M. Huss, J. J. Fürst, J. Landmann, H. Machguth et al. "A consensus estimate for the ice thickness distribution of all glaciers on Earth." *Nature Geoscience*, 12:168–173, 2019. doi:10.1038/s41561-019-0300-3.
- Favier, L., G. Durand, S. L. Cornford, G. H. Gudmundsson, O. Gagliardini et al. "Retreat of Pine Island Glacier controlled by marine ice-sheet instability." *Nature Climate Change*, 4:117–121, 2014. doi:10.1038/nclimate2094.
- Flanner, M. G. and C. S. Zender. "Linking snowpack microphysics and albedo evolution." *Journal of Geophysical Research*, 111(D12208), 2006. doi:10.1029/2005JD006834.

- Flanner, M. G., C. S. Zender, J. T. Randerson, and P. J. Rasch. "Present-day climate forcing and response from black carbon in snow." *Journal of Geophysical Research*, 112(D11202), 2007. doi:10.1029/2006JD008003.
- Fountain, A. G., T. H. Nysten, A. J. Monaghan, H. J. Basagic, and D. H. Bromwich. "Snow in the McMurdo Dry Valleys, Antarctica." *International Journal of Climatology*, 30:633–642, 2010. doi:10.1002/joc.1933.
- Fretwell, P., H. D. Pritchard, D. G. Vaughan, J. L. Bamber, N. E. Barrand et al. "Bedmap2: improved ice bed, surface and thickness datasets for Antarctica." *The Cryosphere*, 7:375–393, 2013. doi:10.5194/tc-7-375-2013.
- Fürst, J. J., G. Durand, F. Gillet-Chaulet, L. Tavard, M. Rankl et al. "The safety band of Antarctic ice shelves." *Nature Climate Change*, 6:479–482, 2016. doi:10.1038/nclimate2912.
- Gardner, A. S. and M. J. Sharp. "A review of snow and ice albedo and the development of a new physically based broadband albedo parameterization." *Journal of Geophysical Research: Earth Surface*, 115(F01009), 2010. doi:10.1029/2009JF001444.
- Glasser, N. F. and T. A. Scambos. "A structural glaciological analysis of the 2002 Larsen B ice-shelf collapse." *Journal of Glaciology*, 54(184):3–16, 2008. doi:10.3189/002214308784409017.
- Grenfell, T. C. and D. K. Perovich. "Seasonal and spatial evolution of albedo in a snow-ice-land-ocean environment." *Journal of Geophysical Research*, 109(C1), 2004. doi:10.1029/2003JC001866.
- Grenfell, T. C., S. G. Warren, and P. C. Mullen. "Reflection of solar radiation by the Antarctic snow surface at ultraviolet, visible, and near-infrared wavelengths." *Journal of Geophysical Research*, 99(D9):18669–18684, 1994. doi:10.1029/94JD01484.
- Griggs, J. A. and J. L. Bamber. "Antarctic ice-shelf thickness from satellite radar altimetry." *Journal of Glaciology*, 57(203):485–498, 2011. doi:10.3189/002214311796905659.
- Hall, A. "The Role of Surface Albedo Feedback in Climate." *Journal of Climate*, 17:1550–1568, 2004. doi:10.1175/1520-0442(2004)017<1550:TROSAF>2.0.CO;2.
- Herman, J., M. T. DeLand, L.-K. Huang, G. Labow, D. Larko et al. "A net decrease in the Earth's cloud, aerosol, and surface 340 nm reflectivity during the past 33yr (1979–2011)." *Atmospheric Chemistry and Physics*, 13:8505–8524, 2013. doi:10.5194/acp-13-8505-2013.
- Herron, M. H. and C. C. Langway. "Firn Densification: An Empirical Model." *Journal of Glaciology*, 25(93):373–385, 1980. doi:10.3189/S0022143000015239.

- Hock, R. "Temperature index melt modelling in mountain areas." *Journal of Hydrology*, 282:104–115, 2003. doi:10.1016/S0022-1694(03)00257-9.
- Hogg, A. E. and G. H. Gudmundsson. "Impacts of the Larsen-C Ice Shelf calving event." *Nature Climate Change*, 7:540–542, 2017. doi:10.1038/nclimate3359.
- Holtslag, A. A. M. and H. A. R. De Bruin. "Applied Modeling of the Nighttime Surface Energy Balance over Land." *Journal of Applied Meteorology*, 27:689–704, 1988. doi:10.1175/1520-0450(1988)027<0689:AMOTNS>2.0.CO;2.
- Hori, M., T. Aoki, T. Tanikawa, H. Motoyoshi, A. Hachikubo et al. "In-situ measured spectral directional emissivity of snow and ice in the 8–14  $\mu\text{m}$  atmospheric windows." *Remote Sensing of the Environment*, 100:486–502, 2006. doi:10.1016/j.rse.2005.11.001.
- Jakobs, C. L., C. H. Reijmer, P. Kuipers Munneke, G. König-Langlo, and M. R. Van den Broeke. "Quantifying the snowmelt-albedo feedback at Neumayer Station, East Antarctica." *The Cryosphere*, 13:1473–1485, 2019. doi:10.5194/tc-13-1473-2019.
- Jakobs, C. L., C. H. Reijmer, C. J. P. P. Smeets, L. D. Trusel, W. J. Van de Berg et al. "A benchmark dataset of in situ Antarctic surface melt rates and energy balance." *Journal of Glaciology*, 66(256):291–302, 2020. doi:10.1017/jog.2020.6.
- Jakobs, C. L., C. H. Reijmer, M. R. Van den Broeke, W. J. Van de Berg, and J. M. Van Wessem. "Spatial variability of the snowmelt–albedo feedback in Antarctica." *Journal of Geophysical Research: Earth Surface*, 2021. doi:10.1029/2020JF005696.
- Jonsell, U. Y., F. J. Navarro, M. Bañón, J. J. Lapazaran, and J. Otero. "Sensitivity of a distributed temperature-radiation index melt model based on AWS observations and surface energy balance fluxes, Hurd Peninsula glaciers, Livingston Island, Antarctica." *The Cryosphere*, 6:539–552, 2012. doi:10.5194/tc-6-539-2012.
- Joughin, I., B. E. Smith, and B. Medley. "Marine Ice Sheet Collapse Potentially Under Way for the Thwaites Glacier Basin, West Antarctica." *Science*, 344:735–738, 2014. doi:10.1126/science.1249055.
- Keck, T., R. Preusker, and J. Fischer. "Retrieving snow and ice characteristics by remotely sensed emissivity using the multi-view brightness temperature within 8  $\mu\text{m}$  to 14  $\mu\text{m}$ ." *Remote Sensing of the Environment*, 201:181–195, 2017. doi:10.1016/j.rse.2017.09.006.
- Kennett, J. P. "Cenozoic Evolution of Antarctic Glaciation, the Circum-Antarctic Ocean, and Their Impact on Global Paleoceanography." *Journal of Geophysical Research*, 82(27):3843–3860, 1977. doi:10.1029/JCo82i027p03843.
- King, J. C. "Using satellite thermal infrared imagery to study boundary layer structure in an Antarctic katabatic wind region." *International Journal of Remote Sensing*, 19(17):3335–3348, 1998. doi:10.1080/014311698214028.

- King, J. C., A. Gadian, A. Kirchgaessner, P. Kuipers Munneke, T. A. Lachlan-Cope et al. "Validation of the summertime surface energy budget of Larsen C Ice Shelf (Antarctica) as represented in three high-resolution atmospheric models." *Journal of Geophysical Research: Atmospheres*, 120:1335–1347, 2015. doi:10.1002/2014JD022604.
- King, J. C., A. Kirchgaessner, S. L. Bevan, E. A. D., P. Kuipers Munneke et al. "The Impact of Föhn winds on surface energy balance during the 2010–2011 melt season over larsen c ice shelf, antarctica." *Journal of Geophysical Research: Atmospheres*, 122:12062–12076, 2017. doi:10.1002/2017JD026809.
- Kingslake, J., J. C. Ely, I. Das, and R. E. Bell. "Widespread movement of meltwater onto and across Antarctic ice shelves." *Nature*, 544:349–352, 2017. doi:10.1038/nature22049.
- Kirchgaessner, A., J. C. King, and A. Gadian. "The Representation of Föhn events to the east of the antarctic peninsula in simulations by the antarctic mesoscale prediction system." *Journal of Geophysical Research: Atmospheres*, 124:13663–13679, 2019. doi:10.1029/2019JD030637.
- König, G. "Roughness Length of an Antarctic Ice Shelf." *Polarforschung*, 55(1):27–32, 1985. doi:10.2312/polarforschung.55.1.27.
- König-Langlo, G. "Basic and other measurements, and meteorological synoptical observations from Neumayer Station, 1992–04 to 2016–01, reference list of 572 datasets." 2017.
- König-Langlo, G. and B. Loose. "The Meteorological Observatory at Neumayer Stations (GvN and NM-II) Antarctica." *Polarforschung*, 76:25–38, 2007.
- Kuipers Munneke, P., S. R. M. Ligtenberg, M. R. Van den Broeke, and D. G. Vaughan. "Firn air depletion as a precursor of Antarctic ice-shelf collapse." *Journal of Glaciology*, 60(220):205–214, 2014. doi:10.3189/2014JoG13J183.
- Kuipers Munneke, P., A. J. Luckman, S. L. Bevan, C. J. P. P. Smeets, E. Gilbert et al. "Intense Winter Surface Melt on an Antarctic Ice Shelf." *Geophysical Research Letters*, 45:7615–7623, 2018. doi:10.1029/2018GL077899.
- Kuipers Munneke, P., D. McGrath, B. Medley, A. J. Luckman, S. L. Bevan et al. "Observationally constrained surface mass balance of Larsen C ice shelf, Antarctica." *The Cryosphere*, 11:2411–2426, 2017. doi:10.5194/tc-11-2411-2017.
- Kuipers Munneke, P., G. Picard, M. R. Van den Broeke, J. T. M. Lenaerts, and E. Van Meijgaard. "Insignificant changes in Antarctic snowmelt volume since 1979." *Geophysical Research Letters*, 39:L01501, 2012a. doi:10.1029/2011GL050207.
- Kuipers Munneke, P., C. H. Reijmer, and M. R. Van den Broeke. "Assessing the retrieval of cloud properties from radiation measurements over snow and ice." *International Journal of Climatology*, 31:756–769, 2011a. doi:10.1002/joc.2114.

- Kuipers Munneke, P., M. R. Van den Broeke, J. C. King, T. Gray, and C. H. Reijmer. "Near-surface climate and surface energy budget of Larsen C ice shelf, Antarctic Peninsula." *The Cryosphere*, 6:353–363, 2012b. doi:10.5194/tc-6-353-2012.
- Kuipers Munneke, P., M. R. Van den Broeke, J. T. M. Lenaerts, M. G. Flanner, A. S. Gardner et al. "A new albedo parameterization for use in climate models over the Antarctic ice sheet." *Journal of Geophysical Research: Atmospheres*, 116(D05114), 2011b. doi:10.1029/2010JD015113.
- Kuipers Munneke, P., M. R. Van den Broeke, C. H. Reijmer, M. M. Helsen, W. Boot et al. "The role of radiation penetration in the energy budget of the snowpack at Summit, Greenland." *The Cryosphere*, 3:155–165, 2009. doi:10.5194/tc-3-155-2009.
- Leeson, A. A., J. M. Van Wessem, S. R. M. Ligtenberg, A. Shepherd, M. R. Van den Broeke et al. "Regional climate of the Larsen B embayment 1980-2014." *Journal of Glaciology*, 63(240):683–690, 2017. doi:10.1017/jog.2017.39.
- Lenaerts, J. T. M., S. Lhermitte, R. Drews, S. R. M. Ligtenberg, S. Berger et al. "Meltwater produced by wind-albedo interaction stored in an East Antarctic ice shelf." *Nature Climate Change*, 7:58–62, 2017. doi:10.1038/nclimate3180.
- Lenaerts, J. T. M., B. Medley, M. R. Van den Broeke, and B. Wouters. "Observing and Modeling Ice Sheet Surface Mass Balance." *Reviews of Geophysics*, 57:376–420, 2019. doi:10.1029/2018RG000622.
- Lenaerts, J. T. M. and M. R. Van den Broeke. "Modeling drifting snow in Antarctica with a regional climate model: 2. Results." *Journal of Geophysical Research*, 117(D05109), 2012. doi:10.1029/2010JD015419.
- Lenaerts, J. T. M., M. R. Van den Broeke, S. J. Déry, E. Van Meijgaard, W. J. Van de Berg et al. "Modeling drifting snow in Antarctica with a regional climate model: 1. Methods and model evaluation." *Journal of Geophysical Research: Atmospheres*, 117(D05108), 2012. doi:10.1029/2011JD016145.
- Lenaerts, J. T. M., M. R. Van den Broeke, J. M. Van Wessem, W. J. Van de Berg, E. Van Meijgaard et al. "Extreme Precipitation and Climate Gradients in Patagonia Revealed by High-Resolution Regional Atmospheric Climate Modeling." *Journal of Climate*, 27:4607–4621, 2014. doi:10.1175/JCLI-D-13-00579.1.
- Lenderink, G., B. J. J. M. Van den Hurk, E. Van Meijgaard, A. Van Ulden, and H. Cuijpers. "Simulation of present-day climate in RACMO2: first results and model developments." Technical report, KNMI, 2003.
- Li, X., E. Rignot, J. Mouginot, and B. Scheuchl. "Ice flow dynamics and mass loss of Totten Glacier, East Antarctica, from 1989 to 2015." *Geophysical Research Letters*, 43:6366–6373, 2016. doi:10.1002/2016GL069173.

- Libois, Q., G. Picard, L. Arnaud, M. Dumont, M. Lafaysse et al. "Summertime evolution of snow specific surface area close to the surface on the Antarctic Plateau." *The Cryosphere*, 9:2383–2398, 2015. doi:10.5194/tc-9-2383-2015.
- Ligtenberg, S. R. M., M. M. Helsen, and M. R. Van den Broeke. "An improved semi-empirical model for the densification of Antarctic firn." *The Cryosphere*, 5:809–819, 2011. doi:10.5194/tc-5-809-2011.
- Ligtenberg, S. R. M., P. Kuipers Munneke, and M. R. Van den Broeke. "Present and future variations in Antarctic firn air content." *The Cryosphere*, 8:1711–1723, 2014. doi:10.5194/tc-8-1711-2014.
- Luckman, A., E. A., D. Jansen, B. Kulesa, P. Kuipers Munneke et al. "Surface melt and ponding on Larsen C Ice Shelf and the impact of föhn winds." *Antarctic Science*, 26(6):625–635, 2014. doi:10.1017/S0954102014000339.
- Marquetto, L., S. Kaspari, and J. C. Simões. "Refractory black carbon (rBC) variability in a 47-year West Antarctic snow and firn core." *The Cryosphere*, 14:1537–1554, 2020. doi:tc-14-1537-2020.
- Marshall, G. J. and J. C. King. "Southern Hemisphere circulation anomalies associated with extreme Antarctic Peninsula winter temperatures." *Geophysical Research Letters*, 25(13):2437–2440, 1998. doi:10.1029/98GL01651.
- Marshall, G. J., A. Orr, N. P. M. Van Lipzig, and J. C. King. "The Impact of a Changing Southern Hemisphere Annular Mode on Antarctic Peninsula Summer Temperatures." *Journal of Climate*, 19:5388–5404, 2006. doi:10.1175/JCLI3844.1.
- Martinson, D. G. "Antarctic circumpolar current's role in the Antarctic ice system: An overview." *Palaeogeography, palaeoclimatology, palaeoecology*, 335-336:71–74, 2012. doi:10.1016/j.palaeo.2011.04.007.
- Martinson, D. G., S. E. Stammerjohn, R. A. Iannuzzi, R. C. Smith, and M. Vernet. "Western Antarctic Peninsula physical oceanography and spatio-temporal variability." *Deep-Sea Research II*, 55:1964–1987, 2008. doi:10.1016/j.dsr2.2008.04.038.
- Massom, R. A., T. A. Scambos, L. G. Bennetts, P. A. Reid, V. A. Squire et al. "Antarctic ice shelf disintegration triggered by sea ice loss and ocean swell." *Nature*, 558:383–389, 2018. doi:10.1038/s41586-018-0212-1.
- Meredith, M., M. Sommerkorn, S. Cassotta, C. Derksen, A. Ekaykin et al. *Polar Regions*, chapter 3. IPCC Special Report on the Ocean and Cryosphere in a Changing Climate. in press., 2019.
- Meredith, M. P. and J. C. King. "Rapid climate change in the ocean west of the Antarctic Peninsula during the second half of the 20th century." *Geophysical Research Letters*, 32(L19604), 2005. doi:10.1029/2005GL024042.

- Monin, A. S. and A. M. Obukhov. "Basic laws of turbulent mixing in the surface layer of the atmosphere." *Proceedings of the Academy of Sciences of the USSR. Geological sciences sections*, 24(151):163–187, 1954.
- Morlighem, M., E. Rignot, T. Binder, D. D. Blankenship, R. Drews et al. "Deep glacial troughs and stabilizing ridges unveiled beneath the margins of the Antarctic ice sheet." *Nature Geoscience*, 13:132–137, 2020. doi:10.1038/s41561-019-0510-8.
- Morlighem, M., C. N. Williams, E. Rignot, L. An, J. E. Arndt et al. "BedMachine v3: Complete Bed Topography and Ocean Bathymetry Mapping of Greenland From Multibeam Echo Sounding Combined With Mass Conservation." *Geophysical Research Letters*, 44:11051–11061, 2017. doi:10.1002/2017GL074954.
- Morris, E. M. and D. G. Vaughan. *Spatial and Temporal Variation of Surface Temperature on the Antarctic Peninsula And The Limit of Viability of Ice Shelves*, volume 79 of *Antarctic Research Series*, chapter 5, pages 61–68. American Geophysical Union, Washington, D. C., 2013. doi:10.1029/AR079p0061.
- Mottram, R., K. P. Nielsen, E. Gleeson, and X. Yang. "Modelling Glaciers in the HARMONIE-AROME NWP model." *Advances in Science & Research*, 14:323–334, 2017. doi:10.5194/asr-14-323-2017.
- Mouginot, J., E. Rignot, A. A. Bjørk, M. R. Van den Broeke, R. Millan et al. "Forty-six years of Greenland Ice Sheet mass balance from 1972 to 2018." *Proceedings of the National Academy of Sciences of the United States of America*, 116(19):9239–9244, 2019. doi:10.1073/pnas.1904242116.
- Nicolas, J. P. and D. H. Bromwich. "New Reconstruction of Antarctic Near-Surface Temperatures: Multidecadal Trends and Reliability of Global Reanalyses." *Journal of Climate*, 27:8070–8093, 2014. doi:10.1175/JCLI-D-13-0733.1.
- Noël, B. P. Y., C. L. Jakobs, W. J. J. Van Pelt, S. Lhermitte, B. Wouters et al. "Low elevation of Svalbard glaciers drives high mass loss variability." *Nature Communications*, 2020a. In review.
- Noël, B. P. Y., W. J. Van de Berg, S. Lhermitte, and M. R. Van den Broeke. "Rapid ablation zone expansion amplifies north Greenland mass loss." *Science Advances*, 5(9), 2019. doi:10.1126/sciadv.aaw0123.
- Noël, B. P. Y., W. J. Van de Berg, S. Lhermitte, B. Wouters, N. Schaffer et al. "Six Decades of Glacial Mass Loss in the Canadian Arctic Archipelago." *Journal of Geophysical Research: Earth Surface*, 123:1430–1449, 2018a. doi:10.1029/2017JF004304.
- Noël, B. P. Y., W. J. Van de Berg, E. Van Meijgaard, P. Kuipers Munneke, R. S. W. Van de Wal et al. "Evaluation of the updated regional climate model RACMO2.3: summer snowfall impact on the Greenland Ice Sheet." *The Cryosphere*, 8:1831–1844, 2015. doi:10.5194/tc-9-1831-2015.

- Noël, B. P. Y., W. J. Van de Berg, J. M. Van Wessem, E. Van Meijgaard, D. Van As et al. “Modelling the climate and surface mass balance of polar ice sheets using RACMO2, part 1: Greenland (1958–2016).” *The Cryosphere*, 12:811–831, 2018b. doi:10.5194/tc-12-811-2018.
- Noël, B. P. Y., L. Van Kampenhout, W. J. Van de Berg, J. T. M. Lenaerts, B. Wouters et al. “Brief communication: CESM2 climate forcing (1950–2014) yields realistic Greenland ice sheet surface mass balance.” *The Cryosphere*, 14:1425–1435, 2020b. doi:10.5194/tc-14-1425-2020.
- Oerlemans, J. and W. H. Knap. “A 1 year record of global radiation and albedo in the ablation zone of Morteratschgletscher, Switzerland.” *Journal of Glaciology*, 44(147):231–238, 1998. doi:10.3189/S0022143000002574.
- Oppenheimer, M., B. C. Glavovic, J. Hinkel, R. S. W. Van de Wal, A. K. Magnan et al. *Sea Level Rise and Implications for Low-Lying Islands, Coasts and Communities*, chapter 4. IPCC Special Report on the Ocean and Cryosphere in a Changing Climate. in press., 2019.
- Padman, L., D. P. Costa, M. S. Dinniman, H. A. Fricker, M. E. Goebel et al. “Oceanic controls on the mass balance of Wilkins Ice Shelf, Antarctica.” *Journal of Geophysical Research*, 117(C01010), 2012. doi:10.1029/2011JC007301.
- Perovich, D. K., T. C. Grenfell, B. Light, and P. V. Hobbs. “Seasonal evolution of the albedo of multiyear Arctic sea ice.” *Journal of Geophysical Research*, 107(C10)(8044), 2002. doi:10.1029/2000JC000438.
- Perovich, D. K. and C. Polashenski. “Albedo evolution of seasonal Arctic sea ice.” *Geophysical Research Letters*, 39(8), 2012. doi:10.1029/2012GL051432.
- Picard, G., F. Domine, G. Krinner, L. Arnaud, and E. Lefebvre. “Inhibition of the positive snow-albedo feedback by precipitation in interior Antarctica.” *Nature Climate Change*, 2:795–798, 2012. doi:10.1038/nclimate1590.
- Picard, G., M. Fily, and H. Gallée. “Surface melting derived from microwave radiometers: a climatic indicator in Antarctica.” *Annals of Glaciology*, 46:29–34, 2007. doi:10.3189/172756407782871684.
- Picard, G., Q. Libois, L. Arnaud, G. Verin, and M. Dumont. “Development and calibration of an automatic spectral albedometer to estimate near-surface snow SSA time series.” *The Cryosphere*, 10:1297–1316, 2016. doi:10.5194/tc-10-1297-2016.
- Pritchard, H. D., S. R. M. Ligtenberg, H. A. Fricker, D. G. Vaughan, M. R. Van den Broeke et al. “Antarctic ice-sheet loss driven by basal melting of ice shelves.” *Nature*, 484:502–505, 2012. doi:10.1038/nature10968.
- Qu, X. and A. Hall. “What Controls the Strength of Snow-Albedo Feedback?” *Journal of Climate*, 20:3971–3981, 2007. doi:10.1175/JCLI4186.1.

- Reese, R., G. H. Gudmundsson, A. Levermann, and R. Winkelmann. "The far reach of ice-shelf thinning in Antarctica." *Nature Climate Change*, 8:53–57, 2018. doi:10.1038/s41558-017-0020-x.
- Reijmer, C. H., W. Greuell, and J. Oerlemans. "The annual cycle of meteorological variables and the surface energy balance on Berkner Island, Antarctica." *Annals of Glaciology*, 29:49–54, 1999. doi:10.3189/172756499781821166.
- Reijmer, C. H. and J. Oerlemans. "Temporal and spatial variability of the surface energy balance in Dronning Maud Land, East Antarctica." *Journal of Geophysical Research*, 107(D24)(4759), 2002. doi:10.1029/2000JD000110.
- Reijmer, C. H., E. Van Meijgaard, and M. R. Van den Broeke. "Evaluation of temperature and wind over Antarctica in a Regional Atmospheric Climate Model using 1 year of automatic weather station data and upper air observations." *Journal of Geophysical Research*, 110(D04103), 2005. doi:10.1029/2004JD005234.
- Rignot, E., G. Casassa, P. Gogineni, W. Krabill, A. Rivera et al. "Accelerated ice discharge from the Antarctic Peninsula following the collapse of Larsen B ice shelf." *Geophysical Research Letters*, 31(L18401), 2004. doi:10.1029/2004GL020697.
- Rignot, E., J. Mouginot, M. Morlighem, H. Seroussi, and B. Scheuchl. "Widespread, rapid grounding line retreat of Pine Island, Thwaites, Smith, and Kohler glaciers, West Antarctica, from 1992 to 2011." *Geophysical Research Letters*, 41:3502–3509, 2014. doi:10.1002/2014GL060140.
- Rignot, E., J. Mouginot, B. Scheuchl, M. R. Van den Broeke, J. M. Van Wessem et al. "Four decades of Antarctic Ice Sheet mass balance from 1979–2017." *Proceedings of the National Academy of Sciences of the United States of America*, 116(4):1095–1103, 2019. doi:10.1073/pnas.1812883116.
- Rott, H., F. Müller, T. Nagler, and D. Floricioiu. "The imbalance of glaciers after disintegration of Larsen-B ice shelf, Antarctic Peninsula." *The Cryosphere*, 5:125–134, 2011. doi:10.5194/tc-5-125-2011.
- Scambos, T. A., J. A. Bohlander, C. A. Shuman, and P. Skvarca. "Glacier acceleration and thinning after ice shelf collapse in the Larsen B embayment, Antarctica." *Geophysical Research Letters*, 31(L18402), 2004. doi:10.1029/2004GL020670.
- Schlatter, T. W. "The Local Surface Energy Balance and Subsurface Temperature Regime in Antarctica." *Journal of Applied Meteorology*, 11:1048–1062, 1972. doi:10.1175/1520-0450(1972)011<1048:TLSEBA>2.0.CO;2.
- Schneider, T. and P. Jansson. "Internal accumulation in firn and its significance for the mass balance of Storglaciären, Sweden." *Journal of Glaciology*, 50(168):25–34, 2004. doi:10.3189/172756504781830277.

- Schoof, C. “Ice sheet grounding line dynamics: Steady states, stability, and hysteresis.” *Journal of Geophysical Research*, 112(F03S28), 2007. doi:10.1029/2006JF000664.
- Scott, R. C., J. P. Nicolas, D. H. Bromwich, J. R. Norris, and D. Lubin. “Meteorological Drivers and Large-Scale Climate Forcing of West Antarctic Surface Melt.” *Journal of Climate*, 32:665–684, 2019. doi:10.1175/JCLI-D-18-0233.1.
- Shepherd, A., E. R. Ivins, E. Rignot, B. Smith, M. R. Van den Broeke et al. “Mass balance of the Antarctic Ice Sheet from 1992 to 2017.” *Nature*, 558:219–222, 2018. doi:10.1038/s41586-018-0179-y.
- Smeets, C. J. P. P., P. Kuipers Munneke, D. Van As, M. R. Van den Broeke, W. Boot et al. “The K-transect in west Greenland: Automatic weather station data (1993–2016).” *Arctic, Antarctic, and Alpine Research*, 50(1), 2018. doi:10.1080/15230430.2017.1420954.
- Smeets, C. J. P. P. and M. R. Van den Broeke. “Temporal and Spatial Variations of the Aerodynamic Roughness Length in the Ablation Zone of the Greenland Ice Sheet.” *Boundary-Layer Meteorology*, 128:315–338, 2008. doi:10.1007/s10546-008-9291-0.
- Souvereinjs, N., A. Gossart, M. Demuzere, J. T. M. Lenaerts, B. Medley et al. “A New Regional Climate Model for POLAR-CORDEX: Evaluation of a 30-Year Hindcast with COSMO-CLM<sup>2</sup> Over Antarctica.” *Journal of Geophysical Research: Atmospheres*, 124:1405–1427, 2019. doi:10.1029/2018JD028862.
- Speirs, J., D. F. Steinhoff, H. A. McGowan, D. H. Bromwich, and A. J. Monaghan. “Foehn Winds in the McMurdo Dry Valleys, Antarctica: The Origin of Extreme Warming Events.” *Journal of Climate*, 23:3577–3598, 2010. doi:10.1175/2010JCLI3382.1.
- Steger, C. R., C. H. Reijmer, and M. R. Van den Broeke. “The modelled liquid water balance of the Greenland Ice Sheet.” *The Cryosphere*, 11:2507–2526, 2017. doi:10.5194/tc-11-2507-2017.
- Stokes, C. R., J. E. Sanderson, B. W. J. Miles, S. S. R. Jamieson, and A. A. Leeson. “Widespread distribution of supraglacial lakes around the margin of the East Antarctic Ice Sheet.” *Scientific Reports*, 9:13823, 2019. doi:10.1038/s41598-019-50343-5.
- Tedesco, M. “Assessment and development of snowmelt retrieval algorithms over Antarctica from K-band spaceborn brightness temperature (1979–2008).” *Remote Sensing of Environment*, 113:979–997, 2009. doi:10.1016/j.rse.2009.01.009.
- Trusel, L. D., K. E. Frey, and S. B. Das. “Antarctic surface melting dynamics: Enhanced perspectives from radar scatterometer data.” *Journal of Geophysical Research*, 117:F02023, 2012. doi:10.1029/2011JF002126.

- Trusel, L. D., K. E. Frey, S. B. Das, K. B. Karnauskas, P. Kuipers Munneke et al. “Divergent trajectories of Antarctic surface melt under two twenty-first-century climate scenarios.” *Nature Geoscience*, 8:927–934, 2015. doi:10.1038/NNGEO2563.
- Trusel, L. D., K. E. Frey, S. B. Das, P. Kuipers Munneke, and M. R. Van den Broeke. “Satellite-based estimates of Antarctic surface meltwater fluxes.” *Geophysical Research Letters*, 40:6148–6153, 2013. doi:10.1002/2013GL058138.
- Turner, J., T. A. Lachlan-Cope, G. J. Marshall, E. M. Morris, R. Mulvaney et al. “Spatial variability of Antarctic Peninsula net surface mass balance.” *Journal of Geophysical Research*, 107(D13):4173, 2002. doi:10.1029/2001JD000755.
- Turner, J., H. Lu, I. White, J. C. King, T. Phillips et al. “Absence of 21st century warming on Antarctic Peninsula consistent with natural variability.” *Nature*, 535:411–415, 2016. doi:10.1038/nature18645.
- Turner, J., T. Maksym, T. Phillips, G. J. Marshall, and M. P. Meredith. “The impact of changes in sea ice advance on the large winter warming on the western Antarctic Peninsula.” *International Journal of Climatology*, 33:852–861, 2013. doi:10.1002/joc.3474.
- Turner, J., A. Orr, G. H. Gudmundsson, A. Jenkins, R. G. Bingham et al. “Atmosphere-ocean-ice interactions in the Amundsen Sea Embayment, West Antarctica.” *Reviews of Geophysics*, 55:235–276, 2017. doi:10.1002/2016RG000532.
- Turton, J. V., A. Kirchgaessner, A. N. Ross, and J. C. King. “The spatial distribution and temporal variability of föhn winds over the Larsen C ice shelf, Antarctica.” *Quarterly Journal of the Royal Meteorological Society*, 144:1169–1178, 2018. doi:10.1002/qj.3284.
- Undén, P., L. Rontu, H. Järvinen, P. Lynch, J. Calvo et al. *HIRLAM-5 Scientific Documentation*, 2002. [Online; accessed 25 January 2017].
- Välisuo, I., T. Vihma, and J. C. King. “Surface energy budget on Larsen and Wilkins ice shelves in the Antarctic Peninsula: results based on reanalyses in 1989–2010.” *The Cryosphere*, 8:1519–1538, 2014. doi:10.5194/tc-8-1519-2014.
- Van Angelen, J. H., J. T. M. Lenaerts, S. Lhermitte, X. Fettweis, P. Kuipers Munneke et al. “Sensitivity of Greenland Ice Sheet surface mass balance to surface albedo parameterization: a study with a regional climate model.” *The Cryosphere*, 6:1175–1186, 2012. doi:10.5194/tc-6-1175-2012.
- Van As, D., R. S. Fausto, W. T. Colgan, J. E. Box, A. P. Ahlstrøm et al. “Darkening of the Greenland ice sheet due to the melt-albedo feedback observed at PROMICE weather stations.” *Geological Survey of Denmark and Greenland Bulletin*, 28:69–72, 2013.

- Van As, D., M. R. Van den Broeke, C. H. Reijmer, and R. S. W. Van de Wal. "The Summer Surface Energy Balance of the High Antarctic Plateau." *Boundary-Layer Meteorology*, 115:289–317, 2005. doi:10.1007/s10546-004-4631-1.
- Van Dalum, C. T., W. J. Van de Berg, S. Lhermitte, and M. R. Van den Broeke. "Evaluation of a new snow albedo scheme for the Greenland ice sheet in the regional climate model RACMO2." *The Cryosphere Discussions*, 2020. doi:10.5194/tc-2020-118. In review.
- Van Dalum, C. T., W. J. Van de Berg, Q. Libois, G. Picard, and M. R. Van den Broeke. "A module to convert spectral to narrowband snow albedo for use in climate models: SNOWBAL v1.2." *Geoscientific Model Development*, 12:5157–5175, 2019. doi:10.5194/gmd-12-5157-2019.
- Van de Berg, W. J. and B. Medley. "Brief Communication: Upper-air relaxation in RACMO2 significantly improved modelled interannual surface mass balance variability in Antarctica." *The Cryosphere*, 10:459–463, 2016. doi:10.5194/tc-10-459-2016.
- Van de Berg, W. J., E. Van Meijgaard, and L. H. Van Ulft. "The added value of high resolution in estimating the surface mass balance in southern Greenland." *The Cryosphere*, 14:1809–1827, 2020. doi:10.5194/tc-14-1809-2020.
- Van den Broeke, M. R. "The semi-annual oscillation and Antarctic climate. Part 1: influence on near surface temperatures (1957-79)." *Antarctic Science*, 10(2):175–183, 1998. doi:10.1017/S0954102098000248.
- Van den Broeke, M. R. "Strong surface melting preceded collapse of Antarctic Peninsula ice shelf." *Geophysical Research Letters*, 32(L12815), 2005. doi:10.1029/2005GL023247.
- Van den Broeke, M. R., C. Bus, J. Ettema, and C. J. P. P. Smeets. "Temperature thresholds for degree-day modelling of Greenland ice sheet melt rates." *Geophysical Research Letters*, 37:L18501, 2010a. doi:10.1029/2010GL044123.
- Van den Broeke, M. R., G. König-Langlo, G. Picard, P. Kuipers Munneke, and J. T. M. Lenaerts. "Surface energy balance, melt and sublimation at Neumayer Station, East Antarctica." *Antarctic Science*, 22(1):87–96, 2010b. doi:10.1017/S095410200990538.
- Van den Broeke, M. R., C. H. Reijmer, D. Van As, and W. Boot. "Daily cycle of the surface energy balance in Antarctica and the influence of clouds." *International Journal of Climatology*, 26:1587–1605, 2006. doi:10.1002/joc.1323.
- Van den Broeke, M. R., C. H. Reijmer, D. Van As, R. S. W. Van de Wal, and J. Oerlemans. "Seasonal cycles of Antarctic surface energy balance from automatic weather stations." *Annals of Glaciology*, 41:131–139, 2005a. doi:10.3189/172756405781813168.

- Van den Broeke, M. R., C. H. Reijmer, and R. S. W. Van de Wal. "A study of the surface mass balance in Dronning Maud Land, Antarctica, using automatic weather stations." *Journal of Glaciology*, 50(171):565–581, 2004a. doi:10.3189/172756504781829756.
- Van den Broeke, M. R., C. H. Reijmer, and R. S. W. Van de Wal. "Surface radiation balance in Antarctica as measured with automatic weather stations." *Journal of Geophysical Research*, 109(D09103), 2004b. doi:10.1029/2003JD004394.
- Van den Broeke, M. R., D. Van As, C. H. Reijmer, and R. S. W. Van de Wal. "Assessing and Improving the Quality of Unattended Radiation Observations in Antarctica." *Journal of Atmospheric and Oceanic Technology*, 21:1417–1431, 2004c. doi:10.1175/1520-0426(2004)021<1417:AAITQO>2.0.CO;2.
- Van den Broeke, M. R., D. Van As, C. H. Reijmer, and R. S. W. Van de Wal. "Sensible heat exchange at the Antarctic snow surface: a study with automatic weather stations." *International Journal of Climatology*, 25:1081–1101, 2005b. doi:10.1002/joc.1152.
- Van den Broeke, M. R., J.-G. Winther, E. Isaksson, J. F. Pinglot, L. Karlöf et al. "Climate variables along a traverse line in Dronning Maud Land, East Antarctica." *Journal of Glaciology*, 45(150):295–302, 1999. doi:10.3189/S0022143000001799.
- Van der Veen, C. J. "Fracture propagation as means of rapidly transferring surface meltwater to the base of glaciers." *Geophysical Research Letters*, 34(L01501), 2007. doi:10.1029/2006GL028385.
- Van Kampenhout, L., J. T. M. Lenaerts, W. H. Lipscomb, W. J. Sacks, D. M. Lawrence et al. "Improving the Representation of Polar Snow and Firn in the Community Earth System Model." *Journal of Advances in Modeling Earth Systems*, 9:2583–2600, 2017. doi:10.1002/2017MS000988.
- Van Lipzig, N. P. M., G. J. Marshall, A. Orr, and J. C. King. "The Relationship between the Southern Hemisphere Annular Mode and Antarctic Peninsula Summer Temperatures: Analysis of a High-Resolution Model Climatology." *Journal of Climate*, 21:1649–1668, 2008. doi:10.1175/2007JCLI1695.1.
- Van Meijgaard, E., L. H. Van Ulft, G. Lenderink, S. R. De Roode, L. Wipfler et al. "Refinement and application of a regional atmospheric model for climate scenario calculations of Western Europe." Technical report, Wageningen University, 2012.
- Van Meijgaard, E., L. H. Van Ulft, W. J. Van de Berg, F. C. Bosveld, B. J. J. M. Van den Hurk et al. "The KNMI regional atmospheric climate model RACMO version 2.1." *Koninklijk Nederlands Meteorologisch Instituut*, 43, 2008.
- Van Tiggelen, M., C. J. P. P. Smeets, C. H. Reijmer, and M. R. Van den Broeke. "A Vertical Propeller Eddy-Covariance Method and Its Application to Long-term Monitoring of Surface Turbulent Fluxes on the Greenland Ice Sheet." *Boundary-Layer Meteorology*, 2020. doi:10.1007/s10546-020-00536-7.

- Van Wessem, J. M., C. H. Reijmer, J. T. M. Lenaerts, W. J. Van de Berg, M. R. Van den Broeke et al. "Updated cloud physics in a regional atmospheric climate model improves the modelled surface energy balance of Antarctica." *The Cryosphere*, 8:125–135, 2014a. doi:10.5194/tc-8-125-2014.
- Van Wessem, J. M., C. H. Reijmer, M. Morlighem, J. Mouginot, E. Rignot et al. "Improved representation of East Antarctic surface mass balance in a regional atmospheric climate model." *Journal of Glaciology*, 60(222):761–770, 2014b. doi:10.3189/2014JoG14J051.
- Van Wessem, J. M., C. H. Reijmer, W. J. Van de Berg, and M. R. Van den Broeke. "Temperature and Wind Climate of the Antarctic Peninsula as Simulated by a High-Resolution Regional Atmospheric Climate Model." *Journal of Climate*, 28:7306–7326, 2015. doi:10.1175/JCLI-D-15-0060.1.
- Van Wessem, J. M., W. J. Van de Berg, B. P. Y. Noël, E. Van Meijgaard, G. Birnbaum et al. "Modelling the climate and surface mass balance of polar ice sheets using RACMO2, part 2: Antarctica (1979–2016)." *The Cryosphere*, 12:1479–1498, 2018. doi:10.5194/tc-2017-202.
- Vaughan, D. G. "West Antarctic Ice Sheet collapse - the fall and rise of a paradigm." *Climatic Change*, 91:65–79, 2008. doi:10.1007/s10584-008-9448-3.
- Wake, L. M. and S. J. Marshall. "Assessment of current methods of positive degree-day calculation using in situ observations from glaciated regions." *Journal of Glaciology*, 61(226):329–344, 2015. doi:10.3189/2015JoG14J116.
- Wang, W., C. S. Zender, D. Van As, C. J. P. P. Smeets, and M. R. Van den Broeke. "A Retrospective, Iterative, Geometry-Based (RIGB) tilt-correction method for radiation observed by automatic weather stations on snow-covered surfaces: application to Greenland." *The Cryosphere*, 10:727–741, 2016. doi:10.5194/tc-10-727-2016.
- Warren, S. G. "Optical constants of ice from the ultraviolet to the microwave." *Applied Optics*, 23(8):1206–1225, 1984. doi:10.1364/AO.23.001206.
- Warren, S. G. and A. D. Clarke. "Soot in the Atmosphere and Snow Surface of Antarctica." *Journal of Geophysical Research*, 95(D2):1811–1816, 1990. doi:10.1029/JD095iD02p01811.
- Weertman, J. "Stability of the Junction of an Ice Sheet and an Ice Shelf." *Journal of Glaciology*, 13(67):3–11, 1974. doi:10.3189/S0022143000023327.
- Wiesenkcker, J. M., P. Kuipers Munneke, M. R. Van den Broeke, and C. J. P. P. Smeets. "A Multidecadal Analysis of Föhn winds over larsen c ice shelf from a combination of observations and modeling." *Atmosphere*, 9:172, 2018. doi:10.3390/atmos9050172.

- Wiscombe, W. J. and S. G. Warren. "A Model for the Spectral Albedo of Snow. I: Pure Snow." *Journal of the Atmospheric Sciences*, 37:2712–2733, 1980. doi:10.1175/1520-0469(1980)037<2712:AMFTSA>2.0.CO;2.
- Wouters, B., A. Martín-Español, V. Helm, T. Flament, J. M. Van Wessem et al. "Dynamic thinning of glaciers on the Southern Antarctic Peninsula." *Science*, 348(6237):899–903, 2015. doi:10.1126/science.aaa5727.

## Publication list

### First-author papers

1. **C.L. Jakobs**, C.H. Reijmer, P. Kuipers Munneke, G. König-Langlo, and M.R. Van den Broeke. Quantifying the snowmelt–albedo feedback at Neumayer Station, East Antarctica. *The Cryosphere*, 13:1473–1485, 2019. doi:10.5194/tc-13-1473-2019
2. **C.L. Jakobs**, C.H. Reijmer, C.J.P.P. Smeets, L.D. Trusel, W.J. Van de Berg, M.R. Van den Broeke, and J.M. Van Wessem. A benchmark dataset of in situ Antarctic surface melt rates and energy balance. *Journal of Glaciology*, 66(256):291–302, 2020. doi:10.1017/jog.2020.6
3. **C.L. Jakobs**, C.H. Reijmer, M.R. Van den Broeke, W.J. Van de Berg, and J.M. Van Wessem. Spatial variability of the snowmelt–albedo feedback in Antarctica. *Journal of Geophysical Research: Earth Surface*, 2021. doi:10.1029/2020JF005696

### Other publications

4. J.M. Van Wessem, W.J. Van de Berg, B.P.Y. Noël, E. Van Meijgaard, G. Birnbaum, **C.L. Jakobs**, K. Krüger, J.T.M. Lenaerts, S. Lhermitte, S.R.M. Ligtenberg, B. Medley, C.H. Reijmer, K. Van Tricht, L.D. Trusel, L.H. Van Uft, B. Wouters, J. Wuite, and M.R. Van den Broeke. Modelling the climate and surface mass balance of polar ice sheets using RACMO2, part 2: Antarctica (1979–2016). *The Cryosphere*, 12:1479–1498, 2018. doi:10.5194/tc-2017-202
5. W.J.J. Van Pelt, V.A. Pohjola, R. Pettersson, L.E. Ehwald, C.H. Reijmer, W. Boot, and **C.L. Jakobs**. Dynamic Reponse of a High Arctic Glacier to Melt and Runoff Variations. *Geophysical Research Letters*, 45(10):4917–4926, 2018. doi:10.1029/2018GL077252
6. B.P.Y. Noël, **C.L. Jakobs**, W.J.J. Van Pelt, S. Lhermitte, B. Wouters, J. Kohler, J.O. Hagen, B. Luks, C.H. Reijmer, W.J. Van de Berg, and M.R. Van den Broeke. Low elevation of Svalbard glaciers drives high mass loss variability. *Nature Communications*, 2020, *accepted*

## Acknowledgements

I could start with thanking you, the reader, for reading my thesis. However, you probably skipped ahead to this part, so the gratitude is not yet entirely deserved.

Many thanks go to my supervisors, Michiel and Carleen. I couldn't have wished for a better team and I hope that many more PhD students will be guided by you. You always took as much time as necessary, once a week or more often if needed, to discuss the progress of my project. Michiel, if I showed a result to you that didn't completely satisfy me, or that I didn't recognise as useful, you talked about it with so much enthusiasm that I exited the room with renewed motivation. You have the incredible ability to see the added value of even the slightest result for the bigger picture, and that surely helped my research to progress steadily. I am happy that you didn't check these acknowledgements, as I would probably be still rewriting them. Carleen, thanks to you many unclear and boring sections of my papers have been removed and replaced by readable stories with an explanatory picture or diagram. You often reminded me to make presentations a bit more attractive than just blobs of text, which certainly improved many of them. You preferred that I came to your office instead of sending an email, and you were always willing and available to discuss any new results or progress. Almost all of our chats eventually drifted away from the main topic, discussing sport events, weather extremes or just general non-science stuff, which I greatly appreciated.

This work relies heavily on the wellbeing of our in-house regional climate model RACMO2, and with that on Willem Jan's modelling experience. Thanks for all the time you spent with me debugging or interpreting its quirks. I would furthermore like to thank Peter for the numerous discussions about the albedo parameterisation, as well as the nice insight you provided in a weatherman's life. I am also thankful for Melchior, Brice and Christiaan, who have devoted their lives to RACMO2. Together we've made our lives somewhat easier. Brice, thanks for coming along on a road-trip through California. What a different world it was back then!

I entered room 6.04 on 2 May 2016, and I left it prematurely and unexpectedly for the final time on 12 March 2020. Antonija, Bert and Erwin were always there in some composition. Antonija, thanks for all the coffee and cookies during my Vierdaagse training weekends. Bert, I'm afraid you'll have to find a new phone operator. Erwin, I hope the air at the KNMI is better than at IMAU. I very much liked the video calls we had during the final months of my PhD.

There is no IMAU without Sandra, Floor or Clara. Thanks to your organisational skills we can enjoy the BBOS symposium every year, but also informal IMAU activities and anything that happened on the 6<sup>th</sup> floor. I always enjoyed our chats during all of these events, and I'll gladly come back for IMAU anniversaries.

Finally, there is the most important group at IMAU: HOeMBA, also known as the PhD mental support group. Thanks for providing a safe haven for all issues, directly and indirectly related to the PhD life. I hope this group remains intact for years to come, as I believe it provides a very important possibility to come together as fellow PhD students. I owe you a pancake lunch!

Dank aan de Nimma Boys voor de uiteenlopende gesprekken over bijna alle mogelijk denkbare onderwerpen. De discussies vonden op ieder willekeurig moment van de dag plaats, wat soms tot iets te lange pauzes leidde, maar het bood vaak ook een welkome afleiding van mijn onderzoek. En als ik dan om halfzes thuiskwam uit Utrecht, stond Gillian klaar om even een rondje te gaan hardlopen. Bedankt voor het inzicht dat je bood in het bedrijfsleven. Mogelijk hebben onze gesprekken er (mede) voor gezorgd dat ik ook deze carrièreswitch heb gemaakt, en daar ben ik voorlopig heel tevreden over. Helaas moet ik het nu zonder je hardlooptmotivatie stellen, wat ook meteen te zien is in mijn Strava-geschiedenis.

Tijdens een lockdown moet je het maar van je burens hebben, en gelukkig had ik Chris en Agnieke. Bedankt voor de spontane tuingesprekken, waarin we elkaar door de lockdown sleurden en jullie me af en toe met Fiep lieten knuffelen (of Fiep met mij). Zorg goed voor ons mooie straatje.

Af en toe moet er genoten worden van de goede dingen in het leven, en dan waren daar de waarde heren van Pierre. Ik weet niet of er *appellations* zijn in het Verenigd Koninkrijk, maar als ik ze vind weet ik er vast een goed

verhaal over te vertellen. Ik hoop dat we nog minstens nul keer een fysieke bijeenkomst kunnen houden, jolig en goedgemutst.

Jungs. Ich waas nao vief jaor de ierste van oze groep mèt 'n diploma, en wersjienlik bin ich noe nao twellef jaor neet de lètste. In 2009 vloge d'r 'n aantal van ós oet nao versjillendje heuk van 't landj, van Mestreech toet Amsterdam, en soms is 't lestig óm ós allemaol byein te kriege. Mer èns in de zoeëvööl tied löktj 't ós toch weer en den veultj 't meteen vertroedj. Bedanktj vöör de vööle leuke, late aovendjes woeëvan d'r wersjienlik nog vööl gaon vólge, ónger 't genot van 'n pötje Risk en 'n sjtök kruumelevlaai.

Eric, Petra en Romy, bedankt dat jullie me in jullie gezin hebben gesloten. Jullie vertellen vaak hoe ik als nette Limburgse jongen voor het eerst bij jullie over de vloer kwam, en jullie vragen je maar af wat er toch met die persoon is gebeurd. Blijkbaar zat er ergens een platte Braobander in mij en die hebben jullie naar boven weten te halen. Dat zal wel de invloed zijn geweest van de kaalste van het stel. Ik kom altijd graag bij jullie langs, het is fijn om lekker te wandelen of op de bank te ploffen en zo de werkweek een beetje te vergeten, uiteraard met een flink stuk tâââart (zonder slagroom!).

Marluuke en Joeri, jullie hebben me in het laatste jaar van mijn promotieonderzoek ook een goede manier gegeven om de werkperikelen te vergeten. Niets is zo heerlijk hersendodend dan torentjes bouwen of puzzeltjes maken met Sem, extra geholpen door de duffe muziekjes die uit de speelgoedautootjes komen. Bedankt voor jullie grenzeloze interesse in mijn werk en onderzoek, en de verrassende vragen die jullie erover wisten te stellen. We delen een passie voor heerlijk speciaalbier, en hopelijk komen er snel speciaalbieravondjes met Engelse ales.

*Two beautiful shiny rails.* Dat appte ik toen ik voor het eerst alleen met de trein naar Nijmegen ging in de zomer van 2009. Wat volgde was een tijd waarin ik deed wat veel studenten deden: niet te hard studeren. Pap en mam, jullie hebben met lede ogen moeten aanzien hoe de kapitaalinjecties in de kassa's van Piecken, Samson of het Beestfeest verdwenen. Een investering in de toekomst zullen we maar zeggen, al zit ik nu aan de

overkant van het Kanaal. Waar ik nu sta had ik nooit bereikt zonder jullie onvoorwaardelijke steun en aandacht voor mijn ervaringen en ontwikkelingen. Al was het lastig om me inhoudelijk op weg te helpen, jullie wisten altijd wel de motivatie en de aansporing te geven die ik nodig had om weer vooruit te komen.

Mijn laatste woord van dank is voor jou, Melissa. Als je samen tegelijk een PhD kunt doorlopen, kun je waarschijnlijk wel alles aan. Dat bleek wel toen we vanaf maart elke dag samen thuis werkten, en vanaf september samen in Engeland zaten. Met jou verleg ik mijn grenzen en neem ik stappen die ik anders niet genomen zou hebben. Je hebt me veel geleerd, bijvoorbeeld hoe ik het schrijven van een proefschrift moet plannen (mam is jaloers!), maar ook hoe ik mijn gevoelens en gedachtes beter onder woorden kan brengen. Na een werkdag doe ik niks liever dan met jou heerlijk series kijken of gamen, en in de weekenden lopen we samen de stress eruit en zien we wat wel er overblijft. De Vierdaagse is ons feestje en hopelijk lopen we er daar nog heel veel van. Ik ben graag met jou het Engelse avontuur aangegaan, en ik ben benieuwd welke avonturen ons nog meer te wachten staan.

## Resume

Stan Jakobs was born on 7 September 1991 in the town of Heythuysen. He has always been fascinated by astronomy and weather. During high school, he carried out a school research project in which he measured the mass of Jupiter using a regular camera and a telescope. This project was considered the best physics-related school research project of 2009, and won him and a classmate a trip to the astronomical observatory of La Palma. After high school, Stan moved to Nijmegen for his bachelor and master education in Physics and Astronomy at Radboud University. While he studied high-energy physics and quantum mechanics, he realised this that was not his cup of tea, and decided to do his master thesis research with Willem Jan van de Berg at the Institute for Marine and Atmospheric research Utrecht (IMAU) at Utrecht University. This thesis concerned applying the climate model RACMO2 to Svalbard. After obtaining his master's degree, Stan continued his stay at IMAU to pursue a PhD degree under the supervision of Carleen Tijn-Reijmer and Michiel van den Broeke, of which this doctoral thesis is the final product. Since September 2020, Stan has been working as a software engineer at Gigaclear, a glass fibre company based located in Abingdon near Oxford, United Kingdom.